ERDA ORO-2504-252

Inclusive Particle Production in e^+e^- Interactions at 3.8 and 4.8 GeV

Ph.D. Thesis

by

Thomas L. Atwood

Technical Report No. 77-040

PF No. 77-135

UNIVERSITY OF MARYLAND
DEPARTMENT OF PHYSICS AND ASTRONOMY
COLLEGE PARK, MARYLAND

ABSTRACT

Title of Dissertation: Inclusive Particle Production in e^+e^- Interactions at 3.8 and 4.8 GeV

Thomas Lamar Atwood, Doctor of Philosophy, 1976

Dissertation directed by: Professor Gus T. Zorn, Department of Physics and Astronomy

This dissertation describes an experiment which measured the inclusive momentum spectra for hadrons and muons produced in e^+e^- interactions at total center of mass energies of 3.8 and 4.8 GeV. The experiment was performed at the SPEAR electron-positron storage ring at the Stanford Linear Accelerator Center. It consisted of a single-arm spectrometer, with additional apparatus to measure charged multiplicities and to tag collinear muon and electron pairs.

The Lorentz-invariant cross section for hadrons is found to exhibit Feynman scaling at all measured momenta. The invariant cross sections for pions, kaons and protons fell along the same exponential energy curve, exhibiting a characteristic hadron temperature of $kT = 0.19$ GeV. Bjorken scaling was found to hold separately for pions and for kaons for $x \equiv 2E/\sqrt{s} > 0.4$; however, the x-dependences of the two cross sections are significantly different. Results are also presented for the inclusive momentum distributions of the hadron charged multiplicity.

An examination of inclusive muon production found the presence of a small anomalous muon signal for two-prong events noncoplanar by more than 20^o and with $p_\mu > 1.05$ GeV/c: $d\sigma/d\Omega|_{90^o} = 17^{+12}_{-9}$ pb/sr. Known processes accounted for the observed muon events having charged multiplicity greater than 2, giving an upper limit at the 95% confidence level of $d\sigma/d\Omega|_{90^o} < 7.5$ pb/sr for any new process.

TABLE OF CONTENTS

BLANK PAGE

ACKNOWLEDGEMENTS

The results presented in this dissertation are the end product of the efforts expended by hundreds of individuals working at the University of Maryland, at SLAC, at Princeton University and at the University of Pavia. I am grateful to the members of the staffs of each of these institutions who have contributed to the success of the experiment and who, because of their large number, cannot be thanked individually in so small a space as I have here. I am also thankful for the friendship, cooperation and contributions of my fellow SP8 collaborators, whose names are listed in Reference 1 of Chapter I and who worked many long and arduous hours to bring the experiment to a successful conclusion.

Special thanks go to my advisors Dr. Gus Zorn and Dr. Bruce Barnett, who have taught me most of what I know about experimental physics, and who have made many valuable direct contributions to this dissertation. I would similarly like to give special thanks to Dr. Luciano Trasatti for his warm friendship and for contributing most of what I have learned about instrumentation. I am grateful to Dr. George Snow for acting as my advisor during the absence of Dr. Zorn and for teaching me most of what I know about high energy physics, both inside and outside the classroom. I also wish to thank Dr. Robert Glasser for his valuable assistance with the computer and with several of the statistics problems encountered during the analysis.

I particularly want to acknowledge the friendship and assistance of my fellow graduate students, Dr. Harold Price and Dr. Frank Svrcek, who have always had a ready ear for my troubles and who have made many useful suggestions during the experimental analysis. My deepest

thanks I reserve for my wife Rebecca, who alone has kept me going these last few years and whose moral support has been essential to the completion of this dissertation. She even typed it. The drawings in this thesis are the work of Mr. Lionel Watkins and Miss Joan Wright, whose cooperation and professionalism are deeply appreciated.

LIST OF TABLES

LIST OF FIGURES

CHAPTER I

INTRODUCTION

This dissertation describes an experiment performed at the SPEAR electron-positron storage ring facility at the Stanford Linear Accelerator Center (SLAC). It was performed by a collaboration among members of the University of Maryland, the University of Pavia (Italy), and Princeton University[1]. The experiment has been referred to in the literature[2,3] as "MPP" or "MP^2". However, within this thesis it will be exclusively termed the "SP8" experiment, the designation applied to the original proposal. This will serve to distinguish it from the later experiments performed by the same collaboration.

The experiment was conducted from October, 1973 through June, 1974. It was among the earliest to run at the SPEAR storage ring, and it consequently represented one of the first attempts to observe the nature of e^+e^- interactions at total CM energies above 3.0 GeV. At the time the experiment was proposed, the results of deep inelastic scattering of electrons on protons had given a striking confirmation of the existence of the scaling previously proposed by Bjorken. This in turn gave strong support to the concepts which had been put forward in the various parton models of the nucleons, in which they were treated as being composed of several point-like constituents. One of the chief unanswered questions at that time was whether the same type of scaling would be observed in e^+e^- hadron production.

The SP8 experiment was proposed primarily to attempt to help answer this question. The idea was to measure the inclusive momentum

BLANK PAGE

spectrum, especially at hadron momenta greater than 1.0 GeV/c, and to distinguish pions, kaons and protons at these momenta. The low-momentum spectrum was simultaneously being measured by the SLAC-LBL collaboration, using their solenoid detector at SPEAR, which was better adapted to the identification of hadrons at lower momenta.[4] It was therefore natural to compare results with the SLAC-LBL group, not only because of the complementary nature of the two experiments, but also because, until recently, they were the only group which had presented comparable results.

The principal part of the apparatus was a single-arm spectrometer situated at 90° from the beam and subtending a solid angle of about 0.1 sr. It identified one particle associated with each trigger event and measured its momentum. The trigger particle was required to have a momentum greater than 400 MeV/c. On the side of the beam opposite the spectrometer there were proportional wire chambers and scintillation counters for tagging back-to-back electrons and muons. A set of proportional wire chambers surrounded the beam interaction region and measured the total charged multiplicity for each event. The experimental equipment is described in detail in Chapter II.

The apparatus was exposed to colliding beam center-of-mass energies ranging from 3.0 to 5.2 GeV, but the vast majority of the data was taken at the two energies of 3.8 GeV and 4.8 GeV, the latter sample containing about 80% of the total.

The procedures used to reconstruct the events are described in Chapter III, which includes information on the selection criteria applied to the data sample. Chapter IV is concerned with the procedures used to identify the spectrometer particle of each event.

The performance of each of the spectrometer components was studied in order to arrive at an efficient particle classification scheme with precisely known identification errors.

The experimental results begin with Chapter V, which is a short study of collinear μμ events. Since the QED production cross section for these events is well known, they can be used to normalize the magnitudes of the inclusive cross sections for other types of events, or, equivalently, to calculate the effective e^+e^- beam luminosity for each beam energy.

The measurements of inclusive hadron events are presented in Chapter VI. That chapter is divided into three major parts. Sections B, C and D describe the various corrections that had to be applied to the observed numbers of events to account for particle interactions with the apparatus. The inclusive hadron spectra are presented in various ways in Section F and compared with other experiments. Finally, Section G gives the hadron multiplicity distributions.

While the analysis of the experiment was in progress, the SLAC-LBL collaboration announced the discovery of several new states produced by e^+e^- interactions. Among their results was evidence, in the form of eμ events, for the existence of a heavy lepton. This motivated a search of the SP8 data for similar events. A full discussion of these inclusive muon results is given in Chapter VII. A short conclusion summarizing all the results of the experiment is given in Chapter VIII.

REFERENCES

CHAPTER I

1. The members of the MP^2 collaboration were:
University of Maryland: T. L. Atwood, D. H. Badtke, B. A. Barnett, L. V. Trasatti, and G. T. Zorn;
University of Pavia: M. Cavalli-Sforza, G. Goggi, G. C. Mantovani, A. Piazzoli, B. Rossini, and D. Scannicchio;
Princeton University: D. G. Coyne, G. K. O'Neill, H. F. W. Sadrozinski, and K. A. Shinsky.
2. T. L. Atwood et al., Phys. Rev. Lett. 35, 704 (1975).
3. M. Cavalli-Sforza et al., Phys. Rev. Lett. 36, 558 (1976).
4. See, for example, G. S. Abrams et al., Phys. Rev. Lett. 33, 1453 (1974) or G. Goldhaber et al., Phys. Rev. Lett. 37, 255 (1976).

CHAPTER II

THE APPARATUS

A. General Description

The SP-8 experiment consisted of three principal components: 1) a small solid angle single-arm spectrometer oriented at 90^{o} to the beam, designed to identify particles and measure their momenta; 2) an assembly of proportional wire chambers, a shower detector, and a hadron filter on the opposite side of the beam from the spectrometer for tagging back-to-back muons and electrons; and 3) a wrap-around central detector designed to measure the total charged multiplicity. The apparatus is shown as seen from above in Fig. II-1 and as seen from the side in Fig. II-2. Detailed specifications on various parts of the apparatus are given in Table II-1.

A particle entering the spectrometer first traversed a series of proportional wire chambers which measured its initial location and direction of travel. Nested in this wire chamber assembly was a small scintillation counter, designated S1, which initiated the time-of-flight measurement. The particle then passed through the threshold Cerenkov counter and then entered the magnet gap. The particle momentum was determined from position measurements in the proportional wire chambers C3X, C4X, and C5X. C3X and C5X were situated at the ends of the magnet gap and C4X was about midway between the other two, as shown in Fig. II-1. After traversing the magnet, the particle entered the shower detector, designed to tag electrons by their relatively large showers. The time-of-flight measurement, gated on when the particle entered the S1 counter near the beam, was made using

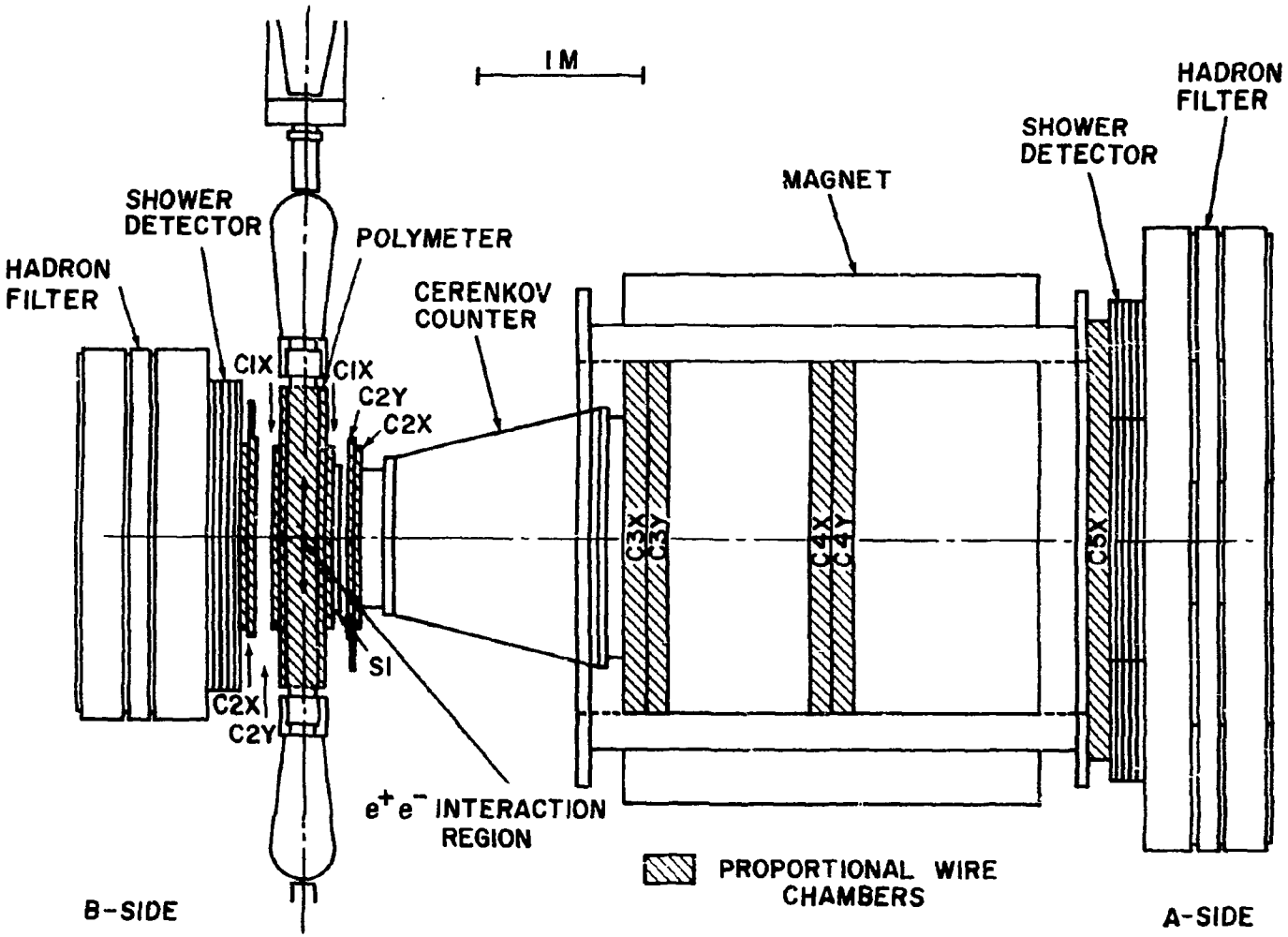

FIGURE II-1. Plan view of the experimental apparatus.

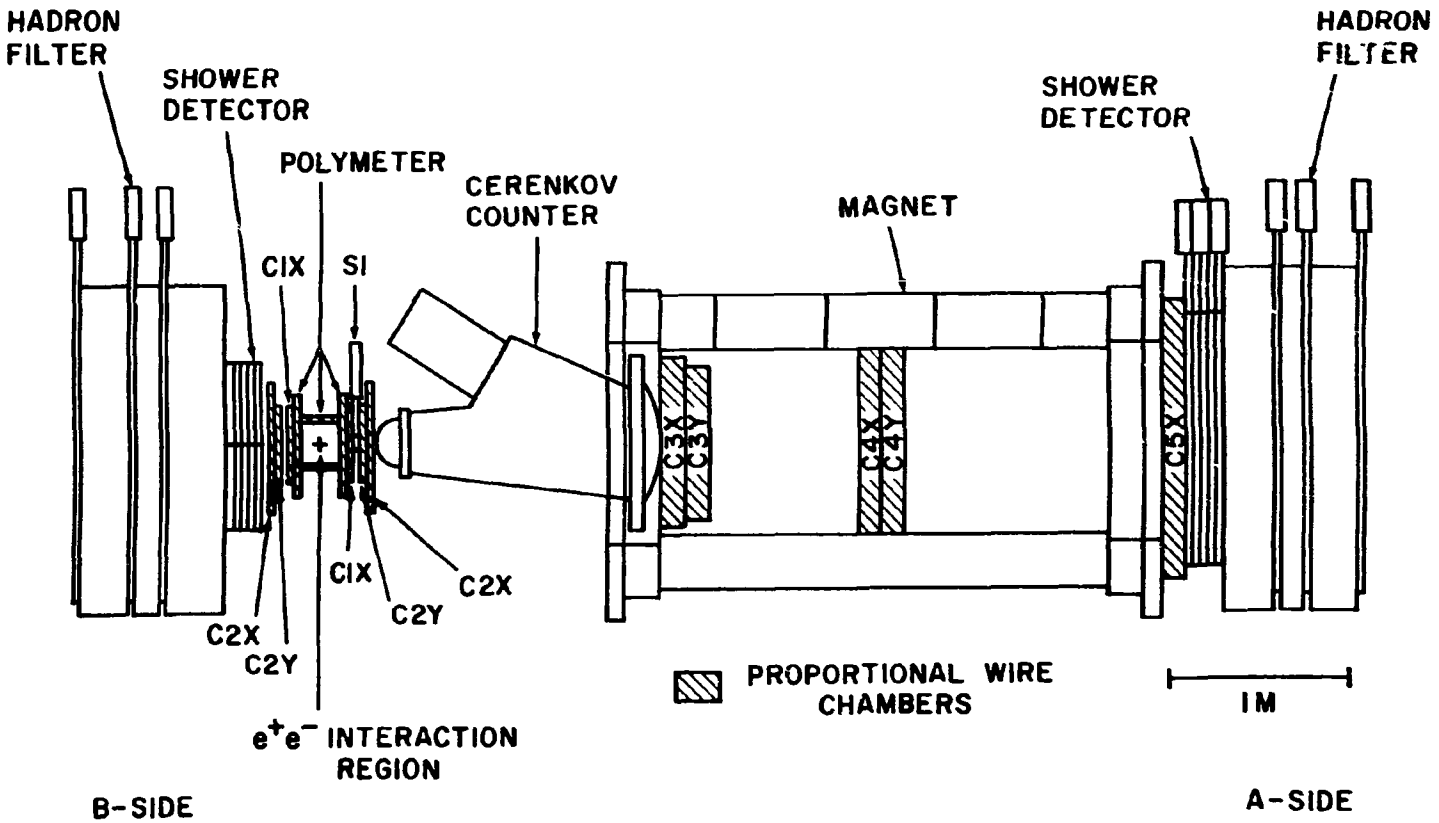

FIGURE II-2. Elevation view of the experimental apparatus.

Magnet: B_{max} = 4.2 Kgauss $\int B_y \cdot dz \simeq 11.8$ Kg-m $\Omega \simeq 1\%$ of 4π

MWPC's: 6544 wires ? mm spacing (3 mm in polymeter)

0.3° angular resolution

Central Detector: Ω = 97.3% of 4π Efficiency = 98.5%

Cerenkov Counter: Length = 1.5 m Active element 7 atm propane gas

Thresholds: Muon = 0.80 GeV/c Pion = 1.05 GeV/c

Kaon = 3.7 GeV/c Proton = 7.0 GeV/c

Shower Detector: Height = 137 cm Width = 274 cm

Composition = .64 cm Pb x 5 x (.64 cm Pb + 1.91 cm scintillator)

Thickness = 7.0 radiation lengths

Hadron Filter: Height = 168 cm Width = 343 cm

Composition = 30.5 cm Fe + 1.9 cm scint. + 12.7 cm Fe + 1.9 cm scint. + 25.4 cm Fe + 1.9 cm scint.

Thickness = 6.8 nuclear collision lengths

TOF System: σ = 0.6 nsec Flight path = 5 m

Conjugate Shower Detector: Ω = 19.8% of 4π

Conjugate Hadron Filter: Ω = 13.72% of 4π

TABLE II-1. Apparatus summary

the scintillation counters in the first two planes of the shower detector. The particle next entered the hadron filter, which was composed of three iron slabs of sufficient thickness to absorb most of the hadrons incident upon it, while passing high momentum muons.

A charged particle leaving the interaction region in a direction more or less opposite to the spectrometer passed through a set of proportional wire chambers similar to those near the beam on the spectrometer side. These measured its initial position and direction. The particle then entered a shower detector and a hadron filter having the same thicknesses as those behind the spectrometer magnet. Thus an electron on the B-side could be identified by its large shower, and a high momentum muon would have penetrated all three iron slabs of the hadron filter.

An important feature of this experiment was the wrap-around central detector, known as the polymeter. This was a set of three layers of proportional wire planes surrounding the interaction region and designed to measure the azimuthal angles of charged particles leaving the interaction region over a solid angle of about 97% of 4π.

B. The Colliding Beams[1]

The experiment was located in the east pit of the SPEAR electron-positron storage ring at SLAC. The beams were injected into the storage ring at 1.5 GeV and then accelerated to the desired energy up to a maximum of 2.6 GeV per beam (SPEAR I). The positions of the beams were monitored using twenty electrostatic position monitors located around the storage ring. Optical monitors were used to

measure the beam size.

A luminosity monitor in the west interaction pit continuously monitored small angle Bhabha scattering, and experimenters were able via a video hookup to keep constant track of the beam currents, the instantaneous and time-averaged luminosity, and the instantaneous and time-averaged beam decay rates. This luminosity measurement was accurate to about 5%.

The lateral beam dimensions were typically σ = 0.1 mm vertically and σ = 3mm horizontally. The bunch length was σ = 14 cm at 2 GeV per beam and varied with energy. The bunch revolution frequency was 1.3 MHz. Typical beam currents were 30 mA, and typical lifetimes were two hours. The beam energy was determined to within 1%, and the energy spread within the bunch was $\sigma(E)/E = 4 \times 10^{-4}$ at 2 GeV per beam. The electron and positron beams occupied the same orbit during normal operation, so that collisions were head-on.

C. The Magnet

The H-shaped 80D96 spectrometer magnet was designed to provide as uniform a field as possible within the magnet gap. On either end were iron magnetic mirrors designed to make the fringe field small, thus reducing the need for extensive magnetic shielding. The three iron blocks of the flux return on the top of the magnet were removable to allow access to the proportional wire chambers inside. The clear inside dimensions of the magnet gap were 100 cm high by 204 cm wide by 244 cm long. The field in the center of the magnet was 4.2 kilogauss, and the integrated vertical field component along the central axis was

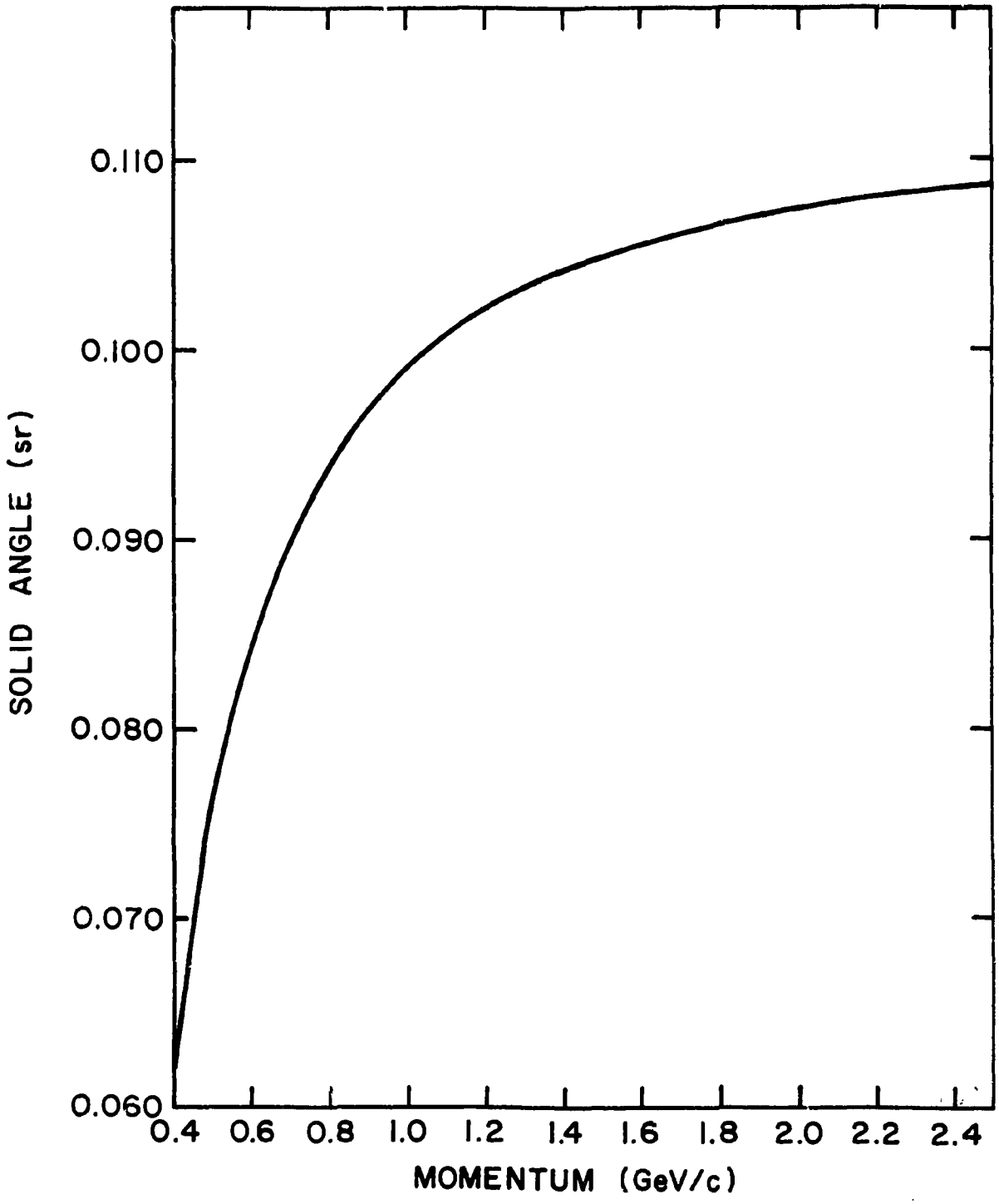

FIGURE II-3. The solid angle acceptance of the spectrometer as a function of particle momentum.

$$\int B_y \, dz = 11.8 \text{ kg-m.}$$

Some details of the magnetic field map are given in Appendix A, which describes the subroutine used to calculate the magnetic field values at arbitrary points within the magnet.

The magnetic field was mapped at SLAC using a three-dimensional Hall probe which was read on line onto magnetic tape. The hadron filter was in place during the field mapping, since it contained a large amount of iron and was positioned near the magnet. A remap of a portion of the field showed it to be reproducible within 0.1% at the magnet center. During the experiment the magnet current was maintained at 3000 amperes, the value at which the field map was performed, and the field polarity was never reversed. Thus, no significant variations in the field value were expected due to hysteresis effects. The magnet current was monitored continuously throughout the experiment.

The solid angle acceptance of the spectrometer at full field is shown as a function of particle momentum in Fig. II-3. The acceptance was determined by integrating particle trajectories through a computer simulation of the spectrometer, using the magnetic field subroutine described in Appendix A.

D. The Proportional Wire Chambers

1. General

Particle positions in the apparatus were measured by nineteen proportional wire chambers totaling 31 wire planes.[2] There were a

total of 6544 wires, most of which were spaced at 2 mm intervals. The wire spacing limited the momentum resolution to σ = 1.5% at 2 GeV/c. Detailed information on the various proportional wire chambers is given in Appendix B.

The positioning of the chambers is shown in Figs. II-1 and II-2. The designation for each chamber includes the position coordinate measured. The x-coordinate axis was parallel to the beam; the y axis was vertical. The origin of coordinates was arbitrarily located in the vicinity of the electron-positron interaction region, and the positive z axis ran through the center of the spectrometer. Occasionally a chamber designation included a letter A or B to indicate on which side of the beam it was positioned. The spectrometer side of the beam was referred to as the A side and the conjugate side was the B side. Thus, for example, C2AX was the second x plane on the spectrometer side of the beam.

The positions of the chambers, as well as other parts of the apparatus, were specified by a careful survey. Cosmic ray muon data was acquired with the magnetic field turned off, and the resulting straight line trajectories were used to precisely determine the chamber positions.

2. The Polymeter

A set of proportional wire chambers of particular importance was the central detector, also known as the "polymeter". It consisted of four proportional wire chamber packages, each containing three planes of wires. The three polymeter planes encircled the beam interaction region as shown in Fig. II-4. The wire spacing was 3 mm

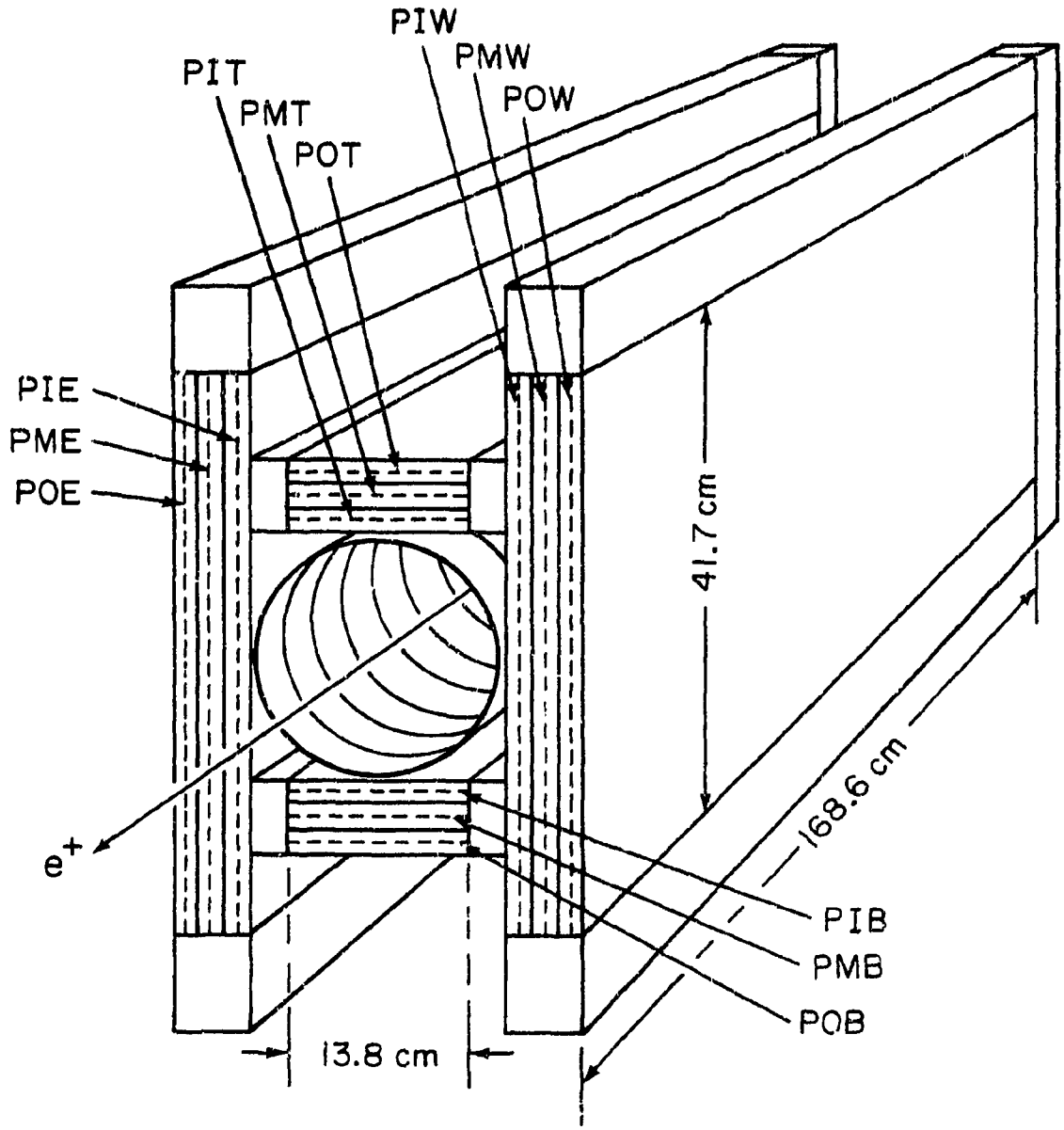

FIGURE II-4. The central detector, also referred to as the polymeter, surrounded the beam pipe, subtending a solid angle of 97% of 4π. The wire spacing in each plane was 3 mm and all wires ran parallel to the beam.

and all wires were parallel to the beam, so that only the azimuthal angle of each track was measured. The effective solid angle over which tracks could be measured was 97.3% of 4π, and the average track detection efficiency was 98.5%. The efficiency was determined by examining polymeter tracks from the hadron data. Two- and three-plane tracks extrapolating through the beam interaction region were counted and compared to determine the average single-plane efficiency. The probability for fewer than two planes to fire was then deduced.

E. The Cerenkov Counter

The threshold Cerenkov counter was an aluminum pressure vessel about 1.5 m long containing 7 atmospheres (abs) of propane. It was designed primarily to distinguish kaons from pions at momenta ranging from about 1.1 GeV/c to more than 4 GeV/c, but was also useful for distinguishing electrons and muons from hadrons at lower momenta. A detailed discussion of the Cerenkov counter design and performance is given in Appendix C.

As a particle traversed the counter, the forward-emitted Cerenkov radiation was collected by a single large mirror with a 118 cm radius and was reflected into a bank of 48 56AVP photomultipliers, whose outputs were added. The photomultipliers were fronted by a 2.5 cm thick plexiglass window, the first surface of which was coated with a P-terphenyl wavelength shifter[3] designed to recover the ultraviolet Cerenkov component as visible light.

The mirror and detector optics were designed using a ray-tracing computer simulation program. The completed counter was tested in beams of pions and protons with momenta of 6 to 8 GeV/c, and using

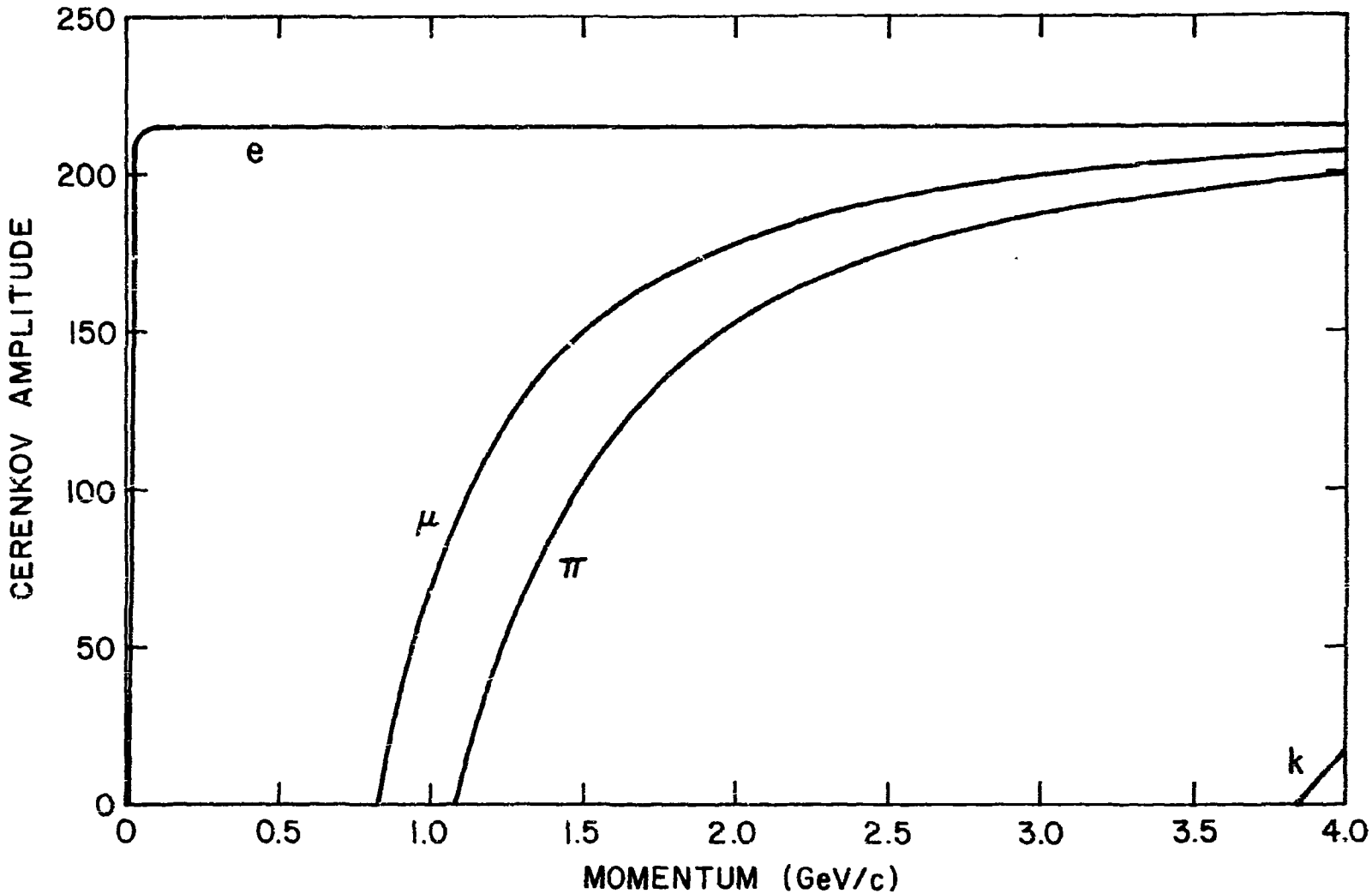

FIGURE II-5. The calculated Cerenkov counter amplitude for various particles as a function of momentum. The calculated number of photoelectrons produced was normalized to the observed amplitudes for electrons.

both freon and propane at various pressures. Efficiency scans were made as a function of the particle position and direction in the counter. The Cerenkov counter interior contained light emitting diodes which were positioned in front of the phototube detector plane and used to periodically check the detector performance.

The predicted mean amplitudes for various types of particles as a function of momentum are shown in Fig. II-5. This can be compared with the actual performance for hadrons shown in Fig. IV-9.

F. The Shower Detector

The shower detector, situated behind the magnet, was designed to distinguish electrons from hadrons by their larger electromagnetic showers. A description of its use in particle identification is given in Section IV-B. It was a five-layer sandwich, each layer consisting of 0.64 cm (1/4") of lead and 1.91 cm (3/4") of scintillator, except that an extra 0.64 cm (1/4") of lead was placed in front of the first layer. Each plane of scintillator was composed of four counters, each 137 cm (54") high and 69 cm (27") wide. A 30 cm high flat triangular light pipe was glued to the top of each counter and interfaced with a 56AVP photomultiplier, which was read into an 8-bit analog-to-digital converter (ADC). Some of the light pipes were asymmetric to allow for close packing of the phototubes in adjacent planes. Two light-emitting diodes (LED) were attached to each counter (as well as to each of the other scintillation counters in the experiment and to the Cerenkov counter) to allow frequent monitoring of the system performance.

The B-side shower detector was composed of the same thicknesses of lead and scintillator as the spectrometer shower detector, although the lateral dimensions were smaller. Each scintillator plane consisted of two counters, one above the other, each of which had a flat light pipe and a photomultiplier attached to the north end.

The individual counter nomenclature consisted of two letters and two numbers. For example AS32 designates the A-side shower detector, third layer, second counter from the left as seen from the beam interaction region; the counter BS3T was the top counter in the third layer of the B-side shower detector.

G. The Hadron Filter

The hadron filter was an iron absorber designed to separate muons from hadrons at momenta greater than about 1.05 GeV/c. Its performance characteristics are described in Section IV-C, and its dimensions are given in Table II-1. As shown in Fig. II-1 and Fig. II-2, the hadron filter was a sandwich of three iron slabs and three planes of scintillation counters, each plane containing five adjacent counters. Each individual counter was 69 cm (27") wide and 168 cm (66") high. A flat triangular light pipe was glued to the top of each counter and interfaced with a 56AVP phototube. The photomultiplier output from each counter was discriminated, and the resulting "yes-no" signal was read into a single-bit data buffer. Pulse height information was not recorded. The B-side hadron filter was composed of the same thicknesses of iron and scintillator as the spectrometer hadron filter, although its lateral dimensions were smaller.

H. The Time-of-Flight System

The organization of the time-of-flight (TOF) system is shown in Fig. II-6. The time of flight for a particle traversing the spectrometer was measured between the S1 counter, located near the beam, and either of the first two layers of counters in the shower detector, located behind the magnet. There were actually four TOF measurements made for each particle in the spectrometer. The S1 counter had two phototubes, one attached to each end, and the first two planes in the shower detector provided two distinct TOF termination measurements. This provided four different counter-to-counter TOF combinations. During the data analysis these four measurements were averaged to provide a single TOF value for each event. The average distance traversed between the S1 counter and the shower detector was about five meters, depending on the particle direction and momentum.

The TOF measurements were made using an overlapping pulse technique.[4] An initiating pulse of fixed duration (100 nsec) was generated when a particle passed through the small S1 counter near the beam. This S1 pulse was used to gate the analog-to-digital converters (ADC's). As shown in Fig. II-6, it was required to be coincident with the enable signal from the LMT counter subtrigger, described in Section II-I.

The TOF termination signal was obtained from one of the counters in the first two shower detector planes. Due to equipment limitations, the TOF outputs from the four counters in each plane were daisy-chained together as shown in Fig. II-6. This resulted in TOF information loss for a few events where two or more counters in the same shower

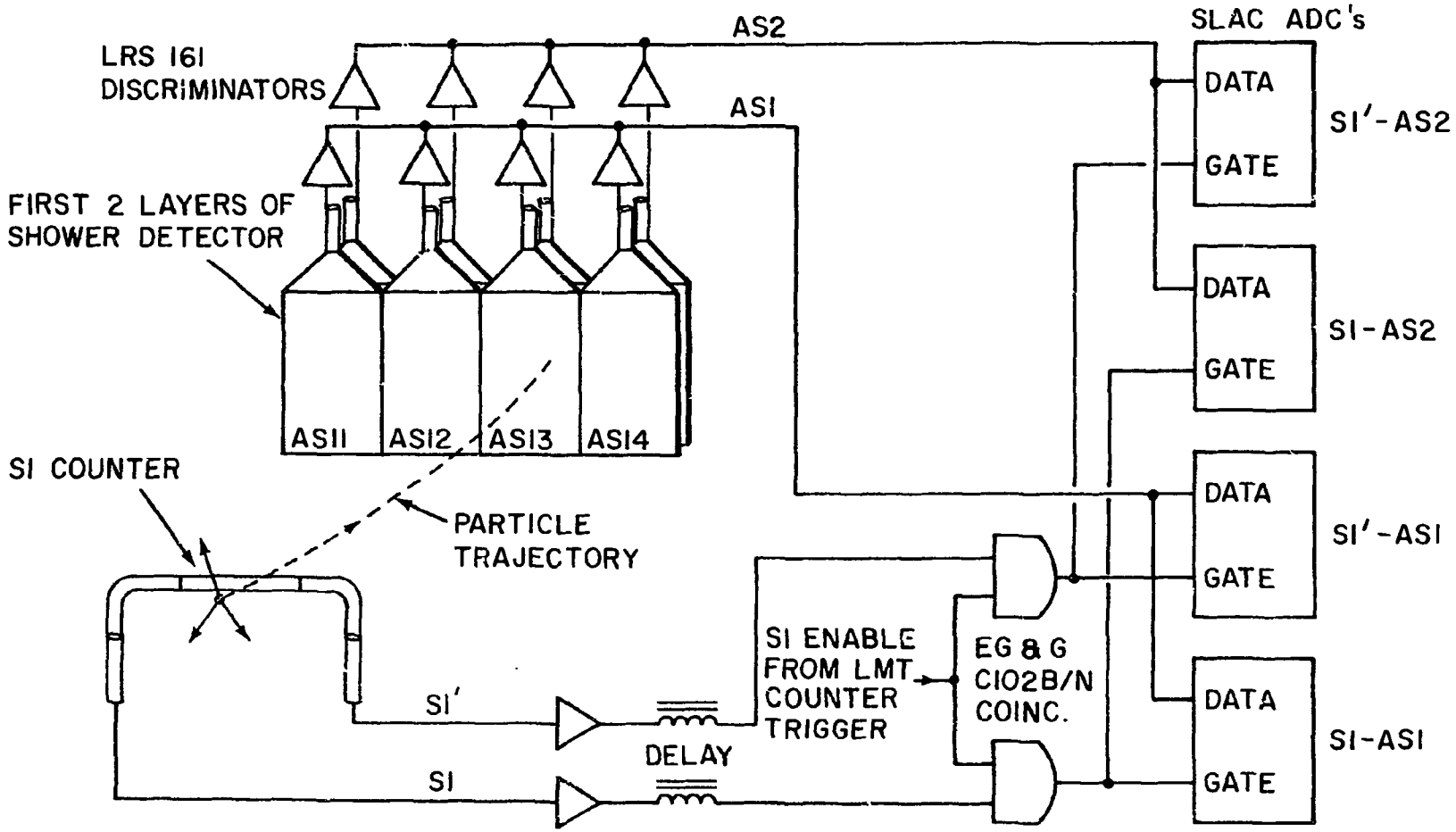

FIGURE II-6. The time-of-flight system. The electron and positron beams collided near the S1 counter. The ADC data input current was integrated until the S1 gate pulse expired. The contents of the four ADC's were later averaged to obtain a single TOF value.

detector plane were hit. The TOF OR from each shower detector plane provided the data input for the ADC's, which was integrated until the S1 gate pulse expired. Thus the ADC output was a digital time-of-flight measurement proportional to the degree of overlap of the S1 and shower counter pulses.

During the data analysis it was necessary to normalize the raw TOF measurements to account for several effects. The TOF dependence upon the particle position in the counter was determined from individual counter studies using cosmic rays. The TOF was also corrected for residual dependence on the amplitudes of the S1 and shower counter outputs. During data acquisition the system was monitored every few hours by pulsing the light-emitting diodes mounted on each counter and recording the results along with the data. As a part of each such calibration a fixed time delay was introduced into the diode signals. The resulting shift in the observed TOF value defined the time scale used to normalize the particle TOF measurements. The final counter normalization was performed using muons, electrons, and low momentum pions from the experimental data.

The implementation of the TOF measurements for determining particle identities is described in Section IV-F. The average resolution was σ = 0.6 nsec, as shown in Fig. IV-11.

I. The Trigger

To facilitate the study of one-particle inclusive hadron spectra the trigger was designed to select events where one or more charged particles traversed the spectrometer. There were no other requirements on trigger events except for timing considerations designed to reduce

contamination from various backgrounds associated with cosmic rays, the linear accelerator and the electron and positron beams. The trigger configuration can be represented as a coincidence between two major subsystems: T = LMT · PWC. The LMT subtrigger consisted of a combination of scintillation counters in coincidence with a timing signal from the colliding beams. The PWC subtrigger was a coincidence of proportional wire chambers in the spectrometer.

To reduce the background rates, the trigger was required to be coincident with an enable pulse synchronized with the beam interaction. A signal coincident with each collision of the electron and positron beams was obtained by delaying and discriminating the output from one of the capacitive beam pickup electrodes located in the storage ring upstream from the beam interaction region.[1] The trigger was synchronized with the delayed signal from the positron bunch as it approached the interaction region. A short duration inhibit signal was used to prevent a second coincidence due to the passage of the electron bunch over the same electrode following the beam collision.

The LMT subtrigger can be decomposed as LMT = S1·S1'·(AS1X+AS2X)·RF, where RF is the beam pickup signal. S1 and S1' are the outputs of the two photomultipliers attached to the ends of the S1 scintillation counter, situated near the beam. The relatively small dimensions of this counter, 3.8 cm (1½") x 71 cm (28") required the trigger particle to have passed near the colliding beam interaction volume. The term AS1X (AS2X) designates any one of the four scintillation counters in the first (second) plane of the shower detector behind the magnet.

Since the accidental rate from the relatively large shower counters was high, it was necessary to also include proportional wire chambers in the trigger. The configuration most commonly used was PWC = C1AX·C3X·C5X, which required a chamber near the beam, one at the entrance and one at the exit of the magnet, as shown in Fig. II-1.

In order to have the diode calibration events taken every few hours conform as closely as possible to the real events, a fake RF signal was switched into the trigger logic in place of the beam pickup. This eliminated the risk of changing the timing characteristics of the trigger circuits resulting from switching the RF signal out of the coincidence. The pulsing of the LED's mounted on each of the scintillation counters and inside the Cerenkov counter was synchronized with a "pulser tree" signal, injected into one wire on each of the proportional wire chambers. Thus no change of the trigger configuration was necessary during the calibration runs. The trigger performance was checked by maintaining a careful count of the number of diode events injected during each calibration run and insuring that the correct number of events was read in by the data acquisition system.

The storage ring behaved as a relatively efficient conductor for electromagnetic disturbances resulting from the triggering of the spark chambers being used in the SPEAR west pit. To avoid recording events triggered by these disturbances a veto signal derived from the firing of the spark chambers was used to activate the "event stop logic" (ESL) in the data acquisition system. This trigger override was distinct from the trigger itself and terminated

an event at a much later time, while it was being read into the computer. Typically two or three percent of the triggers were vetoed in this manner.

J. The Data Acquisition System

When an event occurred which satisfied the trigger requirements, it had to be read into a computer and then written out on magnetic tape. There were three major electronics subsystems for reading in the data: (i) the proportional wire chamber reader electronics, (ii) the CAMAC system for recording time of flight and counter amplitudes, and (iii) a series of discriminator-coincidence-buffers (DCB's) each of which recorded a one-bit ON or OFF signal from one of the counters in either of the two hadron filters.

A simplified logic diagram of the PWC reader electronics is shown in Fig. II-7.[5] The output from each sense wire was first amplified, then discriminated and gated into a data latch. These gates served to shut off the chamber once any sense wire had been hit in order to prevent later accumulation of data unassociated with the event producing the original signal. In particular, an OR of all the wires in the chamber formed the input to the gate latch. Once set by any wire in the chamber, the gate latch closed the gates to all the data latches. That portion of the trigger logic which was associated with each chamber and contained one or more such gate latching circuits was known as the "local logic" for that chamber.

Once the gate latch for any chamber was set, it signalled the fast logic, which contained the trigger coincidence electronics.

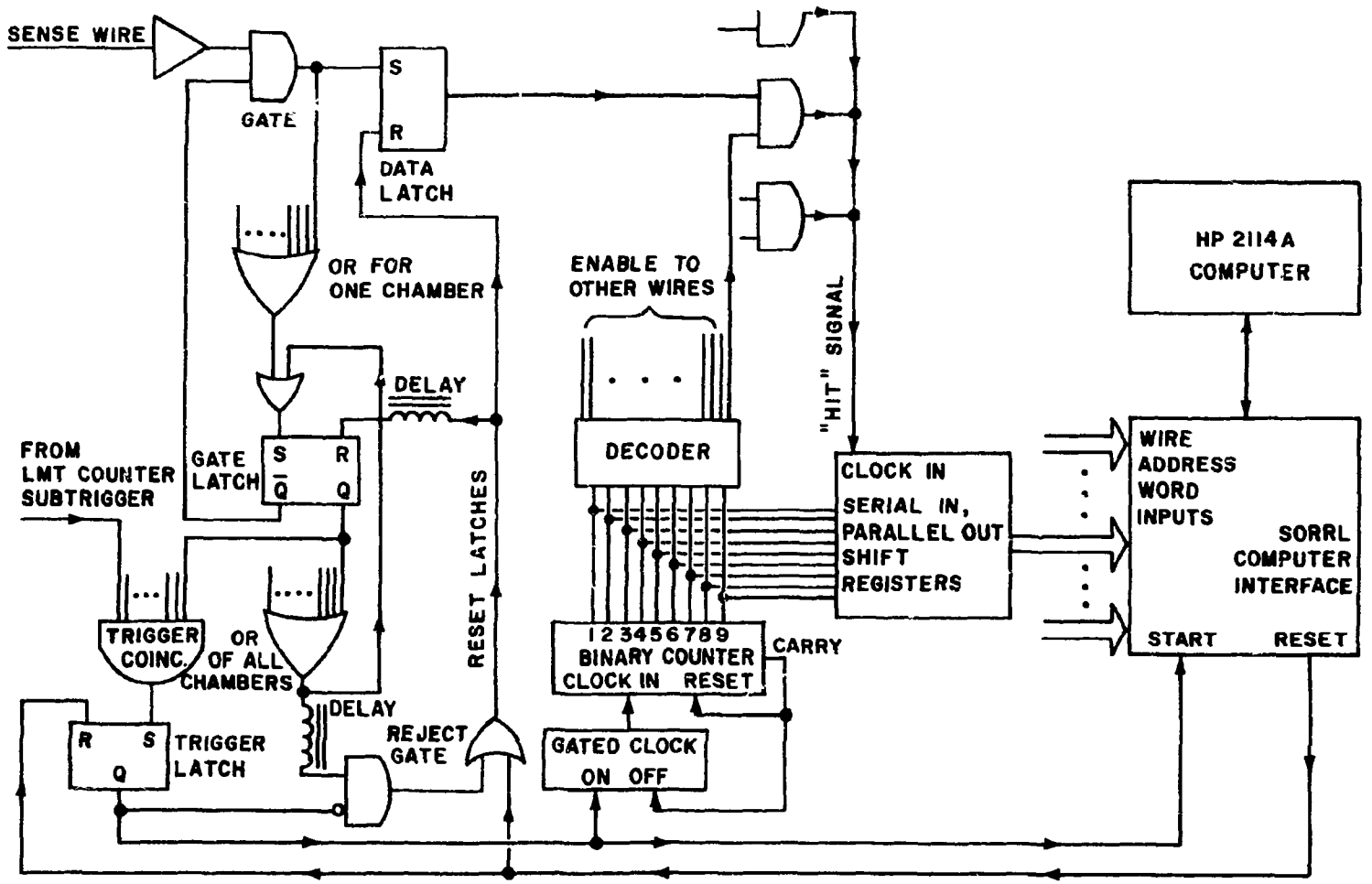

FIGURE II-7. Simplified diagram of the MWPC recording and trigger logic. A single sense wire is shown at upper left. The trigger logic is at the lower left and controlled whether a given event was read in by the computer on the right. The central portion of the diagram shows schematically the logic used to strobe the wire addresses into the computer interface.

The fast logic performed (i) an OR of all chambers with set gate latches and (ii) an AND of all the chambers in the trigger coincidence and the LMT counter subtrigger described in Section II-I. The presence in the fast logic OR of a signal from any chamber resulted in the immediate setting of the gate latches of all the remaining chambers. If the trigger coincidence was satisfied, a START signal was then sent to the computer and to the reader electronics to begin strobing the event into the computer. If the trigger was not satisfied, a reset signal was generated which reset all the data and gate latches, thus clearing out the previous data and reopening the gates on the sense wire inputs.

Associated with each chamber was a reader card. When the trigger was satisfied each reader card received a START signal and began strobing in the addresses of the sense wires which had been hit. These addresses were stored in shift registers located in the reader card. A maximum of five sense wire addresses (fifteen for the central detector) could be stored on each card. If more than this number of wires fired, an overflow bit was set.

The shift register and overflow bit outputs of all the reader cards were transmitted as voltage levels to the input terminals of a computer interface buffer known as SORRL (Son Of Raytheon Read Logic). These binary addresses were subsequently strobed into the computer on machine command.

The Cerenkov counter, scintillation counter, and time-of-flight amplitudes were read into the computer from their respective ADC's via a CAMAC crate controller. The single OFF-ON bits from the counters in the hadron filter were stored in the discriminator-

coincidence-buffers (DCB's) and read directly into the computer input buffer SORRL. These bits were stacked into three computer words.

The data acquisition computer was a Hewlett-Packard 2114A with 8K memory. Its principal function was to read in the data, display it graphically on a small storage oscilloscope, and write it out on magnetic tape. This activity was monitored and controlled by the experimentalists through an interpreter language known as SECOP (Sequencer, Compiler and Online Processor), which used memory and time very sparingly and was subject to operator intervention at every point.

The information in the SORRL interface was read into a rotary buffer in the 2114A memory. This data buffer was subdivided into three partitions, each containing one event. As one partition was being filled, another could be written out on tape and, if the tape writing did not get behind, a third partition would be available for the next event. This procedure was designed to minimize the computer dead time effects caused by having to write out the magnetic tape. The data tape word format used for each event is described in Appendix E.

REFERENCES

CHAPTER II

1. "Summary of Technical Information for SPEAR Users," SLAC Users Bulletin No. 26, Oct. 4, 1971.
2. M. Cavalli-Sforza, G. Goggi, W. W. Ash, D. C. Cheng, D. G. Coyne, and G. K. O'Neill, Nucl. Instr. and Meth. 113, 87 (1973).
3. E. L. Garwin, Y. Tomkiewicz and D. Trines, Nucl. Instr. and Meth. 107, 365 (1973).
4. D. I. Porat, IEEE Trans. Nucl. Sci (USA) 20, No. 5, 36 (Oct. 1973).
5. M. Cavalli-Sforza and D. C. Cheng, Nucl. Instr. and Meth. 113, 81 (1973). This article describes an earlier version of the MWPC data acquisition system, to which a few minor improvements have since been added.

CHAPTER III

INITIAL EVENT SELECTION AND ANALYSIS

A. Introduction

1. General

The collisions of electrons and positrons in the beam interaction region were by no means the only source of particles capable of satisfying the trigger coincidence. Other sources of particles with acceptable momenta were cosmic ray muons (which could pass through the spectrometer in either direction), muons associated with the 20 GeV LINAC, and secondaries of all types produced when an electron or positron struck a gas molecule or veered out of the beam and collided with the surrounding vacuum pipe. These kinds of events constituted a background in the e^+e^- data which at some point would have to be removed. However, for the most part they were not identifiable as background until <u>after</u> they were reconstructed.

The purpose of the initial event selection was to weed out the events which for one reason or another could <u>not</u> be reconstructed. It was desirable to accomplish this at the earliest possible stage of the analysis in order to avoid spending computer time on events containing little or no useful information. The guiding principle behind this selection process was that no event would be rejected from further analysis if there was any possibility of its being successfully reconstructed. Exceptions to this rule were made only when it was clear that (i) a very large group of spurious triggers could be rejected, and (ii) the number of reconstructable events lost in the process was very small and could be accounted for.

2. Unreconstructable Event Types

There were a number of different types of events that were not reconstructable. One class of these was the case when the trigger was satisfied because two or more particles were simultaneously present in different parts of the apparatus. These particles might be unassociated, as was the case when a low momentum particle veered out of the beam area upstream from the spectrometer, passed into the magnet entrance gap, and was deflected through the magnet, setting off the chambers and counters in that area. If a second particle simultaneously veered out of the beam area into the chambers near the beam, the trigger was satisfied and the event was recorded. Because of the large tangential velocity component of beam-associated particles, multiple wires in each chamber would usually be fired, ofter causing the shift registers in the reader cards to overflow.

An example of unreconstructable events involving associated particles was the case when a particle in the spectrometer collided with the magnet wall and produced secondaries which continued through the spectrometer. Some other examples of unreconstructable events occurred whenever the trigger configuration was very weak, and a chamber necessary to momentum analysis did not fire; when a particle decayed in flight (sometimes reconstructable, sometimes not); when radio frequency noise from the spark chambers in the west pit was accompanied by a failure (due to a rapid succession of events) of the "event stop logic". These types of events were characterized by the absence of a physically measurable particle trajectory through the spectrometer and often had an unreconstructable

origin near the beam.

3. Event Reconstruction

Whether events were selected or rejected for analysis depended on the configuration of the trajectory in the spectrometer wire chambers and to some extent on the contents of the spectrometer shower counters. In the entire event selection process, no consideration was given to the contents of any chambers or counters other than those in the spectrometer itself.

The reconstruction of particle trajectories in the spectrometer and the calculation of particle momenta is described in detail in Sections III-B,C. If for a given event the trajectory of the particle in the spectrometer was reconstructable, the analysis program recognized and fit the straight line trajectories leaving the vicinity of the interaction region. For each trajectory projecting into the magnet the values of the momentum corresponding to each hit in C4X and C5X were estimated. Then all possible incoming AX lines and C4X and C5X point combinations were compared to determine the most consistent values of the momentum. Once the most likely trajectory had been selected, its origin and momentum were utilized in an iterative integration of the particle path through the spectrometer. The chamber intercept positions were compared with the actual sense wire addresses and the momentum and origin values were refined. A scattering angle was allowed for, assuming the particle underwent possible multiple coulomb or nuclear diffraction scattering in the neighborhood of the Cerenkov counter exit window.

As described in detail in Section III-D, the total charged multiplicity was measured for each event without regard to the identity of the spectrometer particle. Using the three wire planes of the polymeter, any two- and three-point combinations were reconstructed as straight lines and their distance of closest approach to the beam line was calculated. When the A and B side chambers gave additional information, this was included as well. The observed charged multiplicity, averaged over a number of events, was corrected for polymeter overflows, gamma conversion and charged track losses in order to estimate the uncontaminated total charged multiplicity.

B. Track Reconstruction on the A and B Sides

The first tracks reconstructed by the analysis program were the two-dimensional projections in the chambers C1AX, C2AX and C3X. It was necessary to find at least a two-point line in these chambers leading from the beam region into the magnet gap. Otherwise the lack of knowledge of the initial location and direction of the particle would have made it impossible to determine its momentum.

The following three requirements were placed on each event in order that it pass this stage of analysis:

(i) At least two of the chambers C1AX, C2AX, C3X must have been hit.

(ii) At least one line reconstructed by these chambers projected into the magnet.

(iii) The sum of the number of chambers without hits plus the number of reader cards overflowing must be less than three.

The chambers C1AX and C2AX were connected to one reader card each, allowing them to record five sense wire addresses before an overflow occurred. C3X was serviced by two reader cards, and could have had separate overflows in the wires on either side. It could record as many as ten wire addresses. There was one additional constraint involving these three wire chambers which will be discussed later.

Once all the AX lines formed from hits in C1AX, C2AX and C3X were accumulated, the analysis program proceeded to reconstruct all the lines in the AY chambers, which consisted of the three polymeter planes on the spectrometer side--PIW, PMW, POW--and the chambers C2AY, C3Y, and C4Y. The trajectory was reconstructed assuming a straight line Y-projection from the beam area all the way through the spectrometer.

As was the case with the AX lines, as well as lines in other parts of the apparatus, a line containing more than two points was fit using the subroutine LFIT[1]. The sense wire addresses were grouped into clusters of adjacent wires, the midpoint of each cluster being used for the value of the particle coordinate in a given chamber. The uncertainty associated with each chamber coordinate was represented by equating the estimated standard deviation to

$$\sigma = \#\text{ of wires in the cluster} \times \text{wire spacing} / \sqrt{12} .$$

The $\sqrt{12}$ factor results from the assumption of a uniform distribution.[2] In the fitting procedure the weight associated with each data point in the line was $1/\sigma^2$.

A "goodness" was associated with each AY line found. Several factors were used to assign the goodness values. The primary factor was the number of wire chambers used to form the line. The secondary factor was the distance of each chamber from the beam interaction region, the

farthest chambers having the greatest goodness value. A smaller goodness adjustment was made depending on the chi-squared value for the line fit.

One problem associated with this procedure was that if a particle scattered on its way into the spectrometer, the assumption of a straight line AY projection was violated. If the C4Y point was shifted sufficiently far off the original prescatter trajectory, its higher goodness value would occasionally force the C3Y point to be dropped from the line and would also result in an erroneous origin reconstruction. To solve this problem, the σ value associated with the C4Y point was increased to accommodate the uncertainties due to scattering. This resulted in a looser fit which could then include all the chambers associated with the scattering particle.

Two requirements were placed on the AY line reconstruction in order for an event to qualify for further analysis:

(i) The direction of the best AY line must have been within $\pm 10^{o}$ of the horizontal plane, and

(ii) The best AY line must have contained points from at least two of the six wire planes, and at least one point in the line must have been outside the polymeter.

Only the AY line with the highest goodness was used in the momentum analysis.

The BX lines were formed by taking all two-point combinations in C1BX and C2BX. The resulting lines were assigned a goodness depending on how well their origins in the beam interaction region agreed with that of the best AX line. The BY lines were formed by matching up hits in C2BY with one or more hits in the B-side polymeter planes.

C. Momentum Analysis

The subroutine called MOMTM performed the principal part of the analysis of particles in the spectrometer. It first obtained the Y origin and angle phi corresponding to the AY line. It then scanned through (i) each AX line projecting into the magnet gap and (ii) each point in C4X and C5X, attempting to determine which line and which C4X and C5X points were the most likely combination corresponding to a particle traversing the spectrometer.

In addition to the three requirements mentioned for the AX line reconstruction, there was a somewhat overlapping requirement to be met in order for a particle to be further analyzed: Of the five AX chambers, the sum of the number of chambers without any hits and the total number of overflows must have been less than four. This requirement was inserted to eliminate a relatively large group of unreconstructable events surviving the previous cuts. Before this selection requirement was introduced, scans were made of unselected sequential events from the data tapes in order to insure that the number of possible reconstructable events rejected by this criterion was very nearly zero. Another rather obvious requirement for momentum analysis was that there must have been at least one hit in C4X or C5X.

In one way or another, all of the various momentum determination procedures used in the analysis made reference to a subroutine called BFIELD, which performed a calculation of the three-component magnetic field vector at any specified point in space. The functions used in this field calculation were determined by fitting the major features in the magnetic field map. A description of this fit is

contained in Appendix A.

Before the analysis program could determine the best fit trajectory for a particle in the spectrometer, it first had to assign a momentum value to each point in C4X or C5X corresponding to its deflection from the incoming AX line being considered. The mathematical relationship between the deflection in a chamber and the associated particle momentum had to be written into the analysis program. Using the magnetic field representation BFIELD, a number of imaginary particles of known location and momentum were integrated through the field in order to determine the deflection in each chamber as a function of the particle momentum and direction. Fits were made to these trajectories and the resulting functional relationships were written into the analysis program.

Each line-point combination was assigned a momentum value in the following manner. For a given incoming AX line and a given point in C4X or C5X the deflection from the initial direction of travel was calculated. From this the momentum value was estimated. This estimate of the particle momentum was then used to recalculate the incoming AX line with the C3X point adjusted to correct for the small deflection which occurred in the fringing field outside C3X. This deflection was typically in the neighborhood of one centimeter. With the initial AX direction adjusted, a new value for the C4X or C5X deflection was calculated and a more accurate estimate was made of the momentum.

The next step in the momentum analysis was to decide which AX line and which C4X point and C5X point were the most likely candidates for the particle trajectory. For a given AX line the momentum value

for each C4X point was compared pairwise with that of each C5X point. The pair of points having the closest agreement in momentum values was chosen as the most likely candidate for that AX line. If additional C4X or C5X points were present, the second best matchup was identified. It was stored if the C4X and C5X momentum values were reasonably consistent.

This procedure was repeated for each AX line found. Then the results for all lines were compared to find the trajectory candidate with maximum agreement in momentum values. If there was a viable trajectory having the second best line-point matchup, it was stored as a secondary candidate for further analysis.

Once the best trajectory candidate had been identified, a procedure was invoked to obtain the most precise possible momentum value. This involved using the reconstructed origin, initial particle direction and momentum to integrate the particle through the magnetic field represented by the BFIELD fit. As the integrated trajectory reached the location of each wire chamber, its position was recorded. These extrapolated locations were then compared with the actual wire addresses for the event. The differences were used to obtain better estimates of the initial position and momentum.

Because this integration procedure involved up to one-half second of computer time per trajectory, depending on the particle momentum, it was desirable to eliminate those events for which further analysis would yield no benefits. For this reason there were several requirements made on the best fit trajectory in order to insure that it corresponded physically to a particle traversing the spectrometer.

As shown in Fig. II-3, the amplitude of the magnetic field was such that the spectrometer solid angle was reduced to about 60% of its high momentum value when the particle momentum was 400 MeV/c, and dropped rapidly to zero at lower momenta. In addition it was observed that the one-particle inclusive backgrounds in the e^+e^- data were rising exponentially at lower momenta. For these reasons a cut was introduced requiring the particle momentum to be above 400 MeV/c. The initial cut, designed to pull out as much background as possible before integrating the trajectory, was set at 350 MeV/c to allow for a maximum of 50 MeV/c error in the initial momentum estimate. Thus, events having momentum lower than 350 MeV/c were dropped.

Occasionally, a nonphysical event--usually a spurious trigger--would return a very large or very small momentum value simply because it had invoked the initial momentum estimating procedures using deflections that were outside the physically meaningful range over which the momentum-vs-deflection fits were incorporated. The excessively low momentum values were eliminated as described in the previous paragraph. The high momentum values were eliminated by requiring the momentum to be less than 100 GeV/c. This limit allowed ample room for initial reconstruction inaccuracies to pass and included many cosmic ray muons. One further requirement on the C4X and C5X momentum values was that they must be within a reasonable range of agreement. Weeding out events with very high or very low average momentum did not get rid of those events having physically realizable average momentum values, but containing large disagreements between the individual C4X and C5X values. Allowing an ample margin

of error for chamber overflows and the effects of scattering, the requirement was made that the best fit C4X and C5X momentum values must be physically consistent. The precise definition of this consistency is given in Appendix F. This requirement was only applied to low momentum events.

If the event was considered worthy of more precise analysis, the trajectory integration procedure was entered. Following a comparison of the extrapolated trajectory with the real chamber coordinates, the positions in the chambers C1AX, C2AX and C3X were examined for possible corrections to the particle origin and initial direction of travel. If corrections were necessary, the new origin and direction information was input to an additional integration of the trajectory. Then the momentum value was improved until the integrated trajectory passed as close as possible to the C4X and C5X chamber hit addresses. The reconstruction error in the momentum was estimated from the differences between the hit locations and the extrapolated chamber coordinates. When the fit was sufficiently accurate to reduce this estimated momentum error to 0.5% of the momentum value, the fit was terminated.

If the extrapolated trajectory was found to lie on one side of the C4X hit and on the other side of the C5X hit after the momentum had been laid in as accurately as possible, and if the estimated reconstruction error was still greater than 0.5%, this was taken as evidence of the particle's having scattered in the material in front of the magnet. The presence of only two momentum measuring chambers did not provide sufficient information to allow a determination of the point of scatter, so it was assumed that the scatter

occurred at the most likely point: the exit window of the Cerenkov counter. With this assumption, the scatter was introduced and the momentum adjusted until the C4X and C5X points matched up with the extrapolated trajectory. After the events had been further classified, studies of the magnitude of the calculated scattering angle were undertaken which showed the observed distributions to agree with those expected from multiple Coulomb scattering and nuclear diffractive scattering. The scattering angle distribution for a sample of hadrons is shown in Fig. III-1 for two different momentum intervals. The smooth curves are Gaussian distributions calculated for small-angle multiple Coulomb scattering[3] and roughly normalized to the data. The non-Gaussian behavior of the data results from inaccuracies in the analysis program. The widths of the distributions appear to be in rough agreement with the predicted widths.

Once the selected trajectory was fit as closely as possible, an estimated fitting error was calculated for the final momentum value. This was normally less than 5 MeV/c. The total error was dominated by the uncertainties due to the wire spacing. If there was a second choice trajectory such that the difference between the initial momentum values assigned to the C4X and C5X hits was less than one and one-half that of the first choice trajectory, then the second choice was also subjected to the integration procedure. The final choice between the primary and secondary trajectories was made depending on the scattering angle. Whenever there was doubt about which trajectory the particle followed, the one with the smaller scattering angle was chosen.

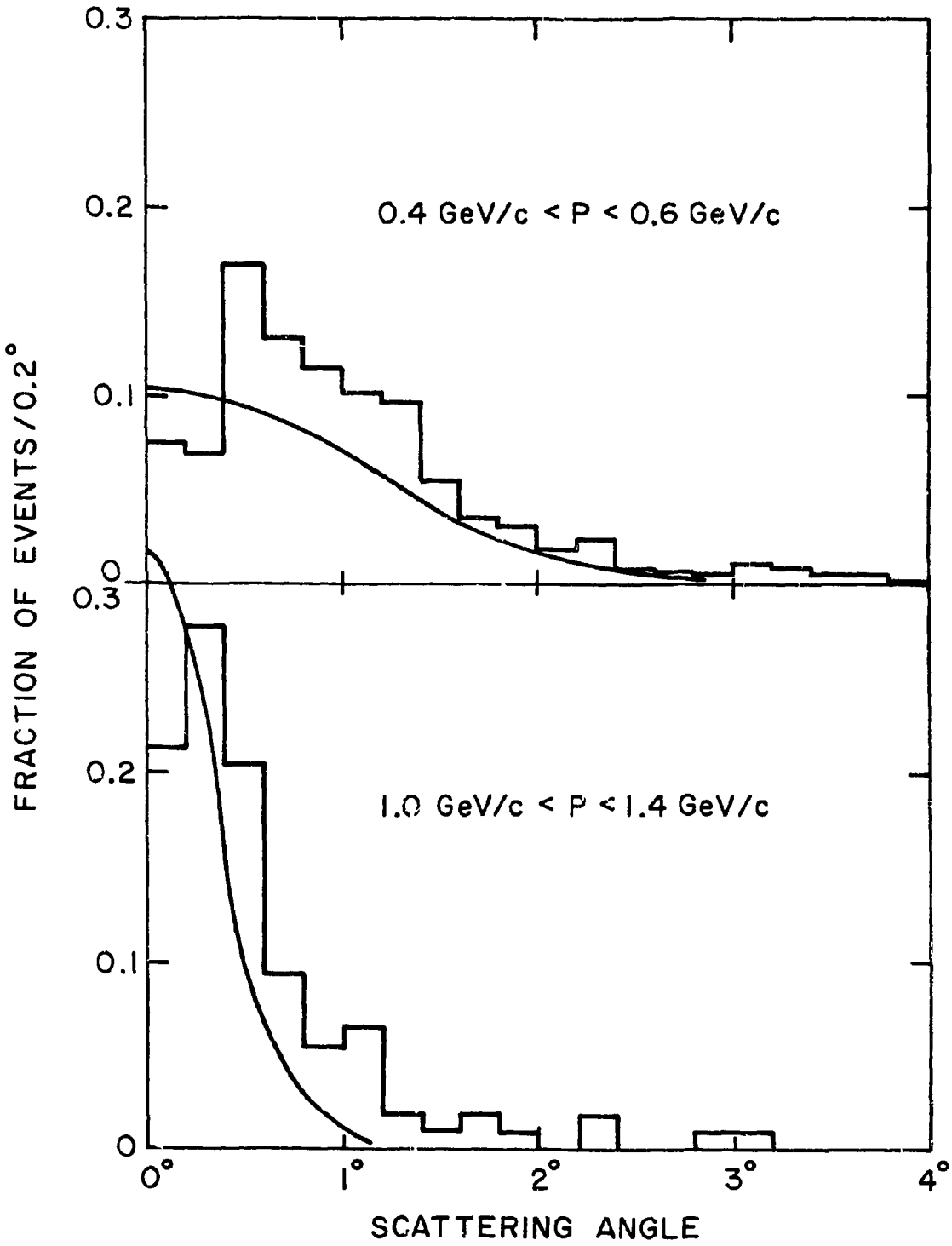

FIGURE III-1. The reconstructed scattering angle for two samples of hadrons in different momentum intervals. The smooth curves are Gaussian approximations to small angle multiple Coulomb scattering at the same momenta. The non-Gaussian behavior in the data resulted from the angle calculation procedures.

As the trajectory was integrated through the spectrometer, the particle position in each piece of the apparatus was recorded. If the chosen trajectory intersected the magnet wall at any point, the event was rejected from further analysis.

D. Polymeter Line Reconstruction and Charged Multiplicity Determination

The polymeter consisted of three planes of wires all running parallel to the beam. First all possible three-point lines were reconstructed, using the subroutine LFIT. The average standard deviation in the reconstructed origins was about 6 mm. This corresponded to an average angular error of 2.2^{o}. If any polymeter point was previously used in an AY or BY line, it was excluded from further fits. Once all three-point lines had been found, a search was made for all the remaining two-point combinations.

For each polymeter line, the extrapolated origin was calculated, and the reconstruction error was estimated based on which planes fired, how many wires were clustered to make each point and at what angle the line emerged. In order to restrict the number of point combinations formed into lines, all polymeter lines were required to have their reconstructed origins not more that one standard deviation beyond ±60 mm from the beam.

Once all the polymeter lines had been found, the charged multiplicity was calculated. A count was made of all the AY lines having at least three points, at least one of which was outside the polymeter. Another count was made of all BY lines, containing a point in C2BY and at least one point in the polymeter. To these was added the sum of all lines formed in the polymeter alone, such that

their origins were within four standard deviations of the beam. This particular reconstruction cut was made after studying a sample of hadron events and positioning the cut in order to maximize the number of events having an even number of charged prongs.

One problem that particularly affected the higher multiplicity events was the occurrence of overflows in the polymeter, resulting in an underestimate of the multiplicity for those events. A statistical correction for this effect is described in connection with the hadron multiplicity analysis in Section VI-G.

E. Final Event Selection

In addition to the event selection criteria mentioned previously, which dealt with trajectory reconstruction in the wire chambers, there were several criteria applied to the spectrometer shower counter amplitudes. As was the case with the requirements on trajectory reconstruction, these shower counter requirements were imposed in order to eliminate certain types of unreconstructable or background events.

The nature of the counter reset electronics, designed to clear out the ADC's if an event failed the trigger requirements, was such that on rare occasions a new event was read in before the previous data erasure was completed. This resulted in the recording of an event where all the counter amplitudes were identically zero. To eliminate these events early in the analysis, a test was made to insure that all the spectrometer shower counters had been digitized.

Two other requirements were made on the dE/dx calculation results after a study of the events reaching that stage of the analysis. Some

of the background events were such that the particle in the spectrometer would pass above or below the S1 counter, the trigger being satisfied only because that counter was slightly above the pedestal level during that event. To eliminate these events the requirement was made that the dE/dx value in S1 must be greater than 0.2 times minimum ionizing. The significance of this cut is shown by Fig. III-2,a. In a similar vein, the requirement was made that the dE/dx for the three shower planes having the smallest amplitudes must be greater than 0.1 times minimum ionizing, as shown in Fig. III-2,b. This in effect required that a spectrometer particle or its secondaries penetrate at least two shower counter planes.

After all the events were analyzed, a visual check was made of each passed event. The conservative philosophy of allowing the analysis software to veto an event only if it was clearly indecipherable inevitably resulted in the passing of a small number of marginal events. During the visual examination, such marginal events were dropped for any of three reasons: (i) No consistent momentum value could be found; (ii) The trajectory origin could not be reconstructed; or (iii) For some reason, probably a failure of the veto for the west pit spark chambers, all or most of the counters registered hits, making the event indecipherable.

This final visual scan rejected about 3% of the remaining triggers. Those events surviving were for the most part relatively clean and reconstructable. A sizeable number of background events remained in the sample at this point--about 30% of the total--but more that 80% of these fell outside the origin cut that was later adopted. The next task, described in Chapter IV, was to identify

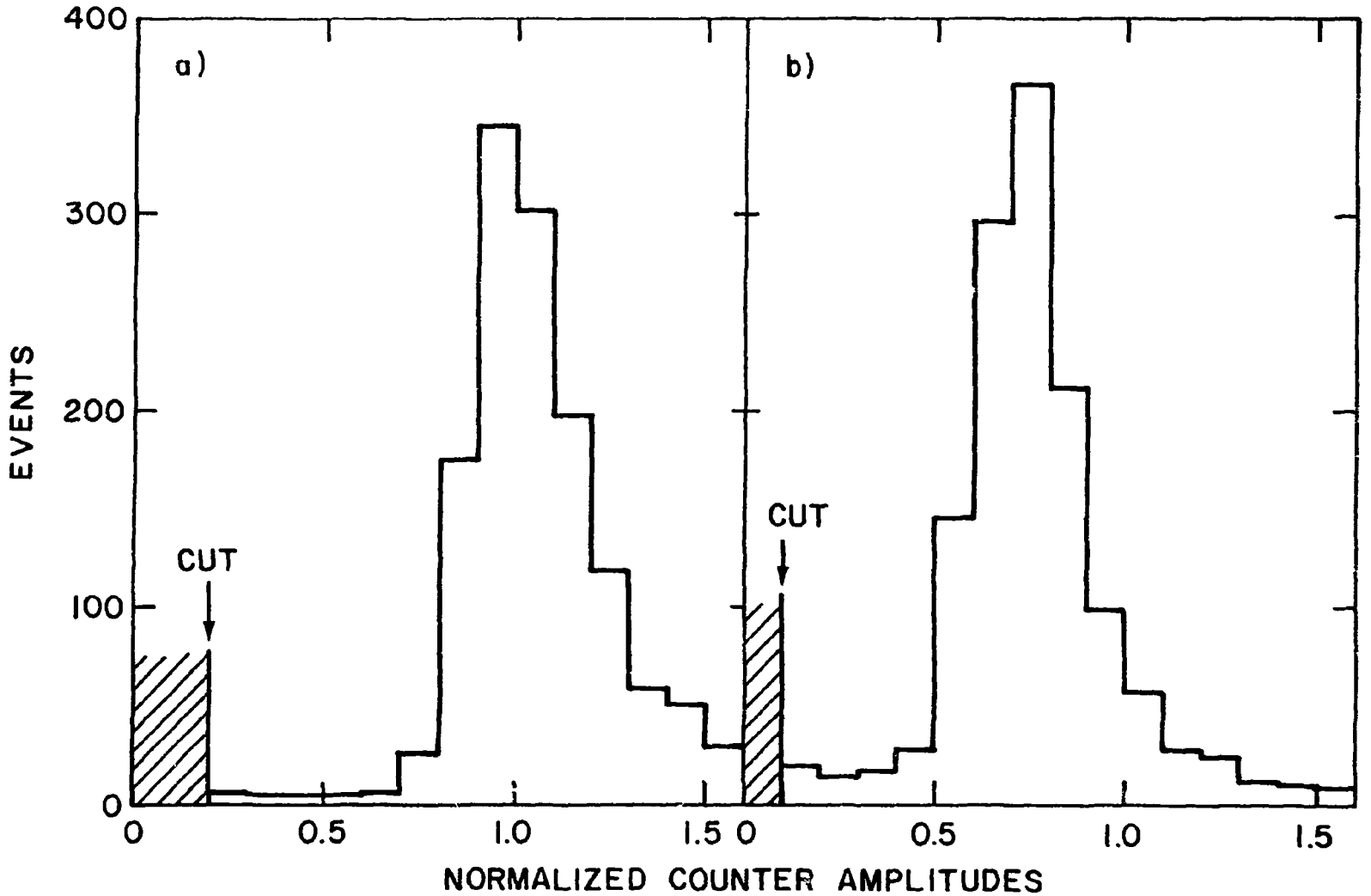

FIGURE III-2. The positioning of the cuts in the energy loss distributions in (a) the S1 counter and (b) the average of the three shower detector planes having the lowest amplitudes. The high-amplitude tails in each distribution are not shown.

each of the particles in the spectrometer.

REFERENCES

CHAPTER III

1. P. R. Bevington, "Data Reduction and Error Analysis for the Physical Sciences", McGraw-Hill Book Co. (1969), pp. 104,5.
2. W. T. Eadie, D. Drijard, F. E. James, M. Roos, and B. Sadoulet, "Statistical Methods in Experimental Physics", North-Holland Publishing Company (1971), p. 72.
3. Particle Data Group, Rev. Mod. Phys., 48, S45 (1976).

CHAPTER IV

PARTICLE IDENTIFICATION

A. Introduction

The identity of the spectrometer particle in each of the reconstructed events was determined through a two-stage process. First the events were separated into classes of electrons, muons and hadrons according to the classification criteria that will be developed in this chapter. These criteria involved the behavior of the spectrometer particle in the Cerenkov counter, the shower detector and the hadron filter. Once this had been accomplished, the hadrons were further identified as pions, kaons or protons through their behavior in the Cerenkov counter and the time-of-flight system.

By making stringent cuts in various measured quantities it was possible to obtain highly purified samples of hadrons, muons or electrons. This procedure is discussed in Section B. These "pure" samples were used to examine the properties of the various spectrometer components in order to establish more general criteria that would lead to an efficient classification scheme. The properties of the shower detector affecting particle identification are described in Section C. Section D describes the performance of the hadron filter, used principally for distinguishing muons. Properties of the Cerenkov counter related to particle classification are discussed in Section E.

The implementation of the particle classification criteria is discussed in Section F. That section describes the separation of the entire data sample according to whether the spectrometer particle was a muon, electron or hadron. The misidentification probabilities

were calculated for each particle type based on the properties of the purified samples. Care was taken to insure that these calculations were not biased by the cuts used to obtain the purified test samples. The further separation of hadrons into pions, kaons and protons is described in Section G.

In order to avoid the introduction of biases during the final identification process, very little use was made of the information on particles other than those actually traversing the spectrometer. The only such cases where multiplicity and conjugate-side shower detector information was used was in the tagging of back-to-back electron and muon pairs.

B. Selection of "Pure" Samples of Muons, Hadrons and Electrons

In order to establish the criteria to be used for particle identification, it was desirable to select pure samples of electrons, muons and hadrons and to examine their properties in various parts of the apparatus. The muon sample was relatively easy to isolate; this procedure is discussed in Section E, and mainly involved the requirement that the spectrometer particle penetrate the hadron filter. To insure a "purified" muon sample, the additional requirement was made that a second muon must have penetrated the conjugate-side hadron filter.

A highly pure sample of hadrons was isolated simply by requiring the Cerenkov counter amplitude to be near the pedestal level. The only contaminants to these hadrons were muons with momenta less than about 800 MeV/c, which was the Cerenkov threshold for muons. Since the origin of the hadron was immaterial for a study of the shower detector, no origin cuts were made at this point.

The selection of a pure electron sample was somewhat more difficult since, for a study of the shower detector, its amplitude could not be used as a tag. The requirements made for electrons were that the Cerenkov amplitude was above 90 (on a scale of 255), the charged multiplicity was exactly 2, and the two tracks were coplanar within 3^{o}. Whenever there were significant doubts about the purity of this electron sample, the additional requirements were made that the shower amplitude of the conjugate-side shower detector was high, and that the two tracks were collinear within 3^{o}. The presence of about 0.3 radiation lengths of material in the Cerenkov counter and other apparatus between the interaction region and the magnet produced substantial degradation of the electron momentum spectrum, resulting in a continuous electron momentum range, as shown in Fig. IV-1. This was advantageous for studying the shower detector performance as a function of momentum.

C. Calibration and Performance of the Shower Detector

The primary function of the shower detector was to identify electrons in the spectrometer by their characteristic of producing large showers. In order to obtain maximum information from the shower detector, the output of each of the 20 scintillation counters comprising the detector was normalized. The detector performance characteristics were studied by selecting highly pure samples of electrons, muons, and hadrons from the data and examining the shower amplitudes of each type of particle. The present section details the calibration procedures applied to the shower counters and the nature of the various cuts used to identify events; the actual

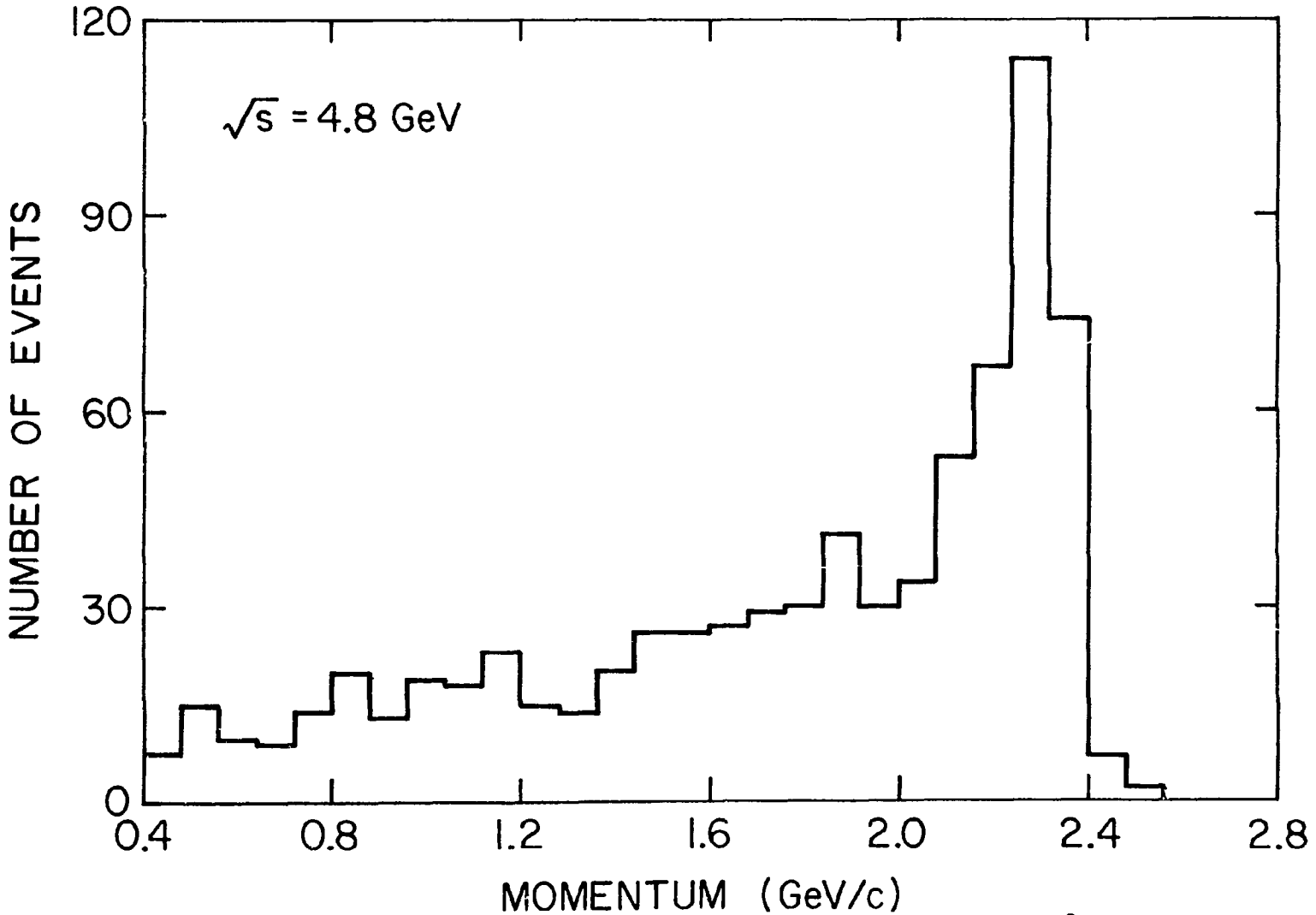

FIGURE IV-1. Momentum distribution of electrons collinear within 3^{o}.

implementation of these cuts is discussed in Section F.

The normalization of the shower detector took several factors into account. The relatively large size of the scintillation counters dictated an amplitude correction to compensate for differing optical attenuation in the scintillator, depending upon the position where the particle traversed the counter. This correction was determined before the apparatus was assembled by mapping the counter performances using cosmic rays with various points of incidence. As a check, the positional dependence of the counter amplitude was examined using muons in the data. The analog-to-digital converter (ADC) pedestal or zero levels were subtracted from each counter amplitude value, and the amplitudes were compensated for the angle of incidence of each spectrometer particle.

In order to confirm that the shower detector performance was well understood, the normalized amplitudes for collinear muons at 2.4 and 2.5 GeV/c were fit to a Landau distribution.[1] This fit is shown in Fig. IV-2. The most probable total energy loss for these muons in the shower detector was calculated to be 103 MeV at normal incidence. About 30% of this energy was deposited in the scintillation counters.

A plot of the normalized shower detector amplitude for electrons as a function of momentum is shown in Fig. IV-3. The expected behavior[2] is that the mean electron energy loss should be proportional to the momentum. The leveling off at high momentum is explained by the saturation of the counter ADC's at large amplitude. A histogram of energy loss for the pure hadron sample is shown in Fig. IV-4.

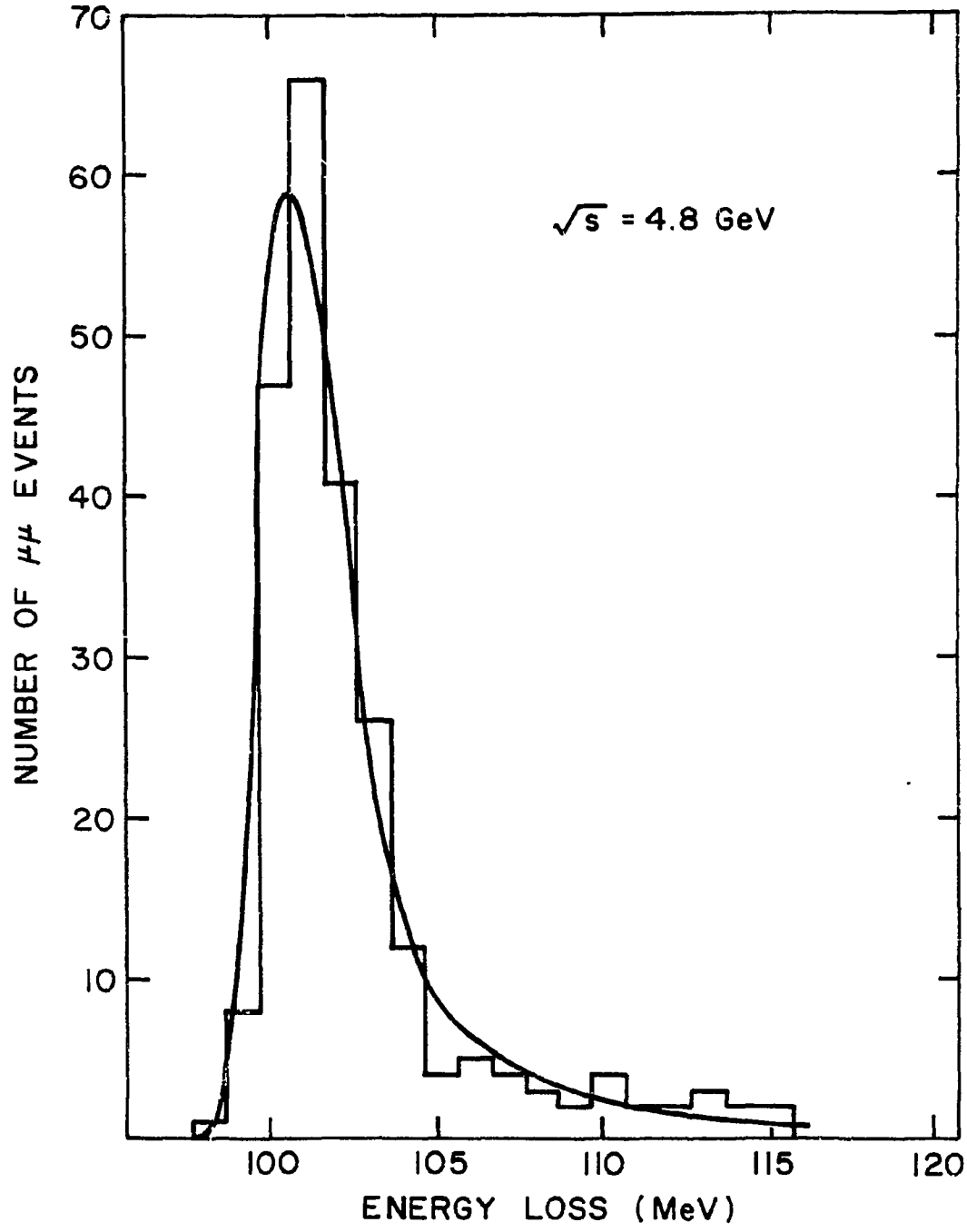

FIGURE IV-2. Energy loss distribution in the spectrometer shower detector for high momentum muons. The solid curve is a fit to a Landau distribution.

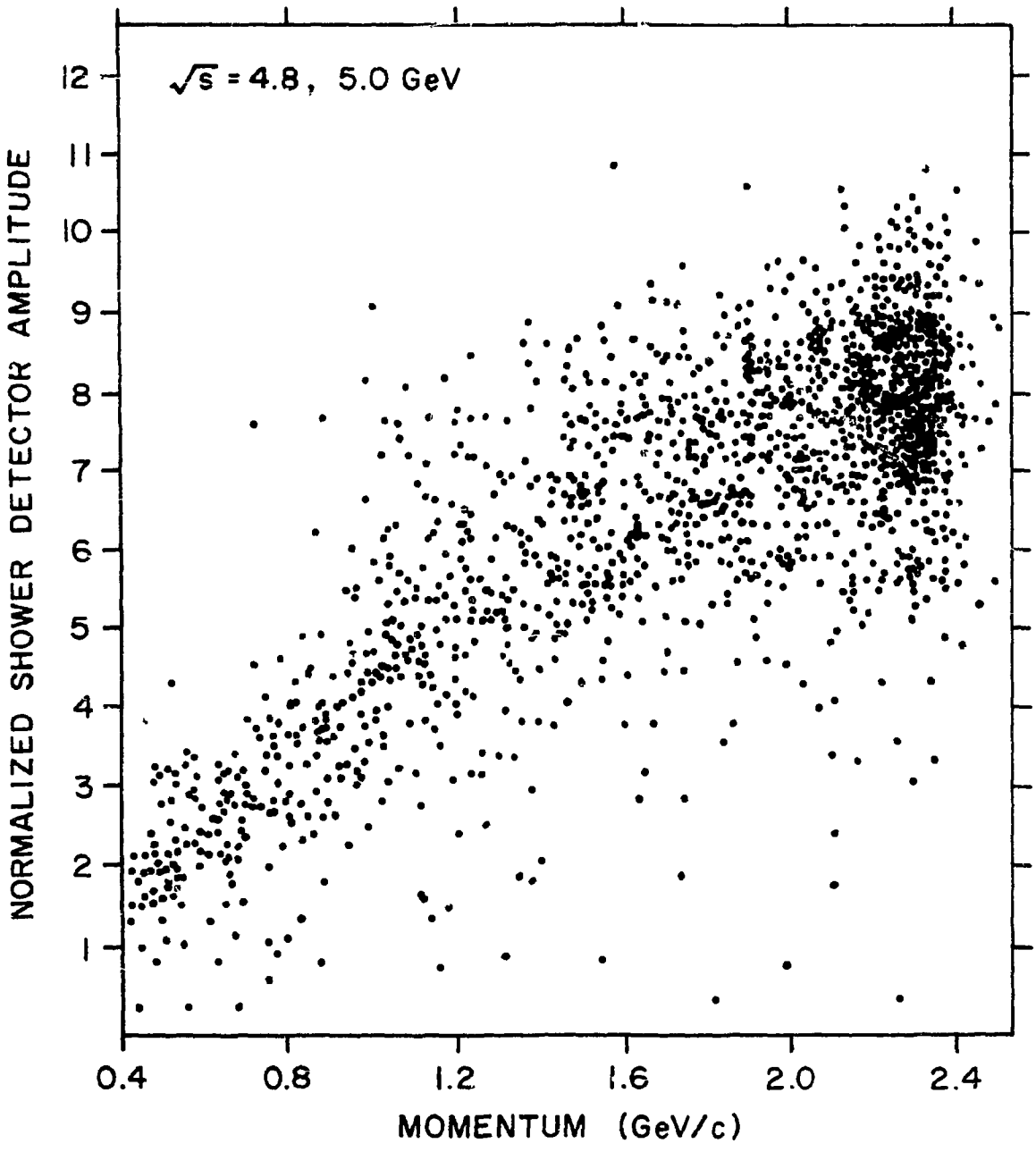

FIGURE IV-3. Energy loss in the spectrometer shower detector for coplanar electrons as a function of momentum. The high amplitude levels were limited by ADC saturation effects.

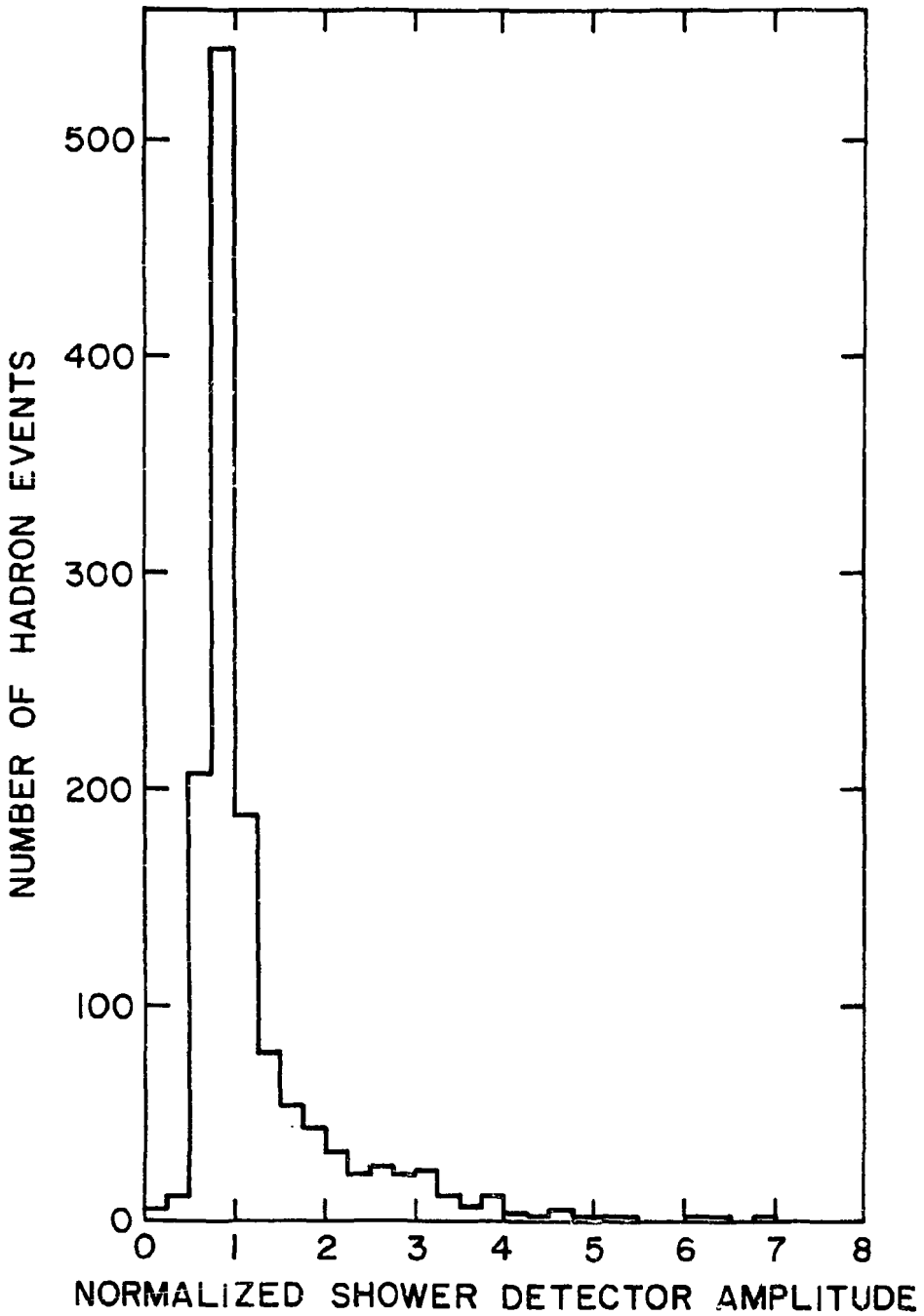

FIGURE IV-4. Energy loss distribution in the spectrometer shower detector for hadrons.

The major problem leading to confusion of hadrons and electrons resulted from the large amplitudes produced when hadrons underwent nuclear interactions. A completely clean separation could have been achieved by simply requiring that the amplitude in each counter be below a certain level for hadrons. However, this would have resulted in the loss of about one-third of the hadron data, including almost all the hadrons that interacted.

A less severe constraint was adopted, essentially requiring the hadron to penetrate only the first two shower counter planes before interacting, resulting in a removal of 13.4% of the pure hadron sample and 99.3% of the sample of coplanar electrons with momenta above 1.2 GeV/c. By invoking this requirement only when the Cerenkov counter was above pedestal, a much smaller hadron data depletion resulted. This two-counter amplitude cut physically corresponded to the requirement that the total energy loss in each of the first two shower detector planes was less than about 60 MeV per plane, or roughly three times mimimum ionizing.

Because of the different energy loss mechanisms involved for electrons and hadrons, the variation in energy loss among the different counters traversed provided a helpful tool for distinguishing some of the hadrons from electrons. Fig. IV-5 shows histograms of the mean squared deviation of the five normalized scintillation counter amplitudes for electrons and hadrons. Unlike the electrons, most of the hadrons were concentrated in the lowest bin. In particular, 59.2% of the hadrons were in this bin, while only 0.1% of electrons with $p > 1.2$ GeV/c and 0.4% of electrons with $0.4 \leq p \leq 1.2$ GeV/c were there. The requirement that a particle have an amplitude

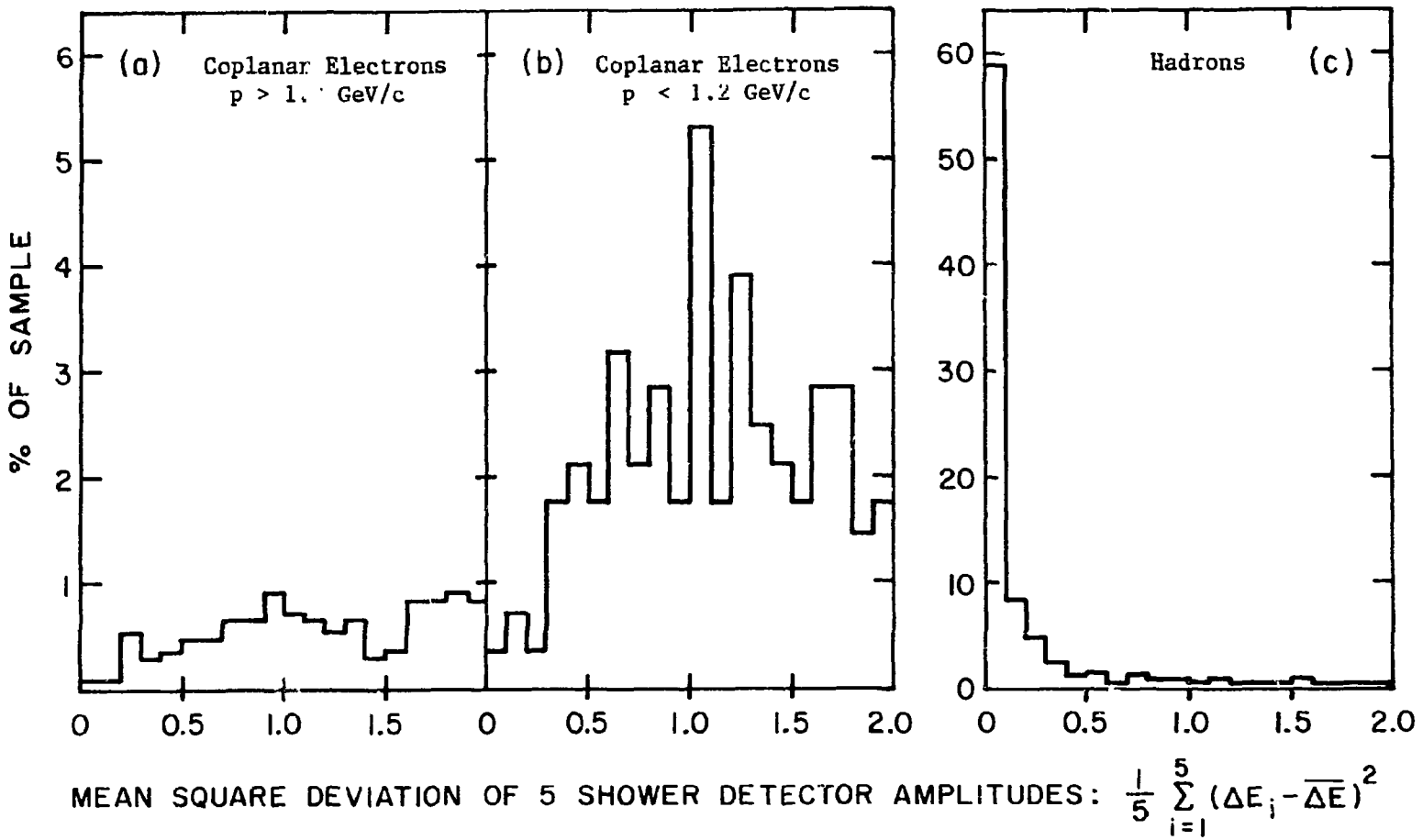

FIGURE IV-5. Distributions of the mean squared energy loss fluctuations in the spectrometer shower detector for (a) coplanar electrons with momentum greater than 1.2 GeV/c; (b) coplanar electrons with momentum less than 1.2 GeV/c; and (c) hadrons. The vertical scale represents the fraction of the events in each sample contained in each bin. Observe that the electrons and hadrons are plotted on different scales and that the distributions only show that portion of each data sample having the lower fluctuation values.

fluctuation less than 0.1 corresponds to an r.m.s. fluctuation in the sampled energy loss of about 5 MeV at normal incidence.

Fig. IV-6 shows a two-dimensional plot of the mean squared counter fluctuation versus the total energy loss for electrons and hadrons. Evidently there is a region of high fluctuation in this plot (above the line in Fig. IV-6) where some interacting hadrons are present and no electrons are. Using the arbitrarily defined units of Fig. IV-6, these hadrons have the property that

$$\sigma^2 \equiv \frac{1}{5} \cdot \sum_{i=1}^{5} (\Delta E_i - \overline{\Delta E})^2 > \frac{50\overline{\Delta E} - 25}{12} \quad ,$$

which defines the cut. The quantity $\overline{\Delta E}$ is the normalized shower detector amplitude and σ is the r.m.s. deviation from the mean energy loss $\overline{\Delta E}$ averaged over the five counters traversed. The use of this cut allowed the recovery of many of the interacting hadrons that would otherwise have been removed from the sample due to their high shower amplitudes.

The most obvious cut, though unfortunately not the most efficient, for separating electrons from hadrons was to cut on the total energy loss. Because the electron losses are proportional to the momentum, the separation efficiency is highly momentum dependent. In the worst case, at 0.4 GeV/c, a cut corresponding to an energy loss of about 0.2 GeV misidentifies electrons and hadrons with equal probabilities of about 30%. Because of substantial overlap with some of the other cuts, this cut in the total energy loss was not invoked, except to tag electrons with an amplitude higher than that observed for any hadron.

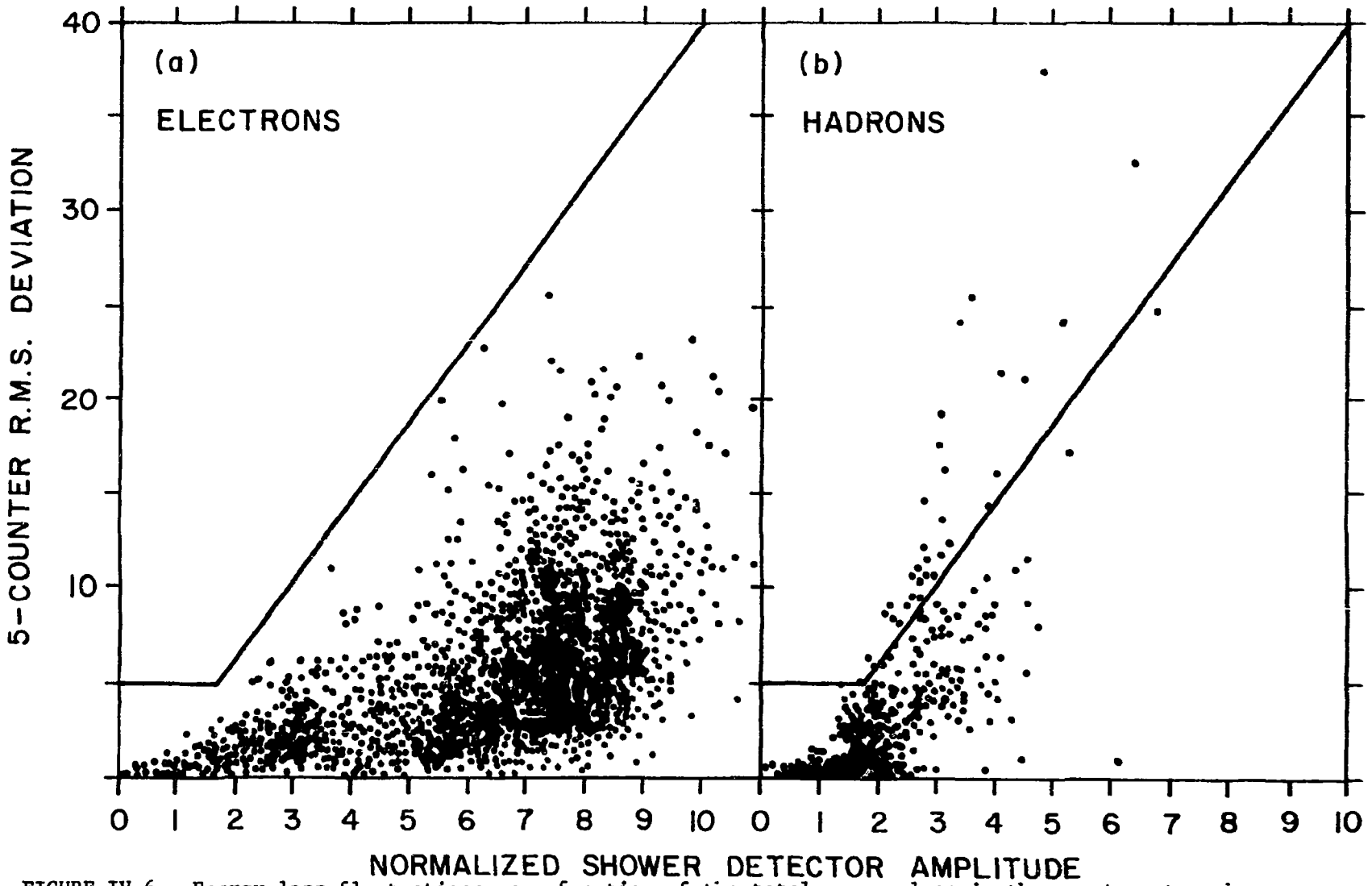

FIGURE IV-6. Energy loss fluctuations as a function of the total energy loss in the spectrometer shower detector for (a) coplanar electrons and (b) hadrons. The samples are roughly equal in size and range over all observed momentum values above 0.4 GeV/c. The solid lines in each plot are identical and indicate the positioning of the cut used to separate some of the hadrons.

The actual implementation of the various shower detector cuts and their effects upon the final data samples are described in detail in Section F.

D. Performance Characteristics of the Hadron Filter

Except for those hadrons which underwent nuclear interactions in the shower detector, the energy loss rates for hadrons made them indistinguishable from muons. In order to isolate the muon events, an iron hadron filter was installed behind the shower detector, as described in Section II-G. It was designed to attenuate hadrons via range and nuclear interaction effects, while being transparent to high momentum muons.

In order to determine the probability of hadron penetration, several effects were taken into account: (1) The amount of material traversed depended on the angle of incidence. (2) The particle penetration was range limited to within the uncertainties due to straggling. (3) If the particle had sufficient range, its penetration probability was limited by the occurrence of nuclear interactions. (4) Both range and nuclear interaction effects were dependent on the particle momentum. (5) The possibility of the subsequent penetration of secondaries produced in a nuclear interaction was implicitly accounted for by basing the calculations of attenuation probability for observed hadrons upon experimental results[3,4] incorporating such effects.

An expression for the momentum-dependent probability for pions penetrating iron was obtained by making a four-parameter fit to the data of Ref. 3 for momenta from 0.6 to 2.0 GeV/c. The probability

for a pion of momentum p (GeV/c) to penetrate x centimeters of iron was expressed as

$$P(p,x) = \exp\left[\frac{x_o - x}{\lambda}\right] \quad ,$$

where

$$x_o = 1.80 + 3.60p \quad ; \quad \lambda = 13.0 + 4.74p \quad .$$

When this calculation was applied to observed hadrons, the total pathlength in iron equivalents traversed in reaching a given plane was corrected for the angle of incidence. The fit was made to the average values of incident pi+ and pi- penetration probabilities. The different penetration probabilities for kaons were ignored because of the small number of such events relative to pions and because they were much more range limited. No observed proton had sufficient range to penetrate to the second row of counters in the hadron filter.

The total penetration probability for a given observed hadron was obtained by multiplying the attenuation probability just described by the probability that the hadron had sufficient range to penetrate. The probability that a muon of momentum p had sufficient range to penetrate a thickness x of iron was represented as

$$P(x,r) = \frac{1}{\sqrt{2\pi}\cdot\sigma} \int_x^\infty \exp\left[-\tfrac{1}{2}\left(\frac{y - r}{\sigma}\right)^2\right] dy \quad ,$$

where r was the most probable range, and σ represented the width of the straggling distribution, assumed to be Gaussian. The r.m.s. range fluctuation was roughly fit to the data of Ref. 5:

$$\sigma \simeq (0.07 - .012p)\ r \quad ,$$

where σ is expressed in cm and p in GeV/c. To make this expression applicable to hadrons, the correct value for the most probable range r was substituted, and the width of the straggling distribution was corrected via the equation[2,4]

$$\sigma = \sqrt{200 m_e/M}\ f(E/Mc^2)$$

for a particle of mass M and energy E. For example, the r.m.s. range fluctuation for high momentum pions was calculated according to

$$\sigma_\pi(p) \simeq \sqrt{M_\mu/M_\pi}\ \sigma_\mu(pM_\mu/M_\pi) \quad .$$

The mean muon momentum corresponding to a range just sufficient to penetrate the entire hadron filter was calculated to be about 1.05 GeV/c[7] and was dependent on the muon angle of incidence. Lower energy muons penetrating only two hadron filter planes could still be tagged by requiring the Cerenkov counter to be above pedestal. The identification of these low-momentum muons is discussed more fully in Section F. Fig. IV-7 shows histograms of muons which penetrated two or three planes as a function of the calculated most probable range and expected straggling error.

E. Performance Characteristics of the Cerenkov Counter

The principal function of the Cerenkov counter was the separation of pions in the spectrometer from kaons and protons. The momentum range over which this discrimination was possible was determined by the Cerenkov threshold momenta for different particles. The

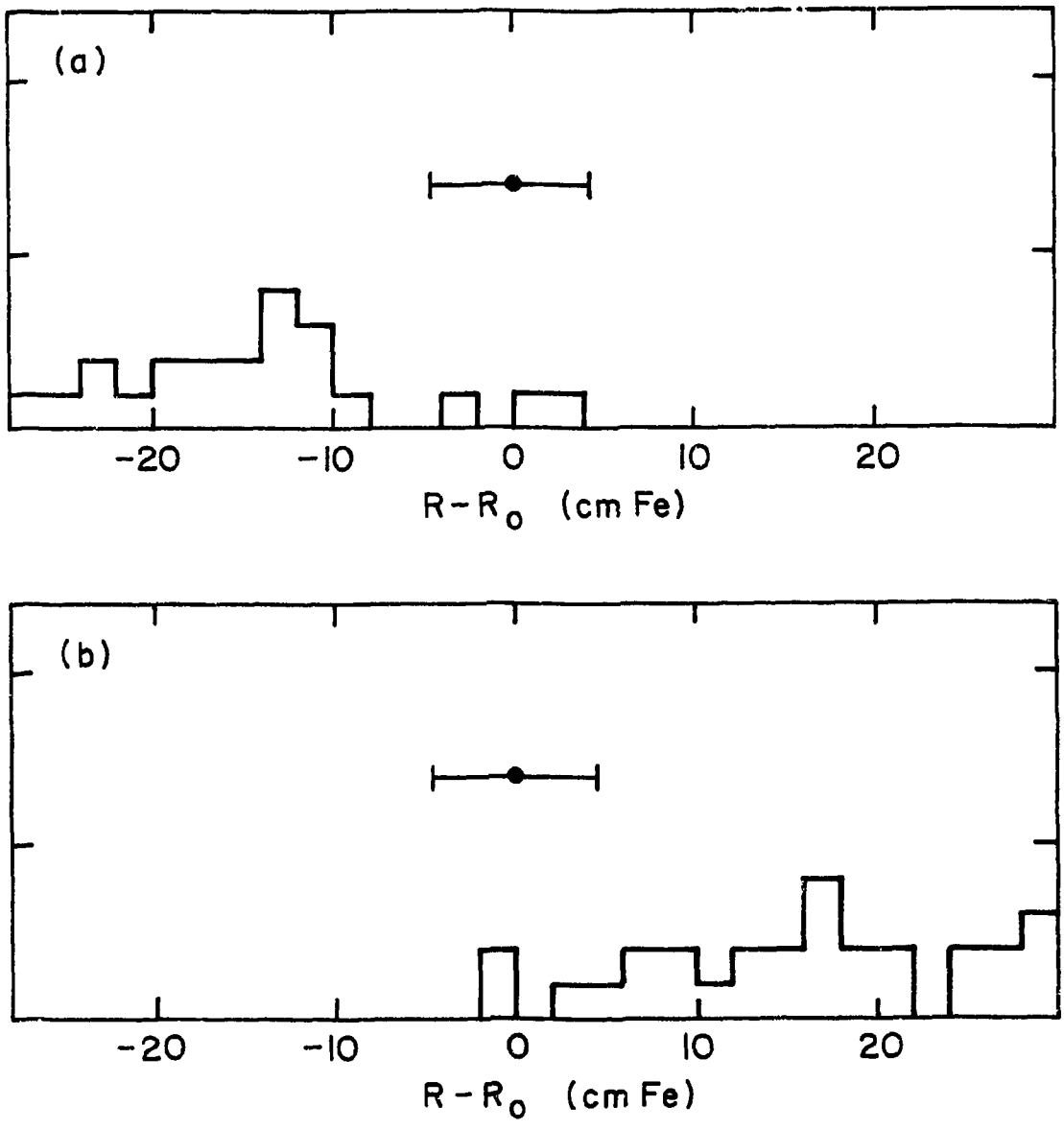

FIGURE IV-7. Distributions of the total calculated range in the hadron filter for (a) muons observed to penetrate only the first two scintillation counter planes and (b) muons observed to penetrate all three planes. The value zero represents the thickness of iron which the muon would have traversed if it had penetrated the entire hadron filter. The error bar represents the standard deviation of the straggling distribution.

calculated threshold momenta were:

Electron	.004 GeV/c
Muon	.80 GeV/c
Pion	1.05 GeV/c
Kaon	3.71 GeV/c
Proton	7.04 GeV/c

Small variations in the propane density during the course of the experiment resulted in minor fluctuations in the index of refraction, causing the pion and muon thresholds to fluctuate upward by as much as 25 MeV/c in the extreme. This effect, together with the statistical fluctuation in photoelectron production near threshold, necessitated the use of a practical threshold about 100 MeV/c above the calculated value.

Another major function of the Cerenkov counter was the identification of muons in the momentum range $0.80 < p < 1.05$ GeV/c, where the muons only penetrated two planes of the hadron filter. For 100% of the muons to be tagged required a practical threshold of 0.90 GeV/c, although some muons could be distinguished below this level.

Because the Cerenkov counter tagged electrons over the entire observed momentum range, it was also very useful in distinguishing electrons from hadrons below the pion threshold momentum. In principle, the Cerenkov counter might have been expected to be entirely sufficient to perform the low-momentum separation. In practice, however, there were several effects that produced spurious signals in the Cerenkov counter, which were not directly attributable to the charged particle traversing the spectrometer. One such effect was the production of delta rays as the particle passed through the

material of the counter. A somewhat larger effect was the conversion of gamma rays produced by the e^+e^- interaction.

An estimation of the likelihood of a particle producing a delta ray Cerenkov signal was obtained by calculating[2] the number of electrons produced with momentum greater than the 4 MeV/c Cerenkov threshold for electrons. For simplicity, the angle of delta ray production was ignored; the 4 MeV cut would force most of the secondary electrons to be sufficiently forward to strike the Cerenkov counter mirror. The result was an estimated 0.68% contamination averaged over the delta-ray energy distribution.

Another cause of accidental signals in the Cerenkov counter was the conversion of gamma rays associated with the event. An upper limit for this effect could be calculated using the high momentum pair production cross section,[2]

$$\sigma_{pair} \simeq \frac{7}{9}\cdot\frac{1}{NX}$$

where N is the number of atoms per gram and X is the radiation length in gm/cm^2. At normal incidence there were 0.17 radiation lengths of material between the beam and the Cerenkov counter mirror. If the average number of gamma rays produced in an event was n and the effective solid angle subtended by the Cerenkov mirror from the interaction region was Ω, then the probability of having produced a converted electron or positron in the Cerenkov counter was

$$P(n) = \frac{n\Omega}{4\pi}(1 - e^{-.132}) = .0033n \quad .$$

Thus for an average of 4 gammas per event, 1.3% of the events would have contained contaminated Cerenkov signals from this source.

A third source of contamination resulted from the passage of charged particles through the plexiglass pressure plate in front of the photomultipliers. The resulting Cerenkov radiation could have excited the photomultipliers, producing a spurious signal. This plexiglass plate was 2.5 cm thick and subtended an effective solid angle of .066 sr from the interaction region. Assuming an average of four charged prongs per event, one of which traversed the spectrometer, the average probability of contamination was 2.1% per event. This assumes that every charged particle passing through the plexiglass plate produced at least one photoelectron.

Some other effects which would also have produced contamination in the Cerenkov counter were i) the presence of additional charged particles in the Cerenkov counter, ii) passage of charged particles through the photomultiplier enclosure, and iii) conversion of gamma rays in the iron magnetic shield surrounding the photomultipliers.

The Cerenkov counter amplitude distribution is shown in Fig. IV-8(a) for a sample of collinear electrons. In Fig IV-8(b) is shown the distribution for all hadrons with momenta less than 1.0 GeV/c. About 3.8% of the low-momentum hadrons had spurious Cerenkov amplitudes high enough to overlap the electron distribution. The Cerenkov amplitude for all hadrons as a function of momentum is shown in Fig. IV-9.

F. Separation of Hadrons, Muons and Electrons

The identification of particles as hadrons, muons or electrons was accomplished by introducing the various cuts on the Cerenkov

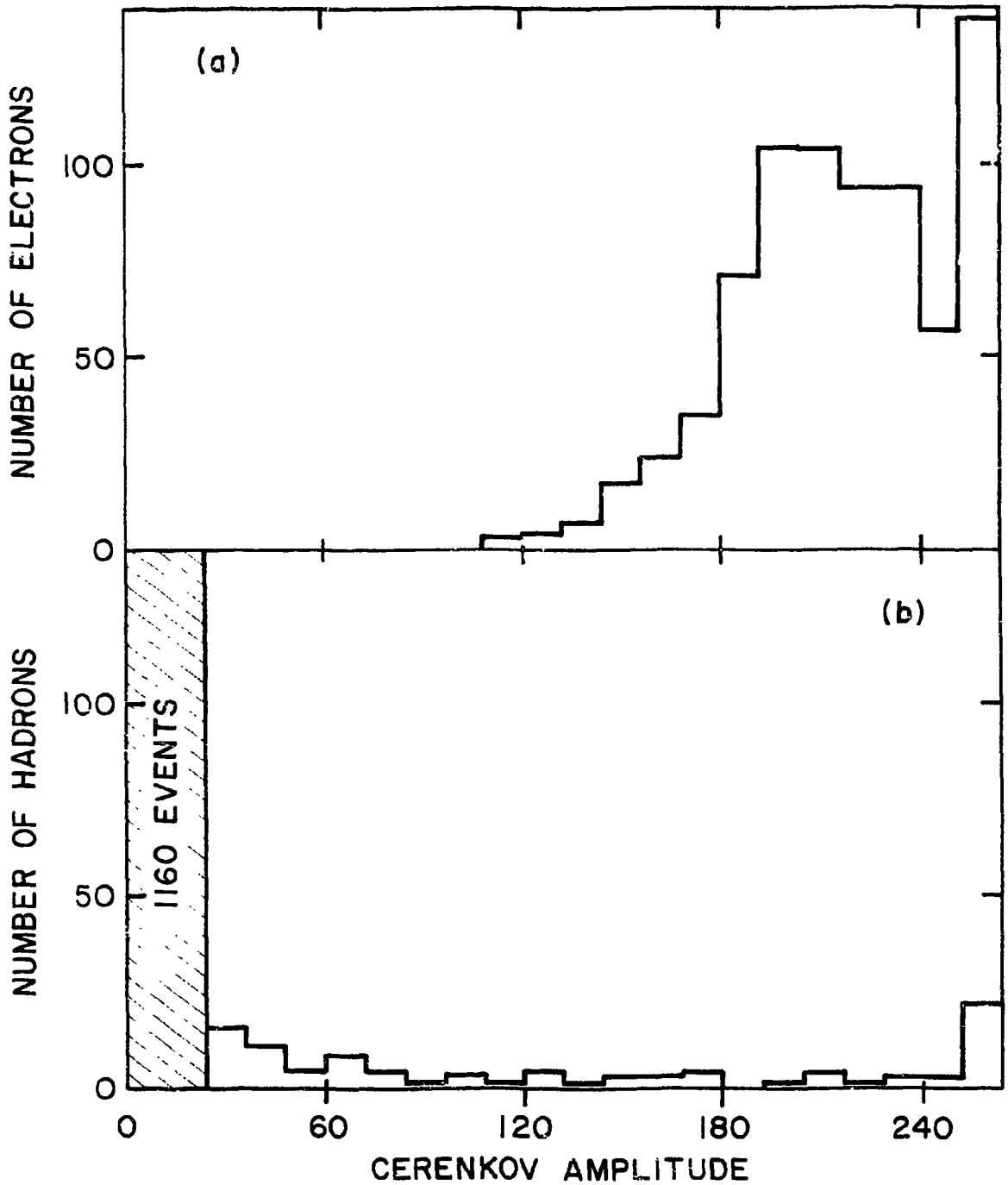

FIGURE IV-8. Cerenkov counter amplitude distribution for (a) a sample of collinear electrons and (b) hadrons with momentum from 400 to 1000 MeV/c. The large number of events in the rightmost bin results from ADC saturation.

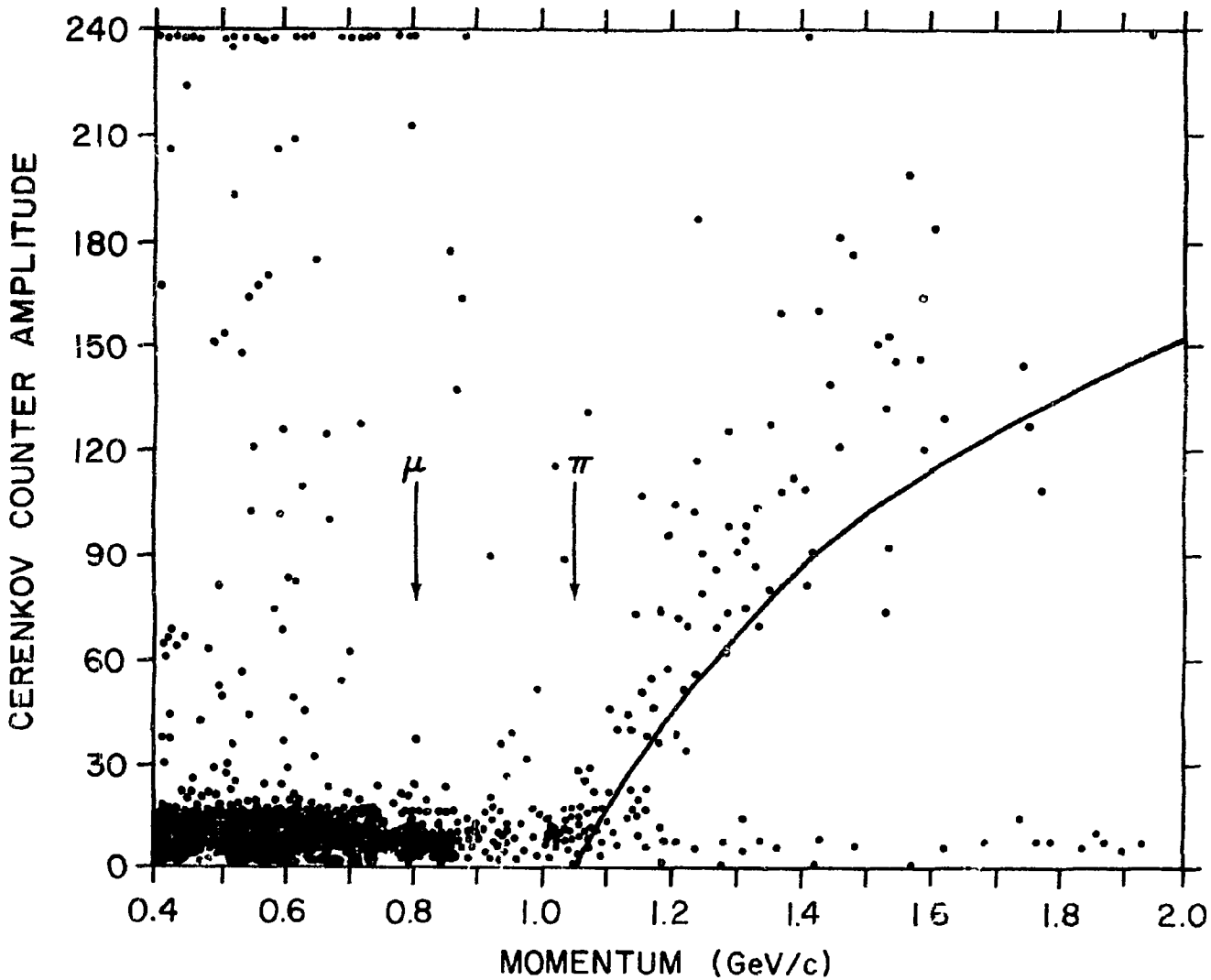

FIGURE IV-9. Cerenkov counter amplitude as a function of momentum for all hadrons. Vertical arrows indicate the calculated muon and pion thresholds. The solid curve is the estimated pion amplitude. The discrepancy between the line and the data results from the different detection efficiency for the high-amplitude electrons used for normalization. The total number of events plotted is 1412.

counter, the shower detector and the hadron filter, which have been described in the previous three sections. Once the hadrons had been isolated, they could be further identified as pions, kaons or protons using the information provided by the Cerenkov counter and time-of-flight system. This hadron identification will be discussed in Section G.

The most straightforward identification procedure was that applied to muons. The hadron filter was of such a thickness that muons would penetrate it if they had momenta greater than about 1.05 GeV/c, the precise value depending upon the angle of incidence and straggling effects. Thus any event with signals in all three scintillation counter planes of the hadron filter was called a muon. Each plane of scintillators was segmented into five adjacent counters, and the requirement was made that the signal in each plane must have come from a counter associated with the charged particle track in the spectrometer. In addition, for all muons with momenta above 1.05 GeV/c the Cerenkov counter was required to be above pedestal, and the normalized shower detector amplitude was required to be less than 3.0 on the scale shown in Fig. IV-4. None of the observed collinear muon pairs had an amplitude higher than about 2.5.

For momenta below 1.05 GeV/c and above 0.80 GeV/c muons were tagged, although somewhat less efficiently, by requiring that the Cerenkov counter was above pedestal, that the total energy loss in the shower detector was consistent with a noninteracting particle, and that two planes of the hadron filter were penetrated. This procedure tagged nearly 100% of muons down to 0.9 GeV/c and some muons down to the Cerenkov threshold of 0.8 GeV/c.

The principal contaminants to the final muon sample were hadrons which either decayed to muons in the spectrometer or penetrated all three hadron filter planes. Contamination of the muons with momenta below 1.05 GeV/c also resulted from those low momentum hadrons which penetrated two hadron filter planes and had accidental signals in the Cerenkov counter. The magnitudes of these contaminations will be calculated in succeeding chapters during descriptions of the cross-section determination procedures.

Once the muon sample had been isolated (along with a few contaminating hadrons) all the remaining events were either electrons or hadrons. Exceptions to this statement were those muons below 0.9 GeV/c which could not be explicitly tagged. The first step in separating the electrons and hadrons was to segregate those events which were unambiguous electrons. These had the following requirements: They i) were coplanar within 3°, ii) had a Cerenkov amplitude above 90, iii) had a charged multiplicity value of 3 or less, iv) either had an energy loss greater than about 400 MeV corresponding to a normalized shower detector amplitude of 2.5 or had a mean square energy loss fluctuation greater than 0.1 (see Fig IV-6a), and v) had an amplitude above 600 in the conjugate side shower detector. Only minimal cuts in the spectrometer shower detector amplitude were used, so that large biases would not be introduced into the dE/dx distribution of that portion of the electrons which at this point had not yet been separated from the hadrons. This facilitated estimates of contamination levels in the remaining sample based on the known properties of the pure samples of hadrons and electrons.

Once this large and relatively easily identifiable group of electrons had been isolated, the hadrons were isolated from the remaining sample. Events satisfying any of the following tests were classified as hadrons:

I. Cerenkov amplitude < 90 in the units shown in Fig. IV-8.

II. Shower detector fluctuation ≤ 0.1 in the units shown in Fig. IV-5.

III. Shower detector fluctuation $> \frac{50E - 25}{12} > 5$, where E is the normalized shower detector amplitude in the units shown in Fig. IV-6.

IV. $0.1 < E_1, E_2 \leq 2.0$ where E_1, E_2 are the normalized shower detector amplitudes for the first and second planes in the units shown in Fig. IV-4.

In each of these four cases, a hadron with a normalized shower detector amplitude greater than 7.0 was rejected. No hadrons in the pure sample were observed to have a shower detector amplitude above this level.

These tests were administered in sequence, and once an event had passed one of the tests, it was not subjected to those remaining. At this point two important questions remain unanswered: i) How many electrons were misidentified as hadrons?, and ii) How many hadrons remained in the electron sample? Both of these questions had to be studied as a function of momentum in order that the hadron cross-sections could be corrected properly.

The total estimated number of electrons contaminating the hadron sample is shown below for each test:

I. Based on the coplanar electron sample, the probability

for a given electron to have a Cerenkov amplitude less than 90 had an upper limit of 1.32×10^{-3} with an 84% confidence level (corresponding to 1.8 events). No such electron was observed in a sample of 1400 events.

II. As deduced from the pure electron sample, the probability for an electron to have a mean squared counter fluctuation less than 0.1 was 9.17×10^{-4} for electrons with momenta above 1.2 GeV/c and 3.55×10^{-3} for electrons with lower momenta.

III. The probability for a given electron to exceed the level indicated by the line drawn through Fig. IV-6 had an upper limit of 1.33×10^{-3} with an 84% confidence level. No such events were observed among a sample of 1413 coplanar electrons.

IV. The probability for a given electron to have a normalized amplitude between 0.1 and 2.0 in each of the first two shower detector planes was 7.33×10^{-3} if the momentum was above 1.2 GeV/c and was 4.96×10^{-2} for electrons at lower momenta.

For each of these four criteria, the estimated electron contaminations were obtained by multiplying the appropriate probability for a given event to be misidentified as a hadron by the number of electrons remaining in the data after the coplanar ones were removed. This number was about two events for the 4.8 GeV data sample.

In a similar fashion the number of hadrons misidentified as electrons was calculated. The misidentification probabilities for a given hadron event are given below for each of the previously

described criteria:

I. As a result of Cerenkov counter contamination and the high amplitude characteristics of high momentum pions, no calculation could be made of the number of hadrons with a Cerenkov amplitude above 90, which would not involve a prior knowledge of the hadron momentum spectrum. After the hadrons were all identified, this subclass was examined and was found to have energy loss properties indistinguishable from those of the hadrons with a Cerenkov amplitude less than 90.

II. The probability that a hadron had a mean squared fluctuation greater than 0.1 was 40.8%.

III. The probability that a hadron was below the level indicated by the line drawn through Fig. IV-6 was 97.3%.

IV. The probability that a hadron had a normalized amplitude less than 0.1 or greater than 2.0 in either of the first two shower detector planes was 13.6%.

The tests II and III were mutually exclusive, so that a total of 61.9% of the hadrons passed one or the other. Since test IV was not fully independent of tests II and III, a more applicable probability was determined by studying those events of the pure hadron data sample that failed both of tests II and III. For such events 31.5% of the hadrons failed test IV. Consequently, the probability for a given hadron to fail all of tests II through IV was 12.0%. This number therefore represents the loss rate for hadron events with the Cerenkov counter amplitude above 90.

G. Separation of Pions, Kaons and Protons

1. General Description

Once the hadron sample had been identified and segregated from the electrons and muons, the next task was to subdivide them into pions, kaons and protons. At the higher momenta the Cerenkov counter tagged the pions; the kaons and protons were separated using the time-of-flight system. At momenta below 1.1 GeV/c the time-of-flight system was used exclusively to make the entire separation.

A plot of the time-of-flight (TOF) values for hadrons as a function of momentum is shown in Fig. IV-10. For each event the difference between its observed TOF value and the calculated value assuming its identity to be a pion, kaon or proton was determined. This procedure filtered out the momentum dependence in the TOF measurement and allowed an examination of the overall distribution of TOF measured values. Fig. IV-11 shows a histogram of Δt_{π}, the difference between the measured TOF for a given particle and the value expected if that particle were known to be a pion. This distribution was found to be Gaussian with a chi squared of 23.8 for 22 degrees of freedom. The width of this distribution as expressed by the standard deviation was σ = 0.59 ns.

2. The Identification Procedure

The best approach to hadron classification would have been to introduce cuts in the TOF distribution and to identify each event according to which side of the cut it was on. This procedure would have worked well at momenta below about 0.8 GeV/c where the TOF separation between pions and kaons was large. However, at higher

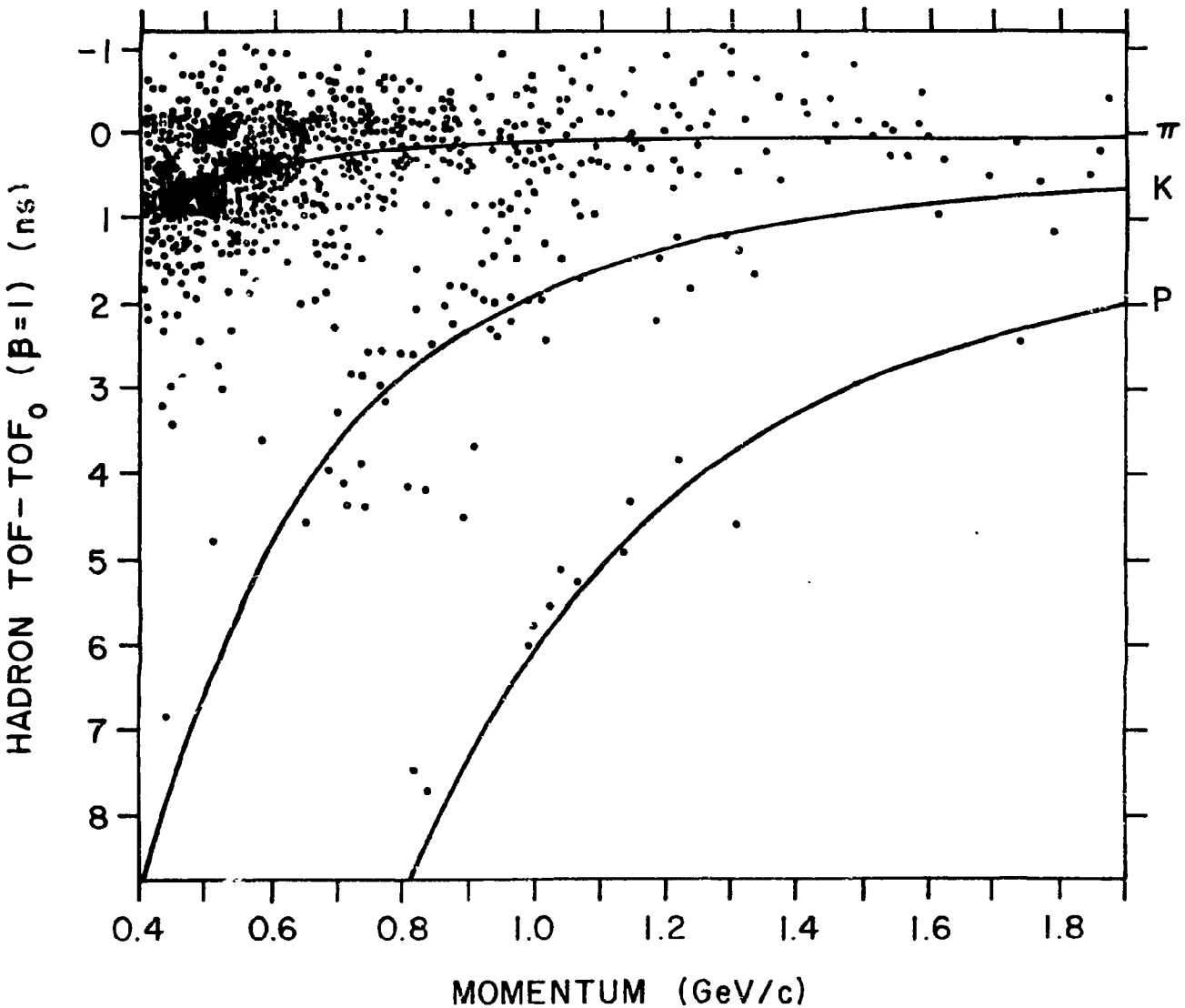

FIGURE IV-10. The normalized time of flight amplitude for hadrons.

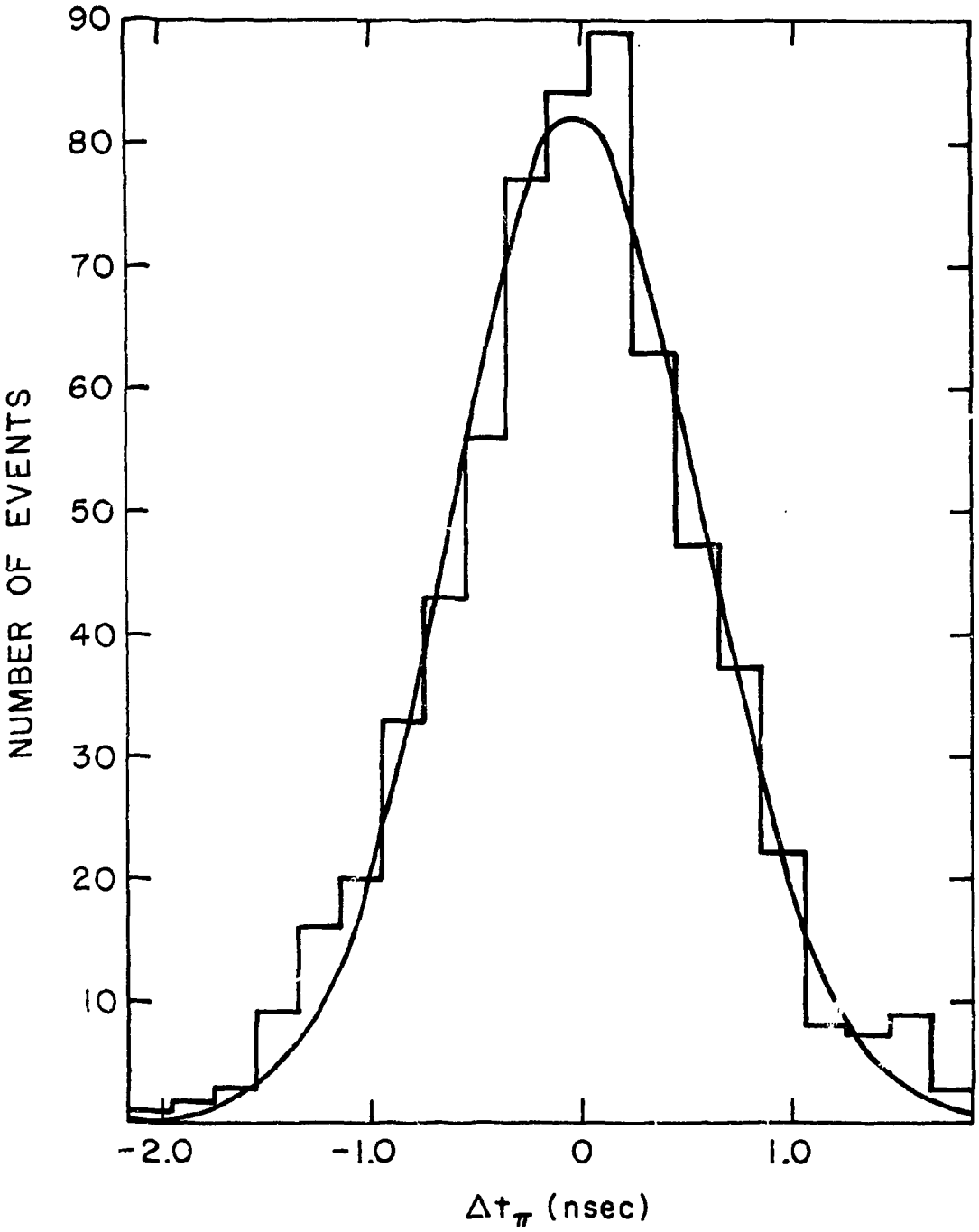

FIGURE IV-11. The distribution of time of flight values for pions with $0.4 < p < 0.6$ GeV/c. The abscissa is the difference between the observed time of flight and the value expected assuming the particle to be a pion. The solid line shows the best fit Gaussian distribution, having a chi square of 23.8 for 22 degrees of freedom. The distribution had a standard deviation of $\sigma = 0.59$ nsec.

momenta the two distributions merged. To attempt to position such a cut would be very risky, complicated by the relatively large number of pions which might spill over the cut and contaminate the small number of kaons in the data. To avoid this difficulty and to recover a maximum amount of the information contained in the low-statistics kaon sample, a more complex analysis procedure was used.

The differences between the observed time of flight t and the expected values assuming the particle to be a pion, kaon or proton can be denoted by

$$\Delta t_\pi = t - t_\pi \quad , \quad \Delta t_K = t - t_K \quad , \quad \Delta t_P = t - t_P \ .$$

The distribution of Δt_π values was Gaussian for pions and centered on zero. The Δt_K and Δt_P distributions were assumed to be Gaussian for kaons and protons respectively, each centered on zero, although the statistics were too low to test the validity of this assumption. The probability density function describing the distribution of TOF values for particles of type a, where a = π, K, or P is given by

$$f_a(t) = \frac{N_a}{\sqrt{2\pi}\cdot\sigma} \exp\{-\tfrac{1}{2}(\Delta t_a/\sigma)^2\} \quad .$$

Based on a sample of N_a particles of type a, this expression gives the number of particles per unit TOF measure having a TOF value t.

The probability that a particle having an observed time of flight t was of type a is expressible as

$$P(a) = \frac{f_a(t)}{f_a(t) + f_b(t) + f_c(t)} \quad ,$$

where (a,b,c) are any permutation of (π,K,P). In other words, the probability that an observed particle was, for example, a pion is equal to the pion fraction of the total parent population distribution evaluated in that TOF bin. In a sample of N events, the number of particles of type a can be taken to be

$$N_a = \sum_{i=1}^{N} P_i(a) \quad ,$$

where $P_i(a)$ is the probability that the spectrometer particle of event i has identity a. By substituting the expressions for the Gaussian density functions for $P_i(a)$, a set of three equations can be obtained relating the N_a:

$$N_a = \sum_{i=1}^{N} N_a g_i(\Delta t_a) \{ N_a g_i(\Delta t_a) + N_b g_i(\Delta t_b) + N_c g_i(\Delta t_c) \}^{-1} \quad ,$$

where

$$g(\Delta t_a) \equiv \exp\{-\tfrac{1}{2}(\Delta t_a/\sigma)^2\} \quad .$$

By assuming values for N_a, N_b, and N_c both sides of these expressions can be evaluated over the observed data. The fit values that satisfied these equalities were then taken as the observed numbers of each particle type. A derivation of the error propagation for this procedure is described in Appendix G.

To facilitate comparison with other experiments,[8,9] Fig. IV-12 shows as a function of momentum the square of the spectrometer particle mass as determined from the observed TOF value. The particle identification procedures described here were implemented by requiring that the TOF value be within two standard deviations of

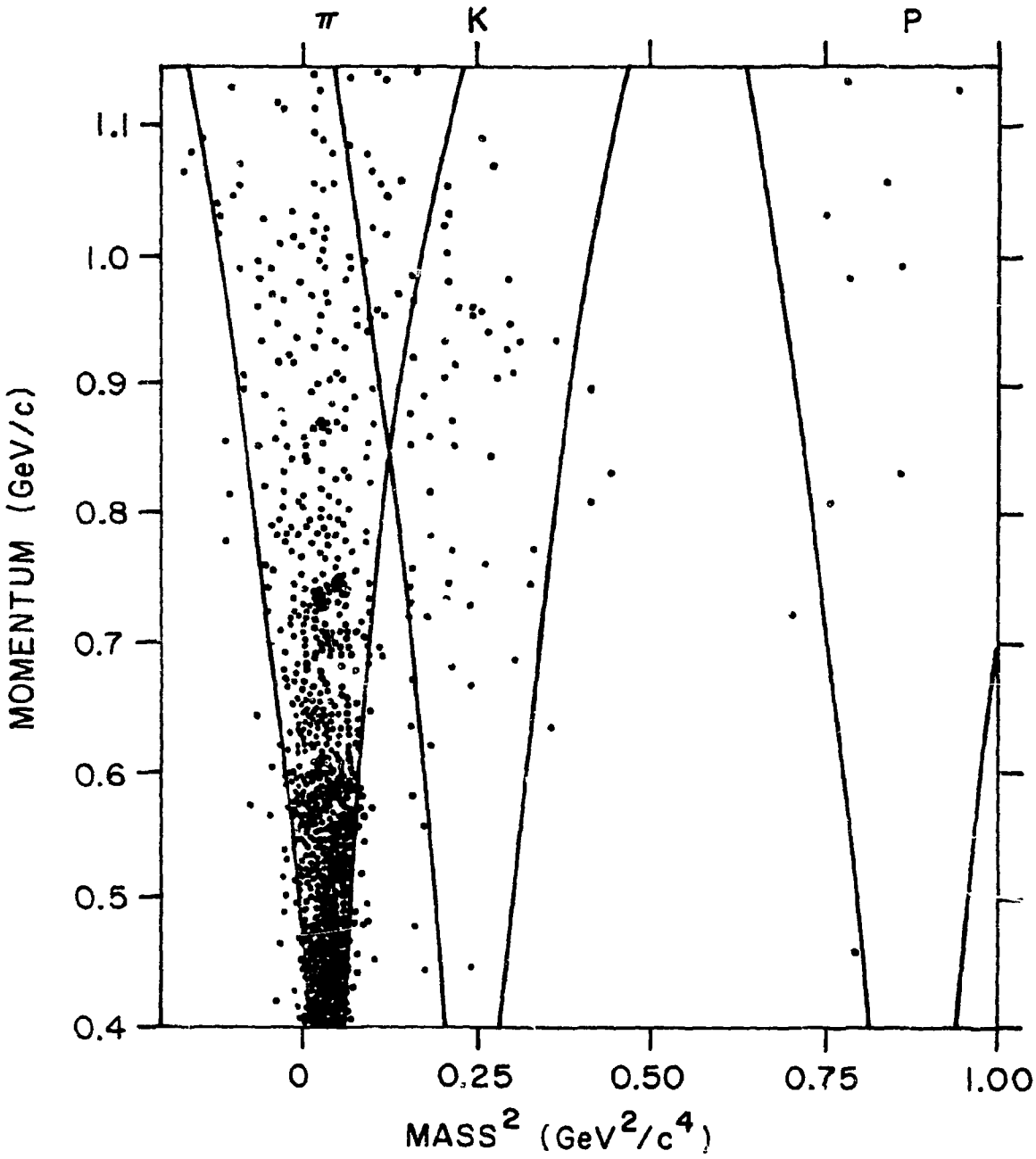

FIGURE IV-12. The distribution of the square of the spectrometer particle mass plotted as a function of its momentum. The mass is calculated based on the measured time of flight for the particle. The solid lines indicate the positions of the 2 standard deviation cuts imposed on the time of flight distributions.

at least one of the pion, kaon and proton expected TOF values. The principal reason for this and the chief difficulty associated with particle identification was the contamination resulting from K- decays. Extensive calculations were made to determine the amount of this contamination in order to correct the particle count. This calculation is described in detail in Section VI-B.

REFERENCES

CHAPTER IV

1. B. Rossi, "High-Energy Particles," Prentice-Hall, Inc, (1952), pp. 29-35.
2. D. M. Ritson, "Techniques of High Energy Physics," Interscience Publishers, Inc. (1961), Chapter I.
3. C. Jordan and Heinz-Georg Sander, Diplomarbeit, Aachen University, 1974 (unpublished).
4. K. Abe, et. al., Phys. Rev. D 10, 3556 (1974).
5. A. Buhler, T. Massam, Th. Muller and A. Zichichi, Nuovo Cimento 35, 759 (1965).
6. A. T. Laasanen, Ph.D. thesis, University of Maryland Technical Report No. 73-055 (1973) (unpublished).
7. P. M. Joseph, Nucl. Instr. and Meth. 75, 13 (1969).
8. C. C. Morehouse, Proceedings of Summer Institute on Particle Physics, SLAC Report No. 191, P. 247, (1975).
9. B. Wiik, Proceedings of the 1975 International Symposium on Lepton and Photon Interactions at High Energies, Stanford, Calif. (1975).

CHAPTER V

COLLINEAR MUON PAIRS AND QED COMPARISONS

A. Selection of μμ Events

The identification of muons was described in Section IV-F. All the events discussed in the present chapter were required to penetrate all three hadron filter planes on both sides of the apparatus and to be collinear within 3^{o}. An origin cut required that the spectrometer particle trajectory extrapolate into the $e^{+}e^{-}$ interaction region. (This same cut was also applied to all the other events.)

Such a cut eliminates most of the cosmic ray contaminations. Cosmic rays were automatically suppressed by the horizontal layout of the spectrometer. Many cosmic ray muons which would have traversed the spectrometer in the "forward" direction were filtered out by a large dirt hill outside the storage ring, overshadowing the east interaction pit. A convenient feature of the TOF system and the Cerenkov counter was that they provided a redundant tag for identifying cosmic rays entering the spectrometer from the side unprotected by the hill. This muon contamination included high energy muons produced by the LINAC. A further cut on cosmic ray muons was the requirement that any event satisfying the trigger had to occur within a narrow time window specified by the $e^{+}e^{-}$ collision timing. An examination of the data indicated that the probability for a given μμ event in the momentum interval $1.0 < p < 2.6$ GeV/c to be a cosmic ray was less than 0.1%.

The momentum distribution for collinear μμ events is shown in Fig. V-1 for data taken at a total center of mass energy of

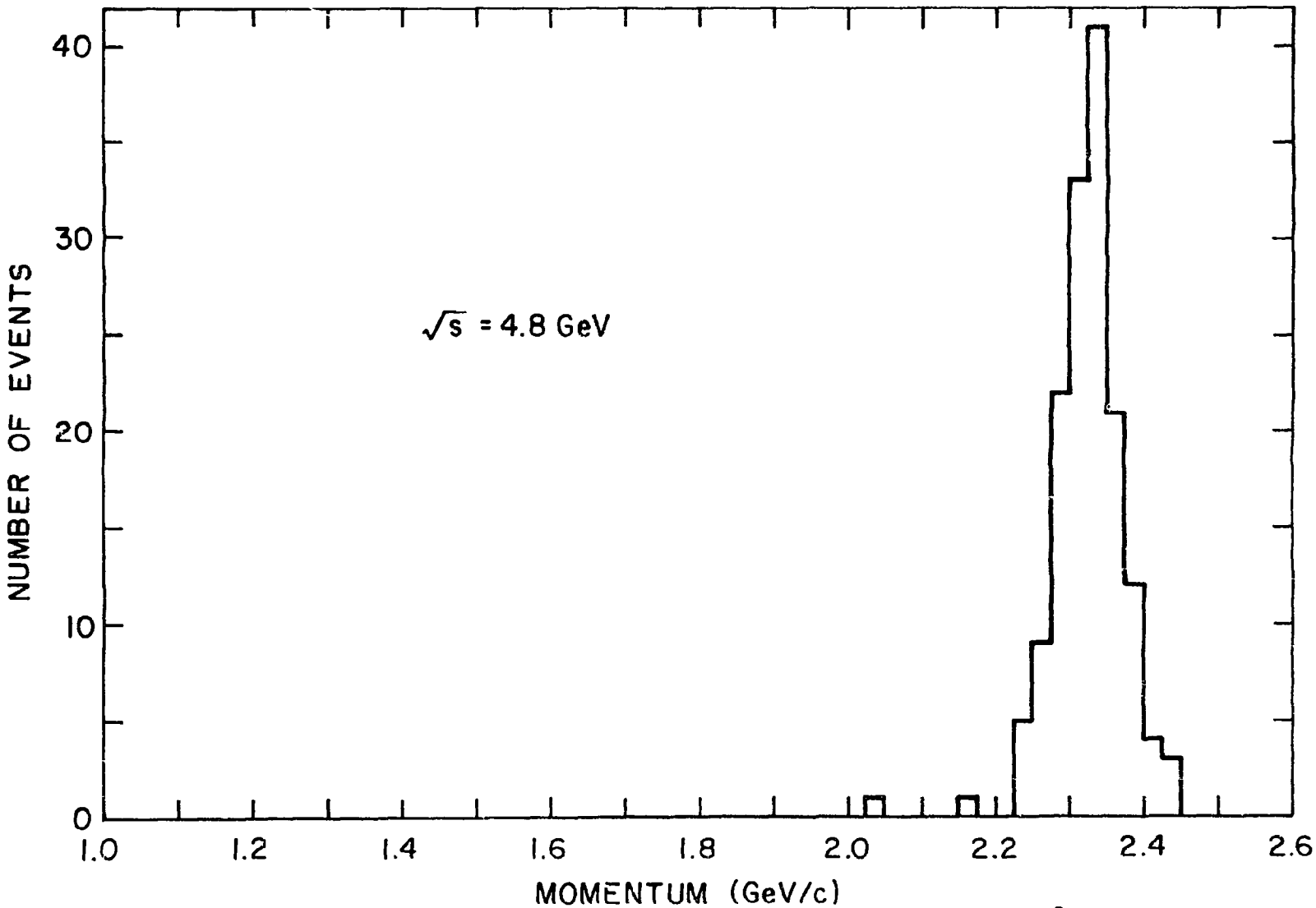

FIGURE V-1. Momentum distribution of μμ events collinear within 3^{o}.

W = 4.8 GeV.

B. QED Calculations

The predominant mechanism for producing muon pairs is

$$e^+e^- \rightarrow \mu^+\mu^-$$

in accordance with QED. A QED calculation for this process accurate to a few percent should include virtual radiative corrections to order α^3 together with reactions of the type

$$e^+e^- \rightarrow \mu^+\mu^-\gamma$$

where a photon is emitted, since such a photon would usually go undetected in the experimental apparatus[1]. Even if it were detected in one of the shower counters, its origin could not have been reconstructed, so no attempt was made to distinguish such events.

A calculation of the cross section for these reactions together with phase space effects was performed in Ref. 1. A numerical integration computer program was written by the authors for evaluating the cross section for a specific experimental arrangement[2]. A version of this program was installed in the University of Maryland computer and debugged by Dr. K. J. F. Gaemers. The program was used to calculate the differential cross section for producing a muon at some angle within the spectrometer acceptance and another muon anywhere within the solid angle subtended by the conjugate side hadron filter. An energy threshold of 1.05 GeV was imposed upon both muons, corresponding to the requirement that they penetrate all three planes of the hadron filters. The program also allowed the imposition of a cut on the μμ acollinearity, facilitating a comparison with the

observed acollinearity distribution for the muon pairs. This distribution is shown in Fig. V-2. The numerical calculation of the cross section was normalized to the number of observed muon pairs with acollinearity less than 3^{o}. The distribution at angles greater than 3^{o} agreed with the QED calculation results shown by the solid line in Fig. V-2. The chi square was 7.7 for 9 degrees of freedom, giving a confidence level of .55. The plot of the distribution ends at an angle of 30^{o} because detection of events with greater acollinearity was less than 100% efficient. The largest acollinearity value that could have been measured was about 60^{o}, and the limiting factors were the size of the conjugate side hadron filter and the spectrometer angular acceptance.

C. Cross Section Normalization

Since the production of collinear muon pairs is accurately described by QED[2], the known cross section could be compared with the observed number of collinear muon pairs in order to establish the time-integrated beam luminosity. This number can then be used to normalize the cross-section for any inclusive particle production observed in the spectrometer.

If the number of collinear muon pairs observed was N and the mean solid angle acceptance of the spectrometer for these events was $\Delta\Omega$, then the integrated luminosity L was

$$L^{-1} = \frac{2}{N}\frac{d\sigma}{d\Omega}\Delta\Omega \quad .$$

The differential cross-section for collinear muons indicated here was

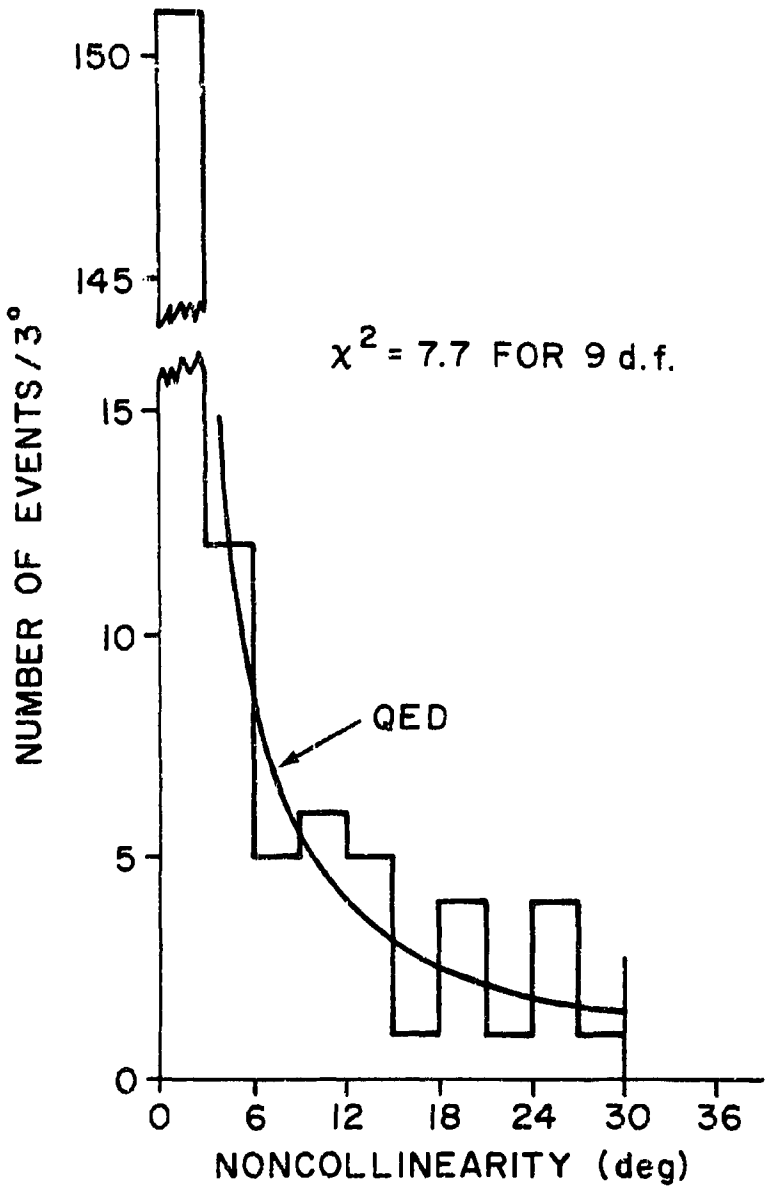

FIGURE V-2. Noncollinearity distribution out to 30° for $e^+e^- \to \mu^+\mu^-\gamma$ at $\sqrt{s}$ = 4.8 GeV (angular resolution ±0.3°). Both muons required to penetrate 69 cm Fe. QED curve from Ref. 1 (χ^2 = 7.7 for 9 degrees of freedom).

averaged over the angular acceptance of the spectrometer. The factor of 2 is present because the single-particle trigger can be satisfied by either muon in each event. The integrated luminosity values obtained for the data samples taken at various total center of mass energies were:

$L = 0.98 \pm 0.12\ pb^{-1}$ at $W = 3.8$ GeV,

$L = 3.73 \pm 0.30\ pb^{-1}$ at $W = 4.8$ GeV,

$L = 0.87 \pm 0.15\ pb^{-1}$ at $W = 5.0$ GeV.

The output of a luminosity monitor located in the west interaction pit was recorded throughout the experiment. (See Section II-B.) Its results were in good agreement with those shown above.

REFERENCES

CHAPTER V

1. F. A. Berends, K. J. F. Gaemers, and R. Gastman, Nucl. Phys. B57, 381 (1973).

2. For comparisons of the QED calculation programs with experiment, see B. L. Beron, et. al., Phys. Rev. Lett. 33, 663 (1974); J. E. Augustin, et. al., Phys. Rev. Lett. 34, 233 (1975); and J. E. Zipse, Ph.D. thesis, Lawrence Berkeley Laboratory Report No. LBL 4281, 1975 (unpublished).

CHAPTER VI

INCLUSIVE HADRON PRODUCTION

A. Introduction

A description of how events were selected was given in Chapter III, and a description of how the spectrometer particle in each event was identified was given in Chapter IV. Once the hadron events had been classified according to whether they were pions, kaons or protons and the associated charged multiplicity had been determined, the various inclusive production cross sections could be calculated.

It was by no means sufficient to simply count the hadrons and then determine the cross section via the muon normalization of Chapter V: a number of corrections had to be made to the observed numbers of hadrons. The various corrections are described in Sections B through E. The calculations of the pion, kaon and proton inclusive cross sections are given in Section F along with the produced particle fractions as a function of momentum. Also given in Section F is the invariant differential cross section summed over all hadron types. Section G contains a discussion on the determination of the charged multiplicity as a function of the spectrometer particle momentum, including the corrections to the observed numbers of tracks.

The results presented in this chapter are primarily an extension of previously published[1] results to lower values of the hadron momentum. The use of a more advanced version of the event reconstruction program (Chapter III) also facilitated the expansion of the allowed values of the spectrometer angular acceptances out to the physical limits imposed by the apparatus. This led to a small

increase in the size of the high-momentum data sample previously published. Improvements were also made in the shower detector analysis, resulting in more efficient electron identification procedures.

B. Corrections for Decays in Flight

1. General

Decays of pions and kaons as they traversed the spectrometer had several effects on the observed numbers of each type of particle. The decays dealt with in the present section are

$$\pi^{\pm} \rightarrow \mu^{\pm} + \nu$$

$$K^{\pm} \rightarrow \mu^{\pm} + \nu$$

$$K^{\pm} \rightarrow \pi^{\pm}\pi^{o}$$
$$\qquad\quad \lfloor \rightarrow 2\gamma \ .$$

The other decays of the kaon were ignored because their effects were sufficiently small to have no significant influence on the experimental results. Their total effect was included in the overall decay loss correction.

Since it was the goal of this experiment to measure the numbers of particles of each identity produced in the e^+e^- interactions, any mechanism which could deplete the sample of spectrometer particles had to be compensated. One such effect resulted from the requirement that the time-of-flight of an observed particle must have been within two standard deviations of the TOF distribution from at least one of the values expected for a pion, kaon or proton having the measured momentum. A decay in flight could change the TOF value by more than this two-standard-deviation cut, thus causing the event

to be dropped from the analyzed sample. Also, the transverse momentum introduced by the decay might have changed the measured momentum value, so that the TOF cut was evaluated at a momentum different from that of the incident hadron.

Even when the TOF value for the decayed event was within the cuts, if the charged secondary particle was a high momentum muon, it would have penetrated the hadron filter causing the event to be tagged as a muon. This did not apply to kaons which decayed after passing through the Cerenkov counter, since they would not have had a Cerenkov signal.

2. Corrections for TOF and Momentum Measurement Errors

The number of events decaying in the spectrometer was calculated as a function of momentum. If the probability for a hadron to traverse the spectrometer without decaying is denoted by S, and if the assumption is made that a decayed particle was lost from the sample, then the number of particles N originally produced in the e^+e^- interaction was

$$N = N_o/S \ ,$$

where N_o was the number observed. The survival probability S is shown as a function of momentum for charged pions and kaons in Fig. VI-1.

However, it is certain that some of the decayed hadron events fell within the TOF cuts, and their presence had to be compensated for. If the probability for an event to decay and still fall within the TOF cuts is designated D, then a more accurate correction formula is

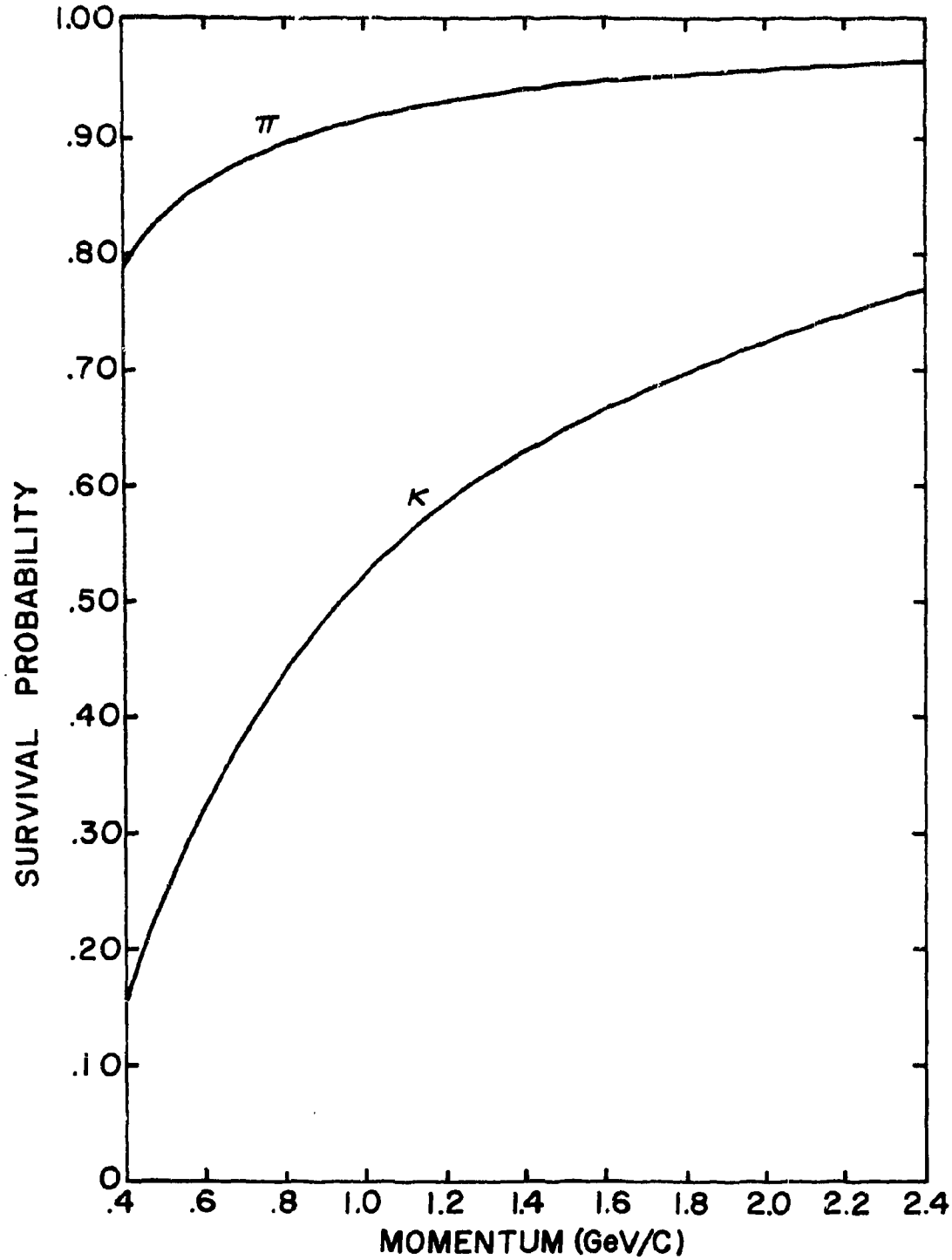

FIGURE VI-1. The probability that a pion or kaon will traverse the spectrometer without undergoing a decay, as a function of momentum.

$$N = N_o/(S + D) \ .$$

It should be noted that each quantity in this expression is momentum dependent.

In order to determine the detection efficiency D for decayed events, a kinematical analysis was performed. The effects of decays on the momentum reconstruction were determined using the simplifying assumption of a uniform, single-component magnetic field inside the spectrometer. The change in measured deflection was calculated as a function of the center of mass decay angle and the position in the spectrometer at which the decay occurred. Averages were performed over both of these variables at various values of the incident hadron momentum. The effects of the decay on the measured time of flight were also included. The probability D is shown as a function of the measured momentum value in Fig. VI-2 for each of the decays considered.

3. Correction for Secondary Muon Penetration

Even though a decayed hadron event fell within the TOF cuts, if the charged secondary was a muon with sufficient momentum to penetrate the hadron filter the event would still have been deleted from the hadron sample. The probability P for a secondary muon to penetrate the hadron filter is shown in Fig. VI-3, plotted as a function of the incident pion or kaon momentum. The penetration probability was calculated by considering the angles of emission of the muons in the pion center of mass reference frame such that the lab momentum of the muon was greater than 1.05 GeV/c. The penetration probability was equated to the fraction of the total solid angle in the CM

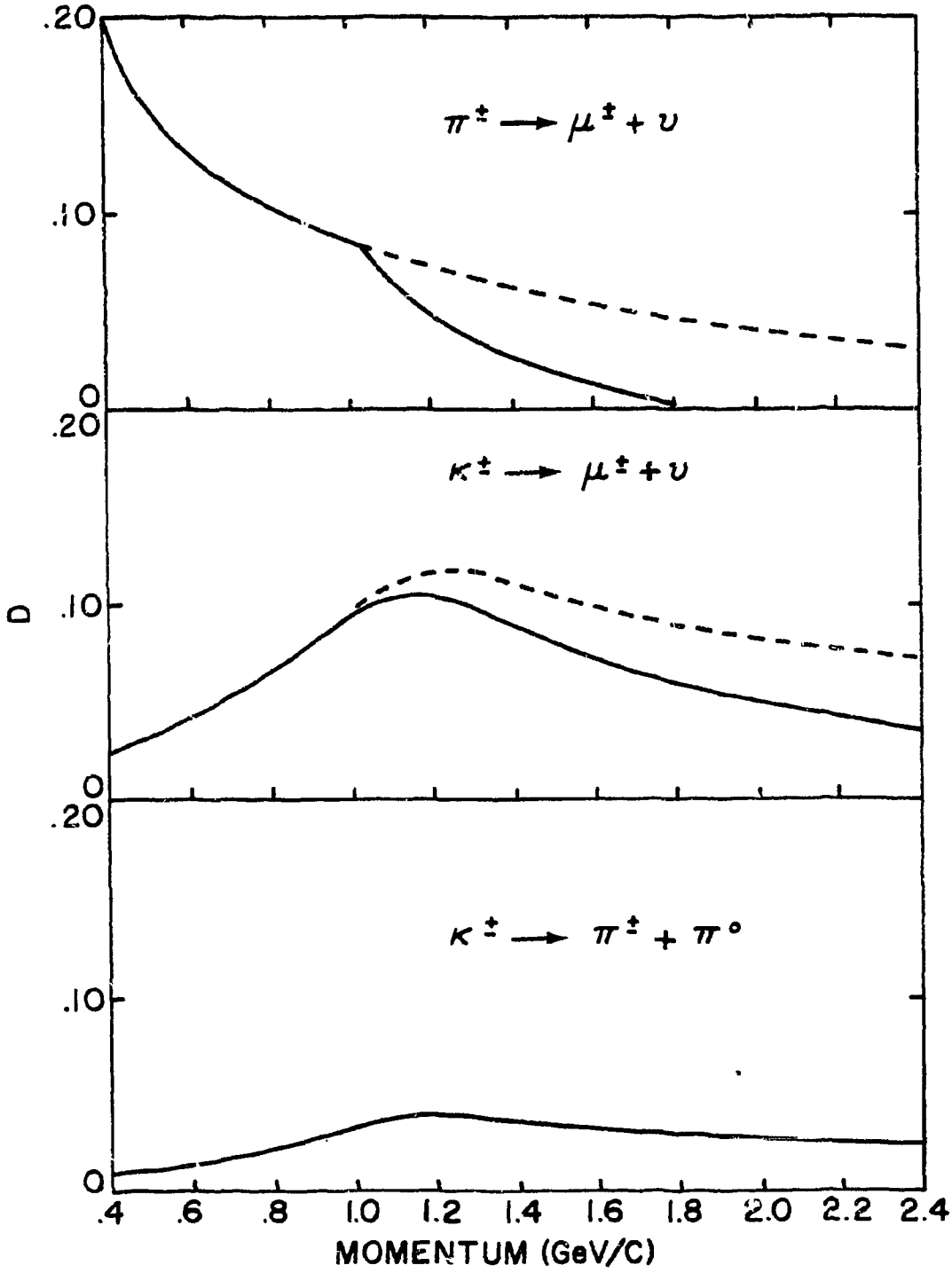

FIGURE VI-2. The probability D that a particle will experience a specific type of decay in the spectrometer and still fall inside the time-of-flight cuts. This detection probability is shown as a function of momentum for the three principal decay modes considered. The dashed curves represent the detection probability distributions if hadron filter penetration were not used to tag the secondary muons.

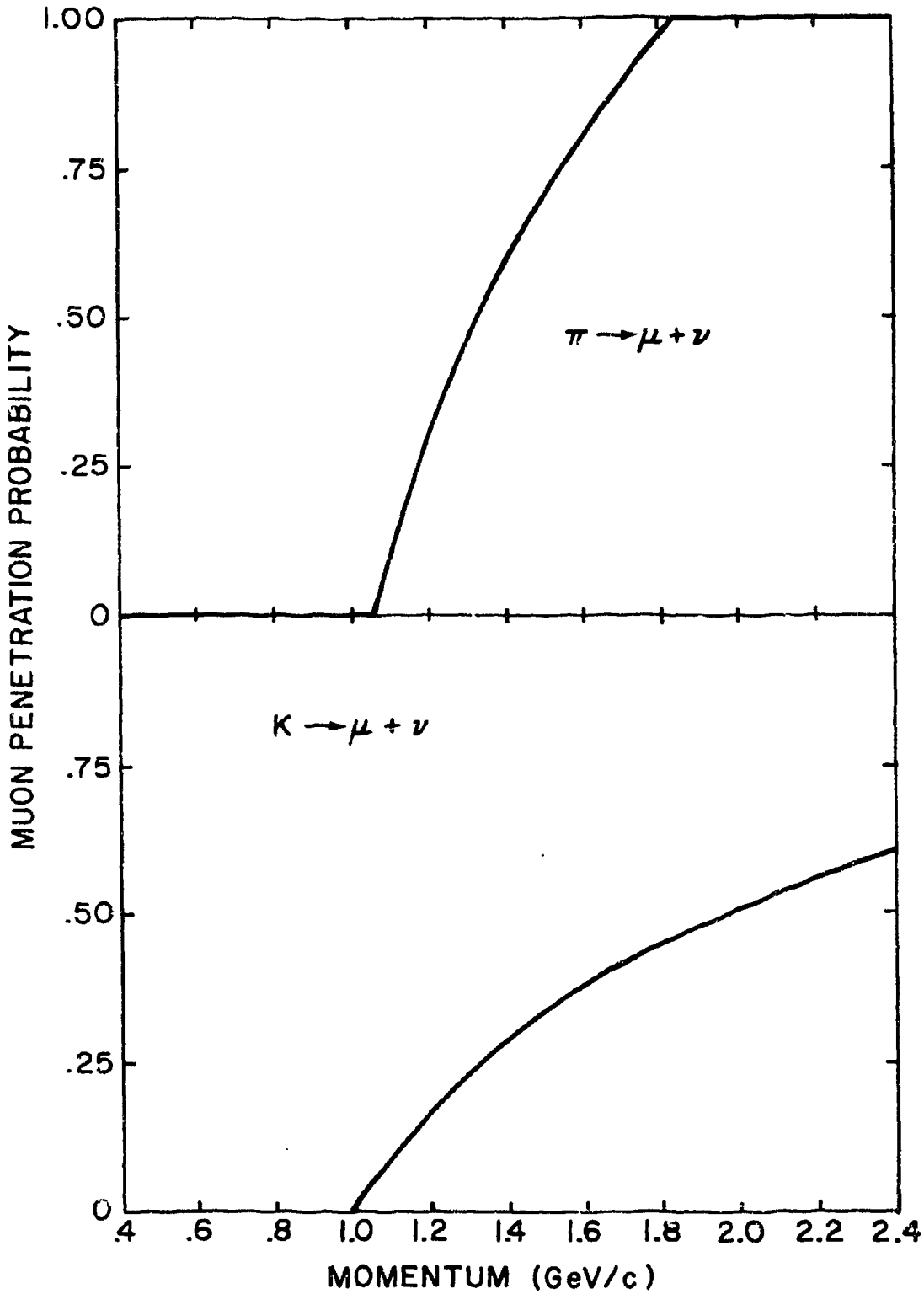

FIGURE VI-3. The probability that the secondary muon produced in pion and kaon decays will penetrate the hadron filter, as a function of the momentum of the incident hadron.

system over which this kinematical constraint was satisfied.

This effect did not occur with equal probability for those decayed hadrons outside the TOF cuts and those inside. The high-momentum muon secondaries would tend to be associated with events falling within the TOF cuts. Consequently, the correction for muon penetration was folded into the calculation of the decay detection efficiency D, rather than being applied separately. For the kaon decays, only those events decaying to a muon before or within the Cerenkov counter were taken into account. The remaining events could be tagged by the low Cerenkov counter amplitude.

4. Corrections for TOF Contamination

There were some events with time-of-flight values which were clearly unphysical. As explained in Section II-H, whenever two or more scintillation counters in the same plane of the shower detector were hit, the TOF amplitude for that plane was indecipherable. Thus, these events could not be included in the TOF analysis.

In order to make the observed numbers of hadrons consistent with the muon normalization of the cross sections, the unanalyzable events had to be factored back into the observed number N_o. The simplest procedure was to assume that the unanalyzed events were distributed according to identity in the same manner as those which were analyzed. However, such a procedure would not take into account the problem that a charged K which decayed into two pions could selectively contaminate the TOF system. The charged pion could traverse one of the TOF counters in the shower detector, tripping the TOF system. At the same time a gamma produced by the decay of

the neutral pion could convert and trip another counter, resulting in the contaminated signal.

From this source one would expect the sample of events having unanalyzable TOF values to contain a higher fraction of kaons than the analyzed sample: These unanalyzed events could never be subjected to the TOF cuts which filtered out most of the decays during the TOF analysis.

The TOF contamination effects due to these kaon decays were estimated using a modification of the kinematical calculations performed to determine the detection efficiency for hadrons decaying to muons. The relative fraction of contaminating decays to total observed kaon events was determined as a function of momentum. The number of such events expected from kaon decays into two pions is shown in Fig. VI-4.

If the observed number of analyzable hadron events of type i was N_{oi}, where $i = \pi, K, P$; the total number of TOF-contaminated events was M; and the estimated number of contaminated events resulting from kaon decays into two pions was M_k; then the M events should have been divided according to

$$N_{oi} \rightarrow N_{oi} + (M - M_k)N_{oi} / N_o \quad ,$$

where N_o is the total number of hadron events with uncontaminated TOF. In addition to this correction term, the quantity M_k was added as a correction to the number of observed kaons.

C. Corrections for Hadron Punchthrough

If a hadron had sufficient range to penetrate the hadron filter, there was a small probability that it would do so and be tagged as a

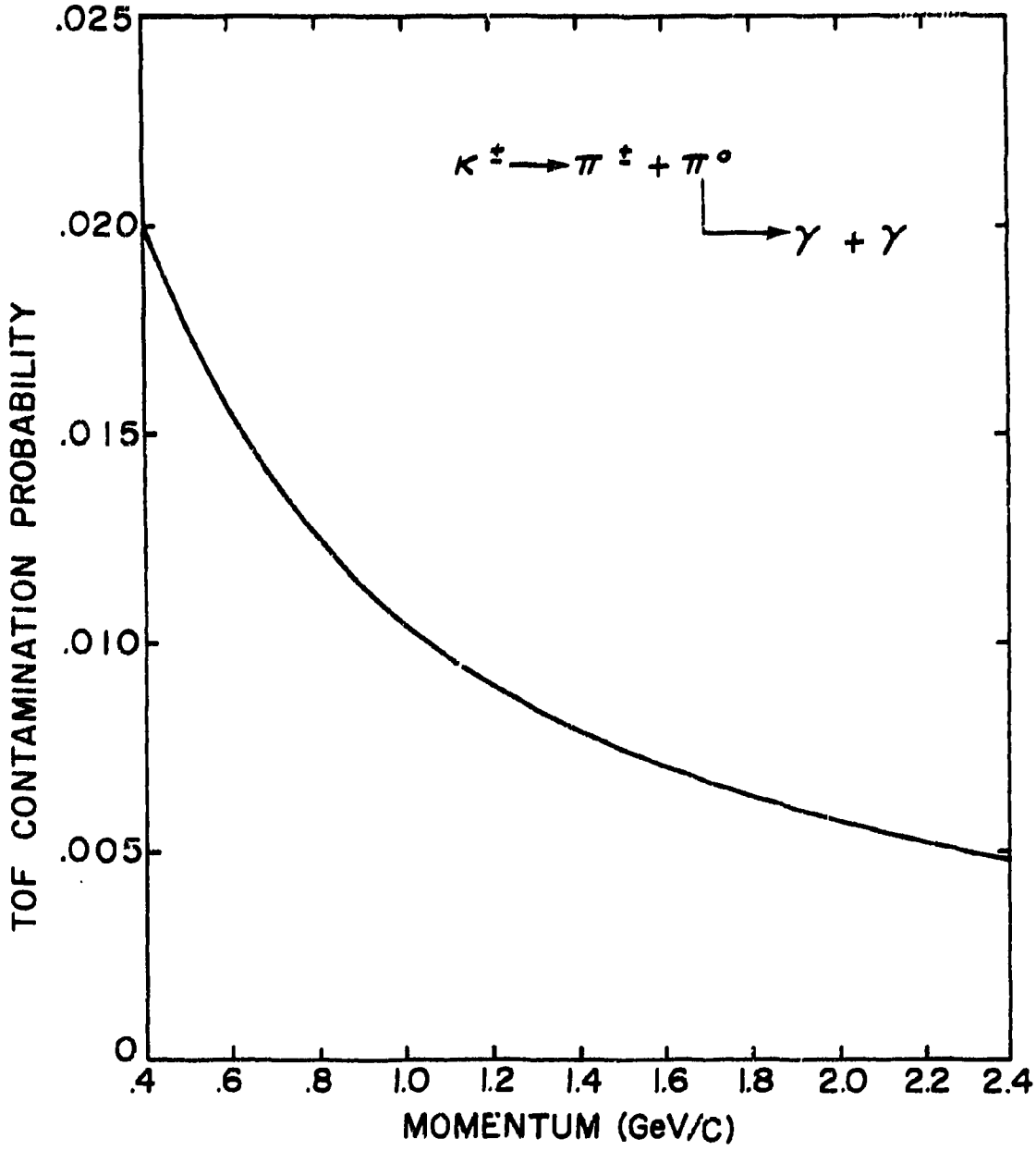

FIGURE VI-4. The probability that a charged kaon will decay into two pions in the spectrometer and that the decay products will contaminate the time-of-flight system. The nature of this type of contamination is discussed in Section II-H.

muon. The evaluation of this probability for a given event was described in Section IV-D. By evaluating this probability over all observed hadrons, the average punchthrough probability was determined as a function of momentum.

A plot of the punchthrough probability distribution is shown in Fig. VI-5. The punchthrough probabilities were determined using the procedures described in Section IV-D. The effects included were the nuclear attenuation, range limitations, the hadron angles of incidence on the hadron filter, and the effects of range straggling. The assumption was made that for pions and kaons, nuclear attenuation was identical. An indication of the magnitude of the error introduced by this assumption can be had from Fig VI-6. In view of the low kaon statistics and the smallness of the punchthrough correction, the error resulting from this assumption was not significant. The range limitations on the kaons resulted in nonzero punchthrough probabilities only for those few events above 1.4 GeV/c.

Because kaons and protons could be tagged by the Cerenkov counter at all momenta where there was any significant punchthrough probability, they could be explicitly accounted for. Unfortunately, however, such kaon events were not distinct from kaons which decayed to muons after traversing the Cerenkov counter, and so they could not be separately tabulated. Hence, the punchthrough correction was performed for both kaons and pions.

If the punchthrough probability was P and the number of observed events was N_o, the corrected number was

$$N = N_o / (1 - P) .$$

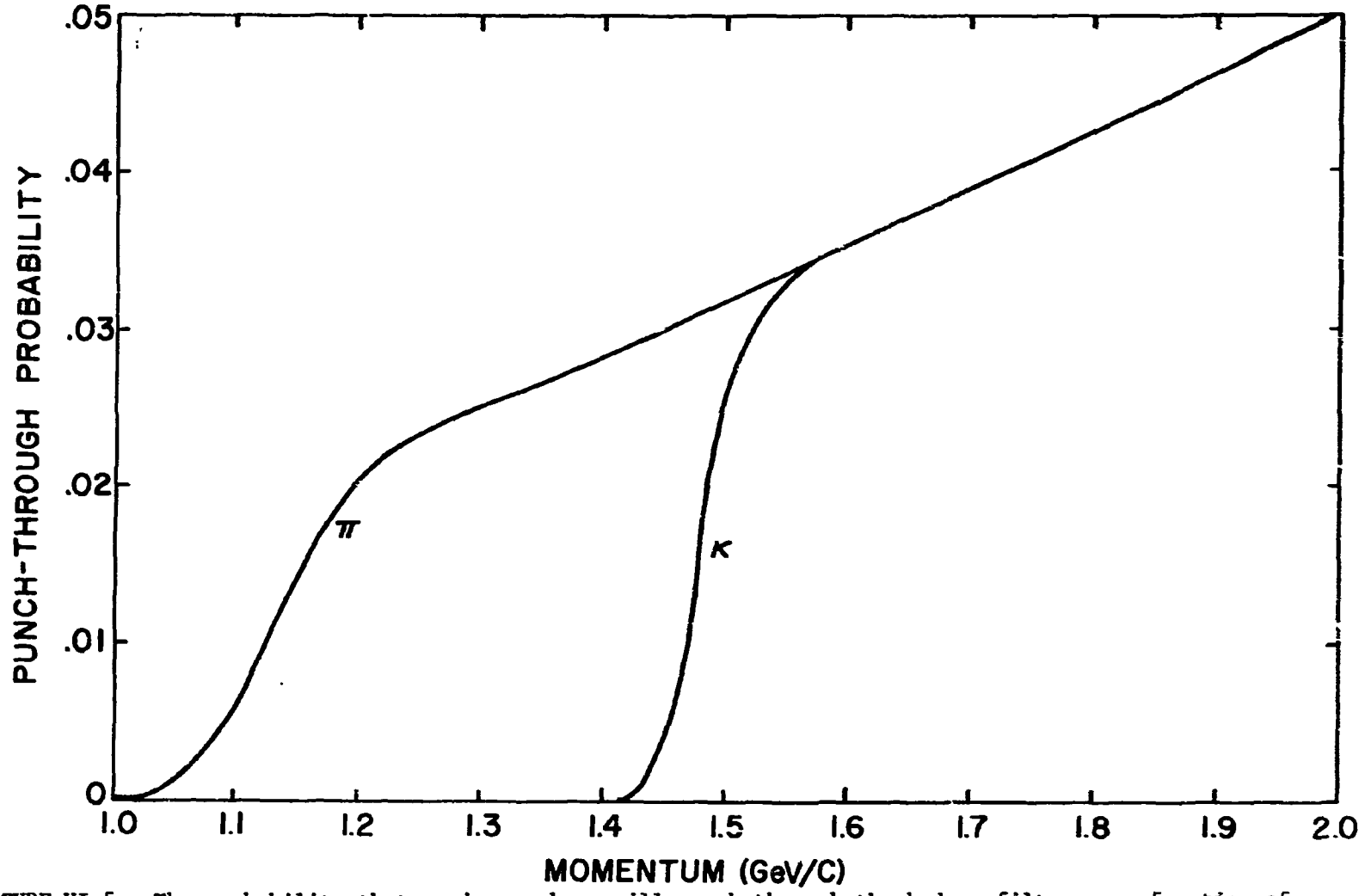

FIGURE VI-5. The probability that a pion or kaon will punch through the hadron filter as a function of momentum. The assumption was made that the nuclear attenuation was the same for both types of particles. The effects of nuclear attenuation, range, range straggling and angle of incidence were included in the calculation.

D. Corrections for Nuclear Interactions

Another factor which had to be taken into account in computing the hadron production cross sections was the loss of events which occurred whenever a hadron interacted with nuclei in the apparatus near the beam. This correction was momentum dependent and also depended on the identity of the hadron.

In the absence of accurate measurements of the absorption cross sections for hadrons on nuclei in the momentum interval 0.4 GeV/c $<$ p $<$ 2.0 GeV/c, a series of approximations was made in order to obtain the necessary cross sections describing hadron depletion. Extensive data was available in this momentum range for the total cross sections of pions and kaons on deuterium.[2-4] Because of the small number of protons observed in the spectrometer, the same correction was applied to them as to pions. Averages over momentum were made of the hadron-deuterium total and elastic cross sections for overall comparison purposes. An average absorption cross section was calculated by subtracting the average elastic cross section from the average total cross section. The averaging procedure was used to smooth out the effects of having only a few measurements, with little comparison available at common momentum values.

From the data of Reference 5, the ratio was calculated for pions on aluminum versus pions on deuterium. It was 9.3±0.6. The principal assumption in this procedure was that the same scale factor could be used for kaons. The momentum dependence was factored back into the average absorption cross sections for aluminum by requiring them to have the same percentage variation at a given momentum value as the total cross sections for deuterium. The resulting approximations

for the absorption cross sections for pions and kaons on aluminum are shown in Fig. VI-6 as a function of momentum. Other materials, such as the steel of the vacuum pipe and the propane in the Cerenkov counter were converted into aluminum equivalents for the attenuation calculation.

The uncertainties in the magnitudes of the absorption cross sections were due to two principal factors. A 7% uncertainty arose from the imprecision of the measurements upon which the calculations were based. The additional uncertainty arising from the assumption that the same scale factor could be used for kaons as for pions in going from deuterium to aluminum was more difficult to assess, due to the lack of data. However, this would appear to be a reasonable assumption, since the neutron-proton ratios differ by only about 6% for deuterium and aluminum. Using an 8% estimate for the total uncertainty in the absorption cross sections results in an uncertainty of 0.7% in the uncertainty propagated to the final hadron production cross sections.

The effects of diffraction scattering from nuclei composing the apparatus near the beam were found to be negligible. The ratios of the elastic to the absorption cross sections were about 30% for pions and 10% for kaons. In addition to the relatively small number of events undergoing these scatters, the majority of them would scatter no more than several degrees and would be adequately reconstructed without depletion of the sample. Many of those events lost because they scattered at angles more than about 6^{o} would have been compensated by others which scattered from outside the solid angle acceptance of the spectrometer such that they came within its acceptance. The

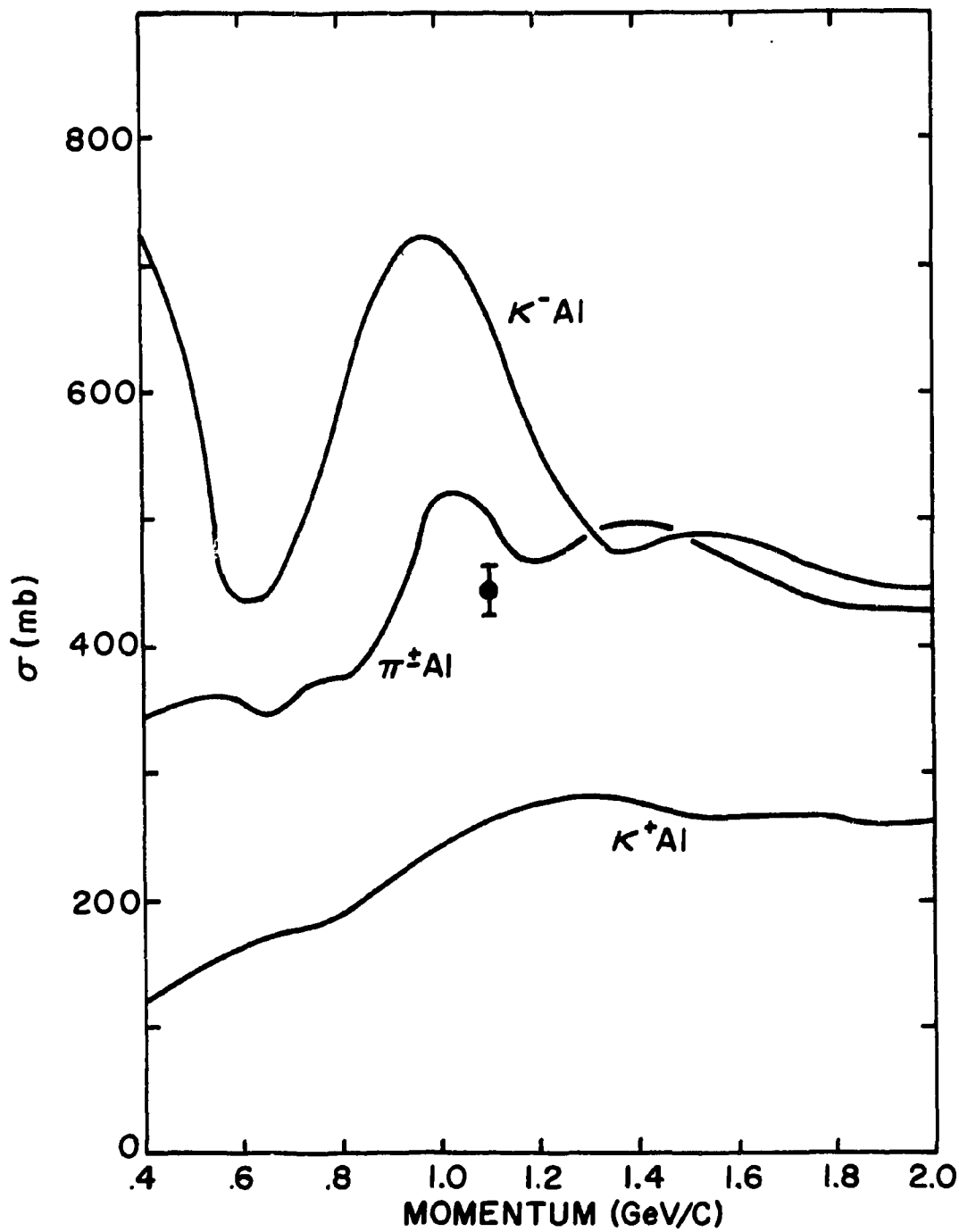

FIGURE VI-6. The approximate absorption cross sections for pions and kaons incident on aluminum as a function of momentum. The values were used to correct for hadron absorption by the nuclei in the materials making up portions of the spectrometer. The single measurement for π^- on Al is included from Ref. 5 for comparison.

estimated depletion of events resulting from nuclear diffraction scattering was considerably less than 1%. The number of secondaries produced by the nuclear absorption process[6] and falling within the spectrometer angular and momentum acceptance was likewise found to be negligible.

E. Miscellaneous Corrections and Background Subtractions

1. Various Corrections to the Observed Numbers of Hadrons

Sections B, C, and D described the nature of most of the principal corrections which had to be applied to the observed numbers of hadrons in order to obtain the numbers of pions, kaons and protons in each momentum bin, produced by the electron-positron interactions. The actual implementation of these corrections is described in detail in Appendix H.

The corrections described in Sections B - D account for decays in flight, the penetration of the hadron filter by hadrons and secondary muons, and the interactions of hadrons with the nuclei in the materials making up the apparatus. Two other significant corrections were the subtraction of hadronic backgrounds from beam-gas and beam-pipe interactions and the compensation for the presence of accidental signals in the Cerenkov counter, which could have caused a hadron to be classified as an electron and which resulted in kaons being misidentified as pions.

The nature of the hadronic background was assessed from runs with only a single beam present or with both beams separated so that there were no electron-positron collisions. Much of the background had been removed by event selection criteria in the analysis program, described in Chapter III. The estimated number of background events

remaining in the data sample was determined from an examination of the events originating along the beam line but outside the origin cut. The origin acceptance applied to particles in the spectrometer was an elliptic region centered on the observed origin distribution and extending out to ±29 cm along the beam at $\sqrt{s}$ = 4.8 GeV and out to ±22 cm at 3.8 GeV. The vertical aperture extended out to ±5 mm at both center of mass energies. The subtracted background consisted of a total of 62 pions, having momenta between 0.4 and 0.8 GeV/c, out of an observed sample of 667 pions in this momentum range. Proton backgrounds were dispensed with by counting only antiprotons and doubling the observed numbers.

The probability that the Cerenkov counter would accidentally fire was found to be 10.0±0.8% from a study of a large sample of low-momentum hadrons. This contamination probability showed no significant variation as a function of hadron momentum or charged multiplicity. Some possible causes of accidentals in the Cerenkov counter are discussed in Section IV-E. The amplitude threshold used to separate kaons from pions at high momentum was 18 on the scale shown in Figs. IV-8,9. Setting the threshold higher would have reduced the accidentals rate substantially, but at the expense of clean kaon-pion separation near the pion threshold. This correction was folded into the cross section calculation along with the others, as detailed in Appendix H.

2. Systematic Errors in the Identification of Low-Momentum Kaons

One major problem associated with the identification of low-momentum kaons remains to be discussed. The identification of both kaons and pions at low momentum was accomplished using the time-of-

flight system. The various corrections resulting from their principal decay modes were described earlier in the present chapter. However, one additional characteristic which distinguished kaons from pions in the apparatus was their energy loss in the shower detector. In particular, some of the kaons with momenta near 0.4 GeV/c could be expected to stop inside the shower detector, and the other low-momentum kaons would range out only a short distance into the hadron filter. Thus, all these kaons underwent decays only a short distance from the TOF counters and the C5X proportional wire chamber. Contamination of the TOF system and saturation of the C5X position-recording capacity (5 wire addresses in each of 3 reader cards, each card covering 1/3 of the chamber) could result if the decay secondaries had sufficient range to penetrate backwards into the TOF counters or C5X. In fact, a number of events were observed having these characteristics. The nature of the TOF contamination is discussed in detail in Section II-H.

The momentum available to a secondary muon produced by a kaon decaying at rest is 236 MeV/c. The range of this muon in the lead and iron of the shower detector and hadron filter corresponds to the range of a kaon having a momentum of about 600 MeV/c. The situation is complicated by the fact that the decays could have occurred at any point before the kaon came to rest, extending the significant effects due to this process to some of the kaons having momenta somewhat higher than 600 MeV/c. Because of the much smaller amount of energy released in pion decays, their longer lifetimes, and their considerably greater range at a given momentum, they did not exhibit this type of contamination. Calculations indicated that more than half of the

kaons with moments near 0.4 GeV/c could suffer contamination resulting from decays in the shower detector.

In an attempt to recover these events a study was made of the low-momentum energy loss distributions in the shower counters and in the S1 counter near the beam. Using this information, it was possible to recover many of the kaon events whose TOF values were distorted due to the decays in the shower detector. However, there remained numerous events which could not be conclusively identified, since the observed energy losses were also contaminated by the presence of the decay secondaries. As a result of the unfeasibility of obtaining accurate estimates of the degree of contamination in the low-momentum kaon sample, the inclusive kaon production cross sections are quoted only for momenta greater than 0.7 GeV/c.

F. Inclusive Hadron Production Cross Sections

1. The Differential Momentum Spectrum

Table VI-1 and Fig. VI-7 show the inclusive momentum spectra for charged pions and kaons, and twice that of antiprotons. The total center of mass energy is 4.8 GeV. In Fig. VI-7 and in most of the later figures, comparisons are made with the low-momentum data of the SLAC-LBL collaboration.[7] That experiment used a large solid angle solenoid detector[8] and took data at total CM energies of 3.8 and 4.8 GeV, among others. At present, no other e^+e^- data exists near these energies, except that taken at the ψ and ψ' resonances, which is not directly comparable.

The errors shown are dominated by the hadron statistics, and do not include a ±7.3% normalization uncertainty arising from the

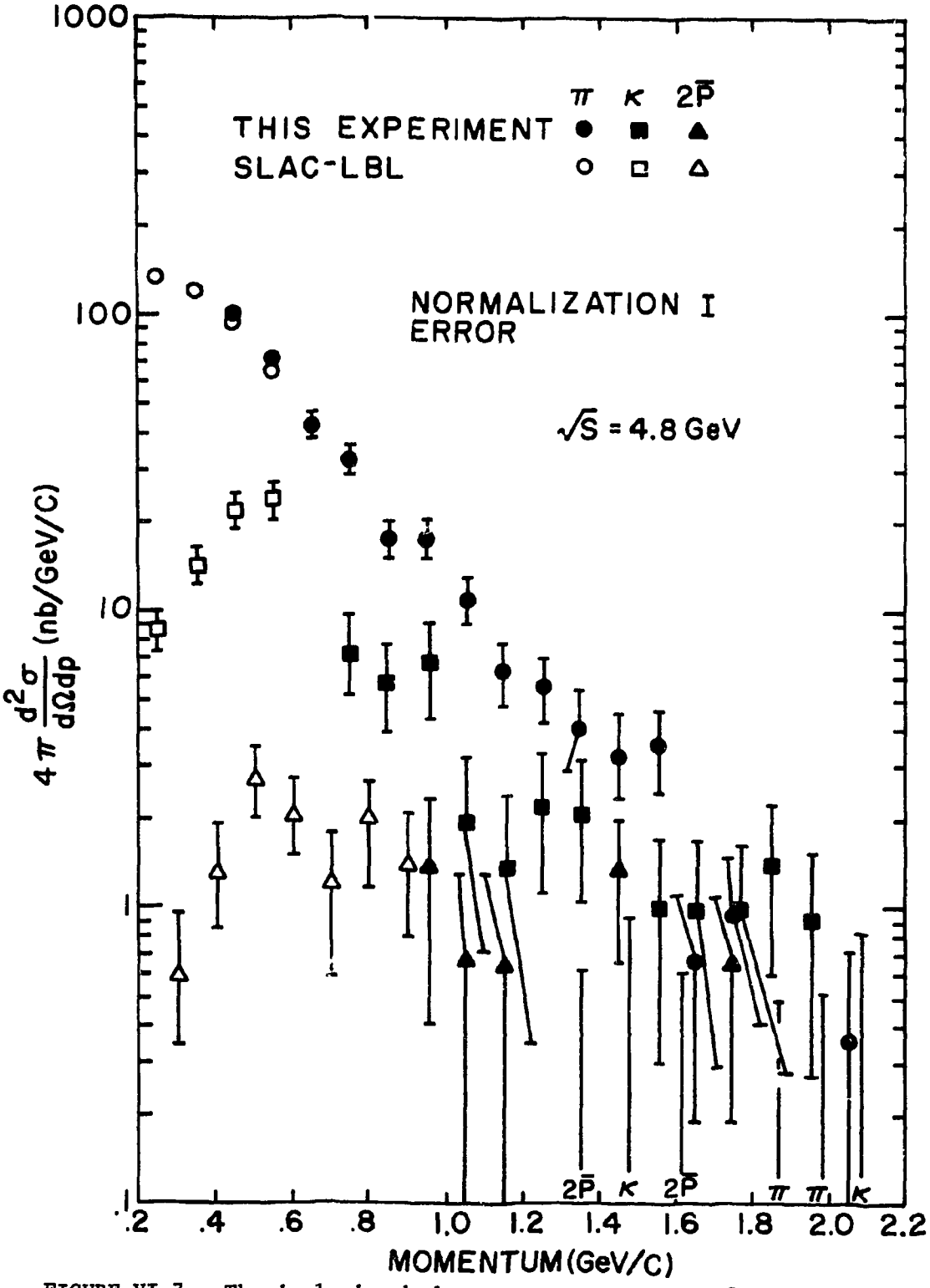

FIGURE VI-7. The inclusive hadron momentum spectrum for pions, kaons and antiprotons at 4.8 GeV.

TABLE VI-1. Differential momentum spectrum, $4\pi d^2\sigma/d\Omega dp$ at 4.8 GeV. Units are nb/GeV/c. The quoted errors include statistical uncertainties and misidentification errors. Not included are a ±7% normalization uncertainty and a ±1.8% uncertainty due to the corrections for nuclear attenuation and Cerenkov counter accidentals. A * indicates an upper limit at the 85% confidence level. A † indicates pions only.

Momentum	Pions	Kaons	Protons ($2\bar{P}$)	Total
0.4-0.5	101. ± 7.		0.86*	101. ± 7.†
0.5-0.6	74.5 ± 5.2		0.74*	74.5 ± 5.2†
0.6-0.7	43.0 ± 3.8		0.68*	43.0 ± 3.8†
0.7-0.8	33.0 ± 3.4	7.37 ± 2.33	0.67*	40.4 ± 4.1
0.8-0.9	17.7 ± 2.6	5.81 ± 1.94	0.65*	23.5 ± 3.2
0.9-1.0	17.8 ± 2.6	6.73 ± 2.42	1.37 ± 0.97	25.9 ± 3.7
1.0-1.1	11.0 ± 2.0	1.98 ± 1.26	0.67 ± 0.67	13.6 ± 2.4
1.1-1.2	6.36 ± 1.51	1.38 ± 1.04	0.65 ± 0.65	8.39 ± 1.95
1.2-1.3	5.55 ± 1.35	2.22 ± 1.11	0.62*	7.77 ± 1.75
1.3-1.4	4.03 ± 1.16	2.11 ± 1.05	0.62*	6.13 ± 1.57
1.4-1.5	3.42 ± 1.08	0.94*	1.33 ± 0.66	4.74 ± 1.27
1.5-1.6	3.52 ± 1.11	1.01 ± 0.71	0.61*	4.53 ± 1.32
1.6-1.7	0.66 ± 0.47	0.98 ± 0.69	0.60*	1.63 ± 0.83
1.7-1.8	0.95 ± 0.55	0.96 ± 0.68	0.64 ± 0.45	2.55 ± 0.98
1.8-1.9	0.49*	1.40 ± 0.81	0.59*	1.40 ± 0.81
1.9-2.0	0.52*	0.92 ± 0.65	0.59*	0.92 ± 0.65
2.0-2.1	0.36 ± 0.36	0.83*	0.59*	0.36 ± 0.36

TABLE VI-2. Differential momentum spectrum, $4\pi d^2\sigma/d\Omega dp$ at 3.8 GeV. Units are nb/GeV/c. The quoted errors include statistical uncertainties and misidentification errors. Not included are a ±12% normalization uncertainty and a ±1.8% uncertainty due to the corrections for nuclear attenuation and Cerenkov counter accidentals. A * indicates an upper limit at the 85% conficence level. A † indicates pions only.

Momentum	Pions	Kaons	Protons ($2\bar{P}$)	Total
0.4-0.5	120. ± 16.		4.06*	120. ± 16.†
0.5-0.6	91.1 ± 12.9		3.40*	91.1 ± 12.9†
0.6-0.7	28.9 ± 7.0		3.27*	28.9 ± 7.0†
0.7-0.8	27.4 ± 6.6	6.73 ± 6.16	3.04*	34.1 ± 9.1
0.8-0.9	23.2 ± 6.3	3.02 ± 3.90	3.06*	26.2 ± 7.4
0.9-1.0	6.48 ± 3.24	4.90*	2.99*	6.48 ± 3.24
1.0-1.1	6.18 ± 3.09	2.29 ± 2.29	2.86*	8.47 ± 3.85
1.1-1.2	4.64 ± 2.67	3.92*	2.78*	4.64 ± 2.67
1.2-1.3	1.19 ± 1.19	5.19 ± 3.67	2.91*	6.38 ± 3.86
1.3-1.4	4.75 ± 2.74	2.46 ± 2.46	2.90*	7.21 ± 3.68
1.4-1.5	1.55 ± 1.55	2.36 ± 2.36	2.87*	3.91 ± 2.83
1.5-1.6	2.76*	4.35*	2.84*	----
1.6-1.7	1.48 ± 1.48	4.22*	2.80*	1.48 ± 1.48
1.7-1.8	1.48 ± 1.48	4.12*	2.78*	1.48 ± 1.48

collinear mu pair statistics, or a ±1.8% uncertainty resulting from the corrections applied to the cross sections. The normalization uncertainty for the 3.8 GeV data was ±12.4%. The upper limits shown for bins where no particles were detected are identified in the figures with the type of particle indicated along the lower border. They are calculated for an 84% confidence level, corresponding to the one-standard-deviation error bars.

The particle production rates of the SLAC-LBL[7] group are seen to rise at low momentum; then both sets of data show that the rates fall with different slopes until they become roughly equal at the highest momenta, given the uncertainties. The SP8 pion and antiproton data is seen to be in good agreement with that of SLAC-LBL[7] where they overlap. Unfortunately, the difficulty of identifying low-momentum kaons in the spectrometer precluded a direct comparison there.

The SLAC-LBL group were able to reproduce their momentum spectrum quite closely using a simple phase space model and assuming all particles to be pions.[9] The only large disagreement occurred in the high-momentum tail, and this might be accounted for by the comparatively higher kaon and proton production occurring there, as seen in Fig. VI-7. As pointed out by G. Feldman and M. Perl,[9] this agreement with simple phase space assumptions means that any dynamical effects which might be present in the momentum spectrum are quite small, so that the spectrum alone would probably not provide significant dynamical information.

Another qualification of the results shown in Fig. VI-7 should be made. While the overall hadron angular distribution has been

found to be consistent with isotropy,[10,11] this in no way precludes the possibility of there being some angular dependence in the high-momentum portion of the spectrum. Such dependence would be obscured in the total sample by the large number of isotropic hadrons occurring at lower momenta. It is also worth observing that the higher momentum events tend towards lower particle multiplicities, a trend which might favor nonisotropic distributions, given the existence of a suitable underlying dynamical mechanism. For this reason, the direct extension of the SLAC-LBL values for $d\sigma/dp$ through the SP8 values of $4\pi d^2\sigma/d\Omega dp$ should be made with care, to the extent that the two solid angles were substantially different. The assumption of isotropy in the low momentum pion data of SLAC-LBL appears to be sound. Presumably, as more data is accumulated over large solid angles, this uncertainty will be eliminated.

2. The Lorentz Invariant Differential Cross Section

Another quantity of interest is the Lorentz invariant differential cross section, which represents the hadron production rates into equal volumes of phase space. The invariant cross sections for pions and kaons are shown in Fig. VI-8 as a function of the hadron momentum for a center of mass energy of 4.8 GeV. The measured values are given in Table VI-3.

In Fig. VI-9 a comparison is made between the invariant cross sections at the two different center of mass energies 3.8 and 4.8 GeV. In this figure a sum was performed over the pion, kaon and antiproton spectra to obtain the overall distribution. Within the rather large errors shown, it is clear, at least over the 1 GeV CM energy range

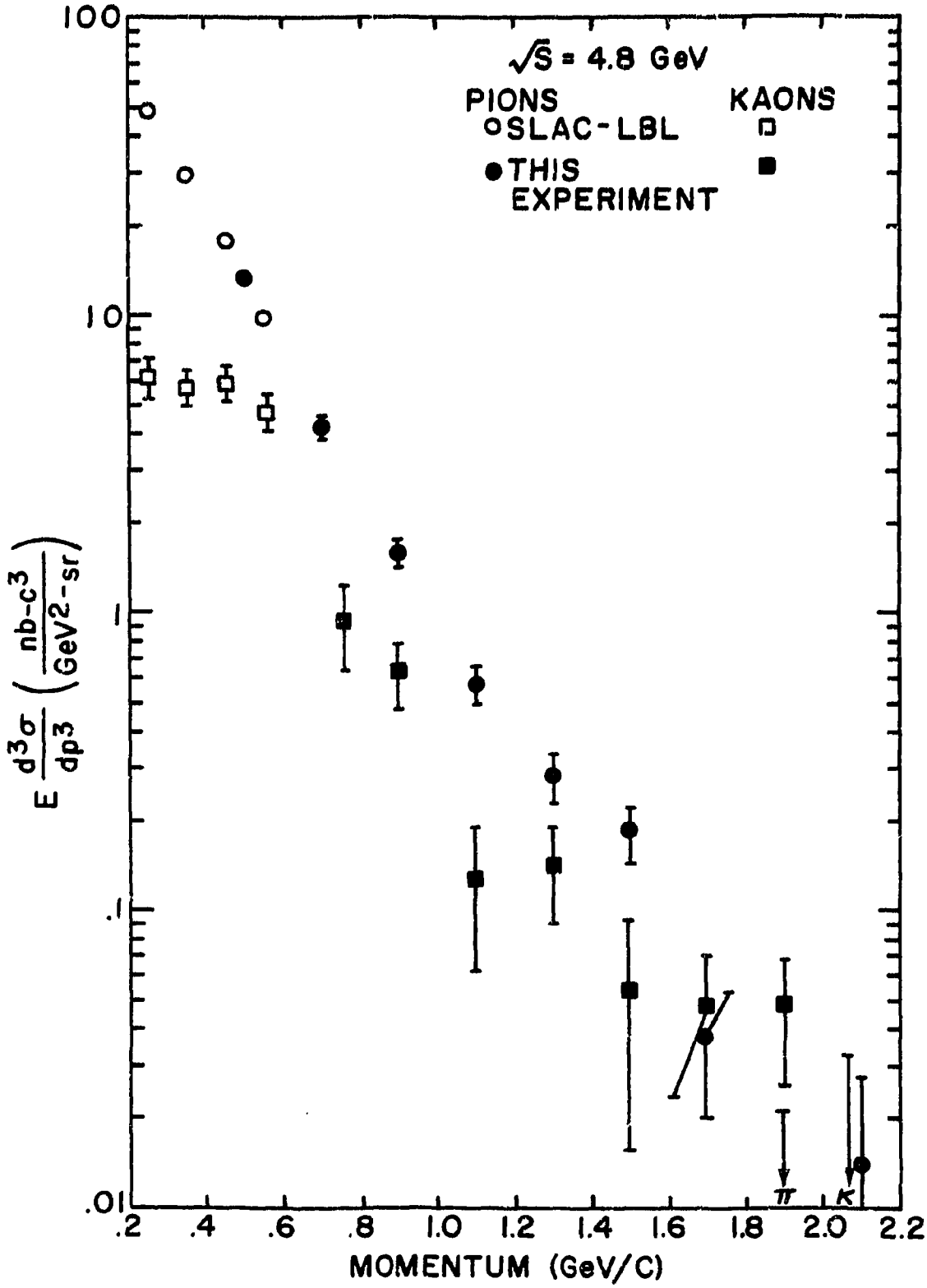

FIGURE VI-8. The Lorentz invariant cross section for pions and kaons at 4.8 GeV, as a function of momentum.

TABLE VI-3. The invariant cross section $Ed^3\sigma/dp^3$ at 4.8 GeV. Units are nb-c^3/GeV^2-sr. The quoted errors include statistical uncertainties and misidentification errors. Not included are a ±7% normalization uncertainty and a ±1.8% uncertainty due to the corrections for nuclear attenuation and Cerenkov counter accidentals. A * indicates an upper limit at the 85% confidence level. A † indicates pions only.

Momentum	Pions	Kaons	Protons ($2\bar{P}$)	Total
0.4-0.5	18.6 ± 1.2		0.35*	18.6 ± 1.2†
0.5-0.6	11.1 ± 0.8		0.21*	11.1 ± 0.8†
0.6-0.7	5.38 ± 0.48		0.15*	5.38 ± 0.48†
0.7-0.8	3.57 ± 0.37	.936 ± .296	0.11*	4.50 ± 0.47
0.8-0.9	1.67 ± 0.25	.629 ± .210	.091*	2.30 ± 0.32
0.9-1.0	1.51 ± 0.22	.635 ± .228	.161 ± .114	2.31 ± 0.34
1.0-1.1	.841 ± .150	.166 ± .106	.068 ± .068	1.07 ± 0.20
1.1-1.2	.444 ± .105	.104 ± .078	.058 ± .058	.605 ± .144
1.2-1.3	.355 ± .086	.152 ± .076	.050*	.508 ± .115
1.3-1.4	.239 ± .069	.132 ± .066	.045*	.371 ± .095
1.4-1.5	.189 ± .060	.054*	.087 ± .043	.275 ± .074
1.5-1.6	.181 ± .057	.054 ± .038	.037*	.236 ± .069
1.6-1.7	.032 ± .023	.049 ± .035	.033*	.081 ± .041
1.7-1.8	.043 ± .025	.045 ± .032	.033 ± .024	.122 ± .047
1.8-1.9	.021*	.062 ± .036	.029*	.062 ± .036
1.9-2.0	.021*	.039 ± .027	.027*	.039 ± .027
2.0-2.1	.014 ± .014	.033*	.025*	.014 ± .014

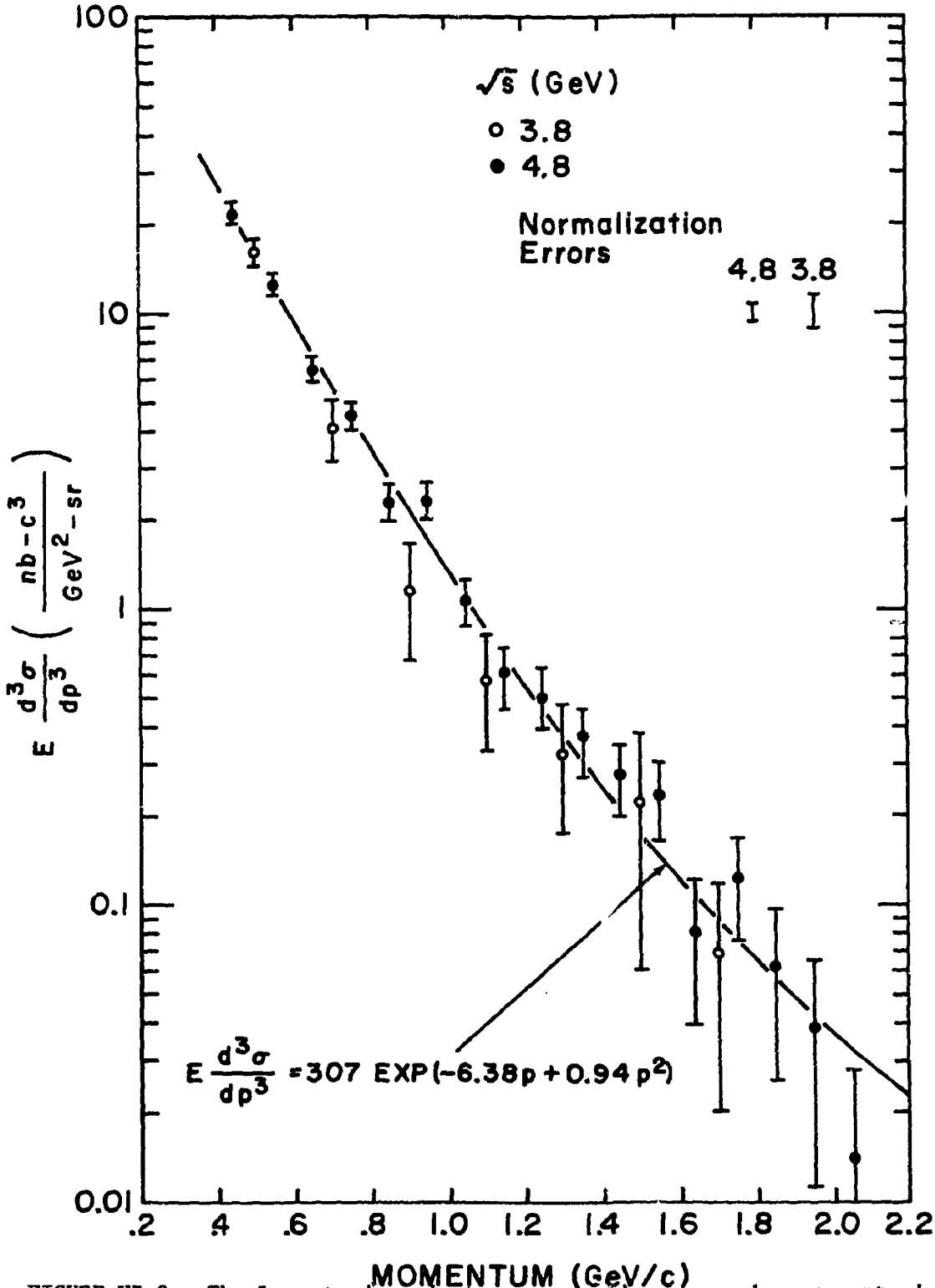

FIGURE VI-9. The Lorentz invariant cross sections summed over particle types, as a function of the hadron momentum. The data were taken at center of mass energies of 3.8 and 4.8 GeV. The values quoted for $p < .7$ GeV/c are for pions only. The smooth curve is the best fit to the 4.8 GeV data.

separating the two samples, that some form of scaling occurs in this momentum spectrum. This behavior was also observed by the SLAC-LBL solenoid group and has been termed "Feynman scaling"[12] in p because of its similarity to the phenomenon of the same name observed in the $p_\perp$ distributions in hadron-hadron interactions.[9] Such scaling behavior can be represented as

$$E \frac{d^3\sigma}{dp^3} \rightarrow f(p) \quad .$$

In order to quantify the observed scaling behavior, the invariant cross sections were fit using three-parameter exponential functions. The resulting fit at 4.8 GeV is given by

$$Ed^3\sigma/dp^3 = A \exp(bp + cp^2)$$

$$= 307 \cdot \exp(-6.4p + 0.94p^2) \ ,$$

where the cross section is expressed in the units of Fig VI-9 and the momentum in GeV/c. The χ^2 for this fit was 13.4 for 14 degrees of freedom, giving a confidence level of 0.49. Fitting the 3.8 GeV data to the same exponent resulted in an intercept of A = 267. This fit had a χ^2 of 5.12 for 6 degrees of freedom, giving a confidence level of 0.53. The uncertainties in these two intercepts resulted from the normalization errors for each data sample and the uncertainties in the cross section correction factors. A comparison of the two intercepts together with their respective uncertainties is given by

$$A_{3.8} = 267 \pm 33 \quad , \quad A_{4.8} = 307 \pm 23 \quad .$$

The degree of agreement between these two intercepts can be expressed by forming the χ^2 for their difference, which gives 0.94 for one

degree of freedom, corresponding to a confidence level of 0.32.

Integrating the invariant cross section over momentum gives the result that

$$\int E \frac{d^3\sigma}{dp^3} d^3p = \overline{E}_{ch}\sigma_h \ .$$

Here $\overline{E}_{ch}$ is the average total energy in charged particles and σ_h is the total hadronic cross section. If Feynman scaling holds, then this quantity should be independent of CM energy. The SLAC-LBL results seem to bear this out, at least within the current measurement uncertainties. Since the SP8 spectrometer measured the momentum of only one particle per event, and only for $p > 0.4$ GeV/c, accurate estimates of $\overline{E}_{ch}$ and σ_h could not be made.

Plotting the invariant cross section as a function of the energy of the hadron leads to another interesting result, as shown in Fig. VI-10. The figure shows the cross sections for pions, kaons and antiprotons as measured by SP8 and by SLAC-LBL. The production cross sections for all three types of particles appear to lie on or near the same exponential curve. The curve shown in Fig. VI-10 is the same as that found by SLAC-LBL and roughly fits their low-momentum data from center of mass energies of 3.0 GeV to 7.4 GeV.[7] This apparent tendency of the cross section to depend only on the particle's energy is a type of behavior predicted in statistical models,[13] where the CM energy released by the e^+e^- interaction is assumed to be distributed among the resultant hadron degrees of freedom according to the laws of thermodynamics. In these models, the hadronic "temperature" manifests itself in the exponential slope of the cross section, which from

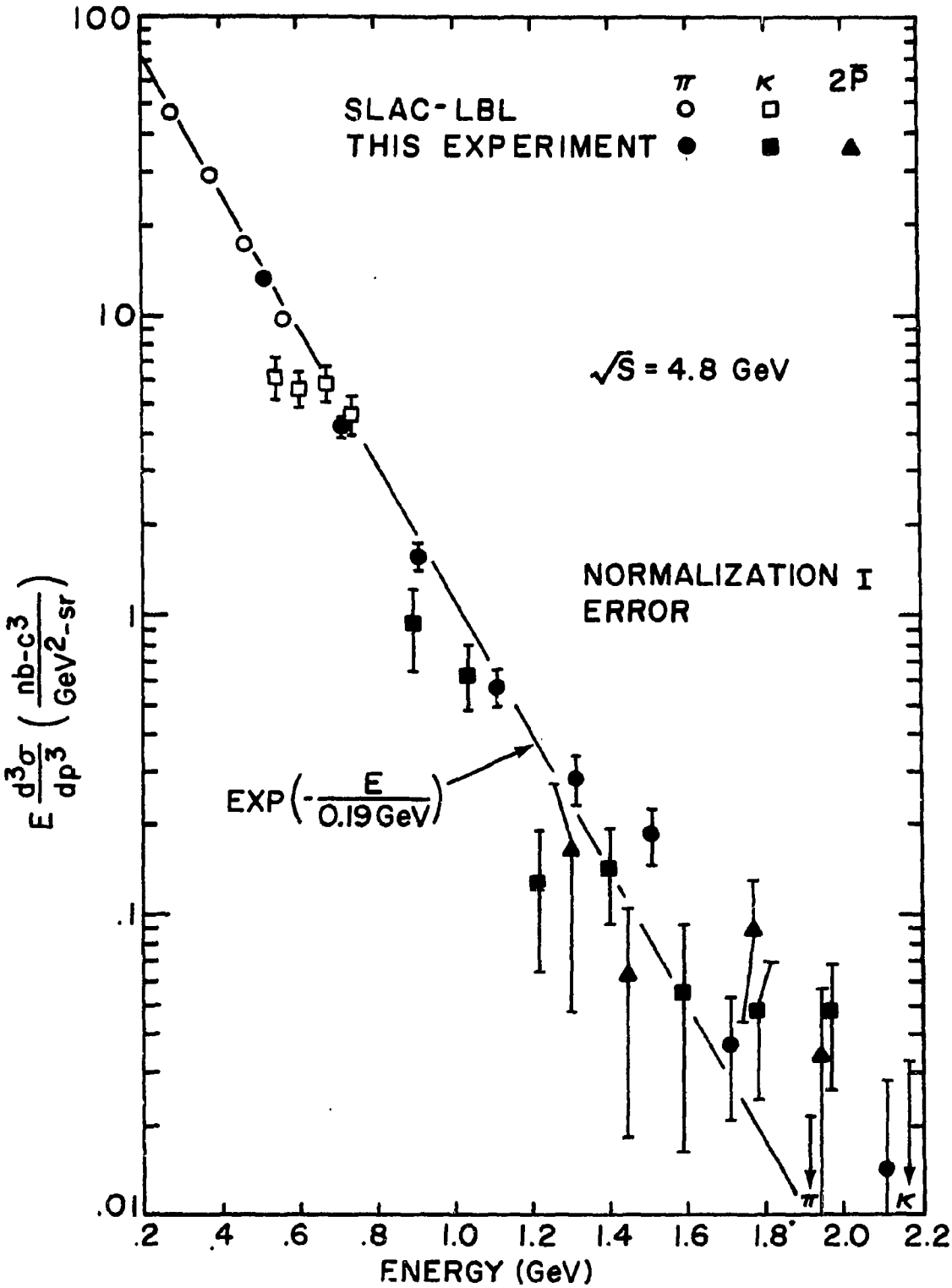

FIGURE VI-10. The Lorentz invariant cross section for pions, kaons and antiprotons as a function of the hadron energy. The data were taken at a total center of mass energy of 4.8 GeV.

Fig. VI-10 gives

$$kT = 0.19 \text{ GeV} .$$

3. The "Scaling" Cross Section

It was predicted by Bjorken[14] and subsequently observed that in lepton-nucleon interactions, the hadron production structure functions depend only upon a single "scaling variable",

$$\omega = \frac{2P\cdot q}{|q^2|} ,$$

in the region where $|q^2|$ and $P\cdot q$ are large. The quantities q and P are the four-momenta of the exchanged virtual photon and the incident nucleon. This behavior is much simpler than the more general dependence upon q^2 and $P\cdot q$ separately, which can be deduced from Lorentz invariance and current conservation. The phenomenon of scaling results from the assumption of pointlike constituents of the hadron as predicted in the various parton models.

In attempting to assess the effects of such predictions upon inclusive hadron production in e^+e^- interactions, one may observe that

$$q^2 = s \quad \text{and} \quad \omega = \frac{2P\cdot q}{|q^2|} = \frac{2E}{\sqrt{s}} \equiv x ,$$

where E is the energy of the hadron and $\sqrt{s}$ the total center of mass energy. The scaling predictions are that the differential cross section as a function of x will have the form

$$\frac{d^2\sigma}{d\Omega dx} = \frac{\alpha^2 x\beta}{s}\{W_1(x) + (x\beta^2/4)W_2(x)\sin^2\theta\},$$

where β is the velocity of the measured hadron. To the extent that one can assume that

$$\beta \to 1 ,$$

one can integrate over the solid angle to obtain

$$s\frac{d\sigma}{dx} \simeq 4\pi\alpha^2 x\{W_1(x) + (x/6)W_2(x)\} \to f(x).$$

Thus, if this cross section is plotted as a function of the scaling variable x, one expects to find for $\beta \to 1$ that there is no dependence of s or E other than that contained in x.

A plot of this scaling cross section is shown in Fig. VI-11 using the SP8 and SLAC-LBL data for pions at CM energies of 3.8 and 4.8 GeV. Within the errors the scaling holds for $x > 0.3$ over this energy range. It is well known that Bjorken scaling cannot occur over all x. This not only follows from the assumption that $\beta \to 1$, but from the observation that

$$\int s\frac{d\sigma}{dx}\,dx \simeq s\bar{n}_{ch}\sigma_h = \frac{4\pi\alpha^2}{3}R\bar{n}_{ch} ,$$

where $\bar{n}_{ch}$ is the mean charged multiplicity and R the ratio of the total hadron cross section to the cross section for producing collinear muon pairs. The right hand side has been observed to increase with s throughout this CM energy region.[7]

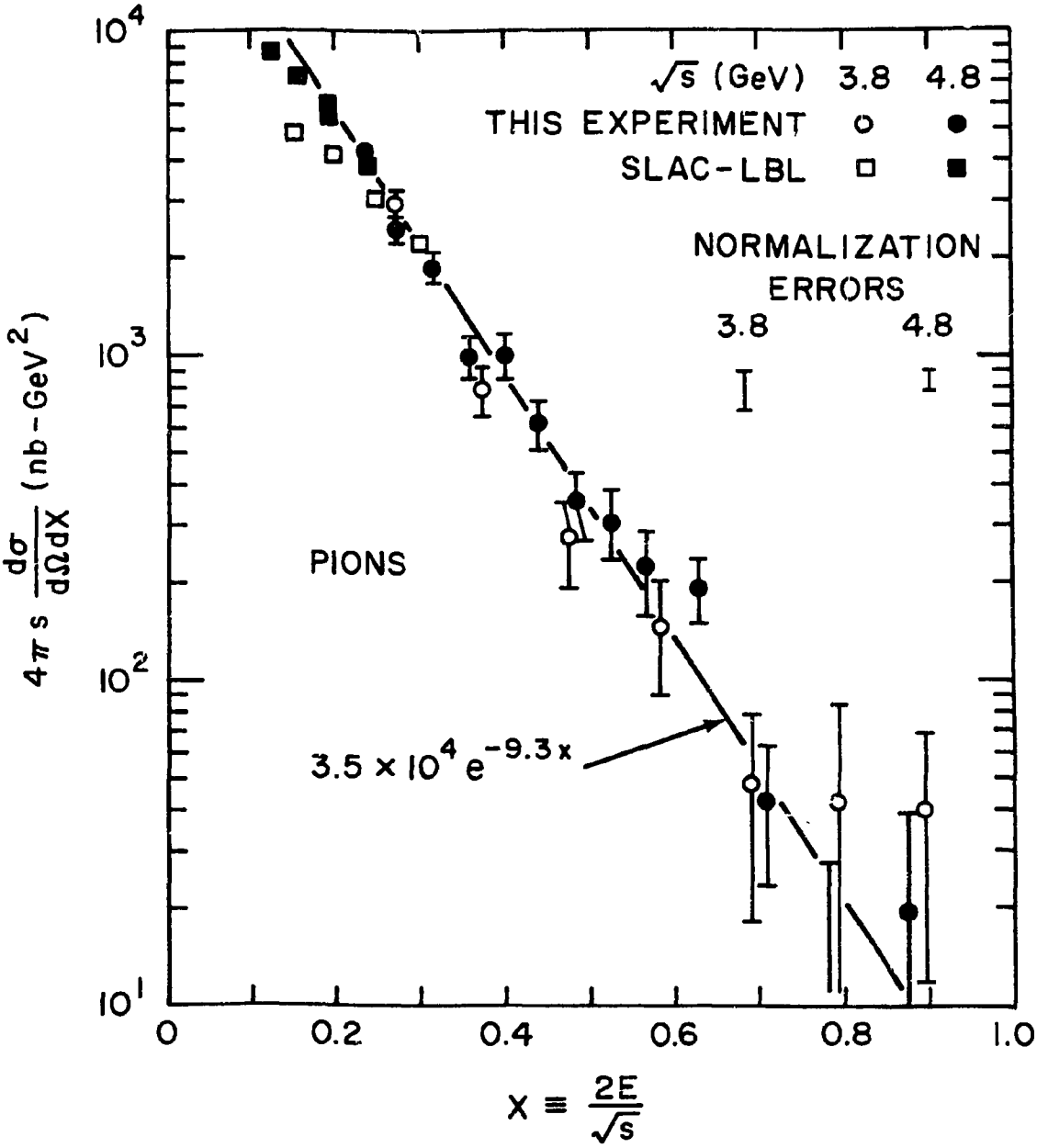

FIGURE VI-11. The "scaling cross section" for pions at center of mass energies of 3.8 and 4.8 GeV. The exponential was fit to the 4.8 GeV data.

Figure VI-12 shows a similar plot for kaons. Unfortunately, the errors are quite large. However, the figure appears consistent with scaling within this species for $x > 0.4$. A comparison between pions, kaons and protons at the same energy is shown in Fig. VI-13. A two-parameter fit was made to the 4.8 GeV pion scaling cross section, with the result that

$$4\pi s \frac{d\sigma^2}{d\Omega dx}\Big|_\pi = 3.50 \times 10^4 \; e^{-9.26x} \text{ nb-GeV}^2 \; .$$

The χ^2 for this fit was 6.29 for 5 degrees of freedom, giving a confidence level of 0.28. Fitting the 4.8 GeV kaon cross section to the same exponent gives

$$4\pi s \frac{d\sigma^2}{d\Omega dx}\Big|_K = 1.74 \times 10^4 \; e^{-9.26x} \text{ nb-GeV}^2 \; ,$$

with a χ^2 of 9.03 for 6 degrees of freedom. This gave a confidence level of 0.17. The intercepts for the pions and kaons differ by about a factor of two, suggesting that the two cross sections are significantly different. A further measure of this difference was that the χ^2 for the fit of the kaon cross section using both the same slope and the same intercept as for the pions was 50.8 for 7 degrees of freedom, giving an extremely low confidence level less than 10^{-6}.

4. Particle Fractions

Another quantity of physical interest is the particle fraction distribution as a function of momentum. As an example, the pion fraction is defined by

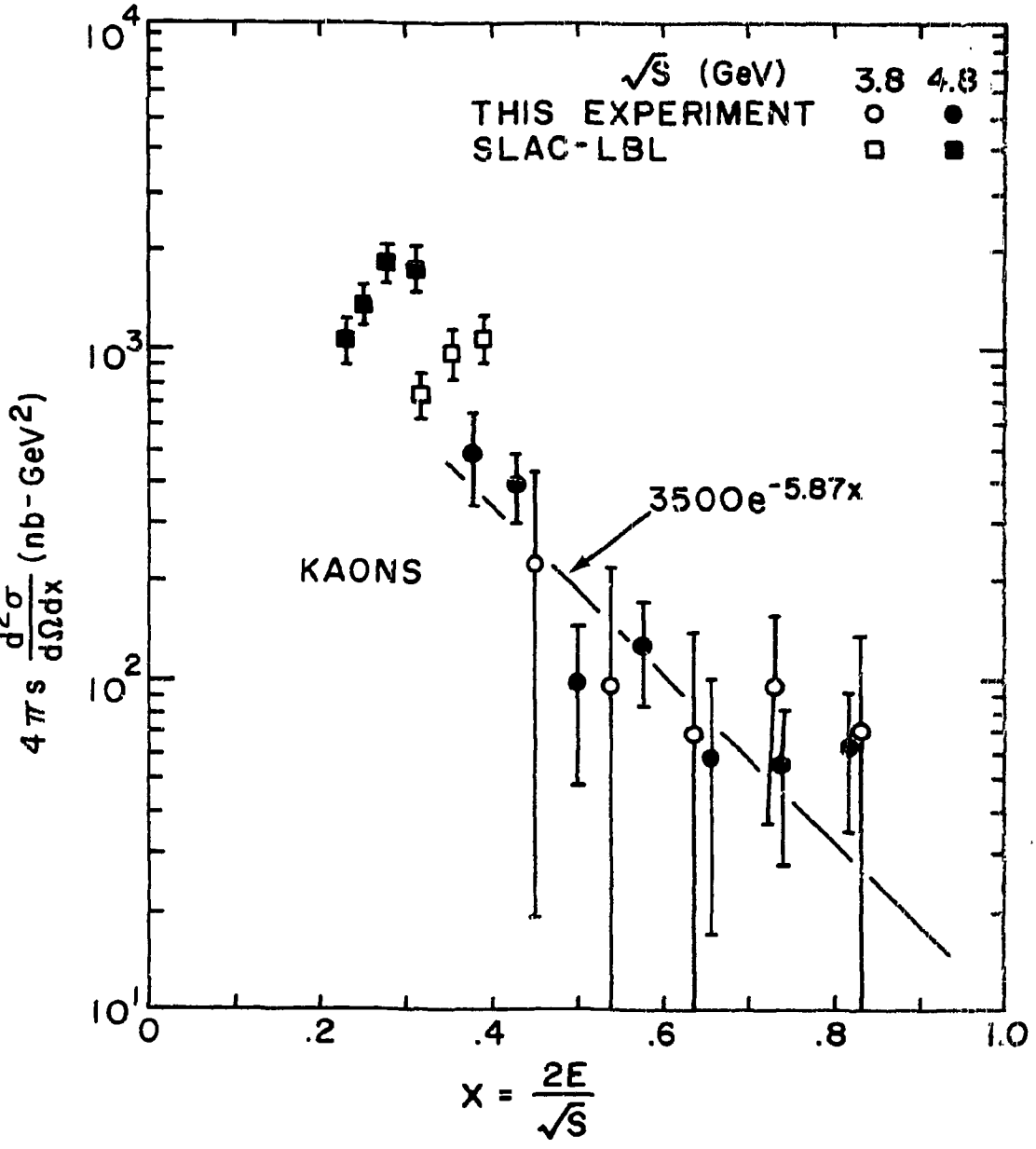

FIGURE VI-12. The "scaling cross section" for kaons at center of mass energies of 3.8 and 4.8 GeV. The exponential was fit to the 4.8 GeV data.

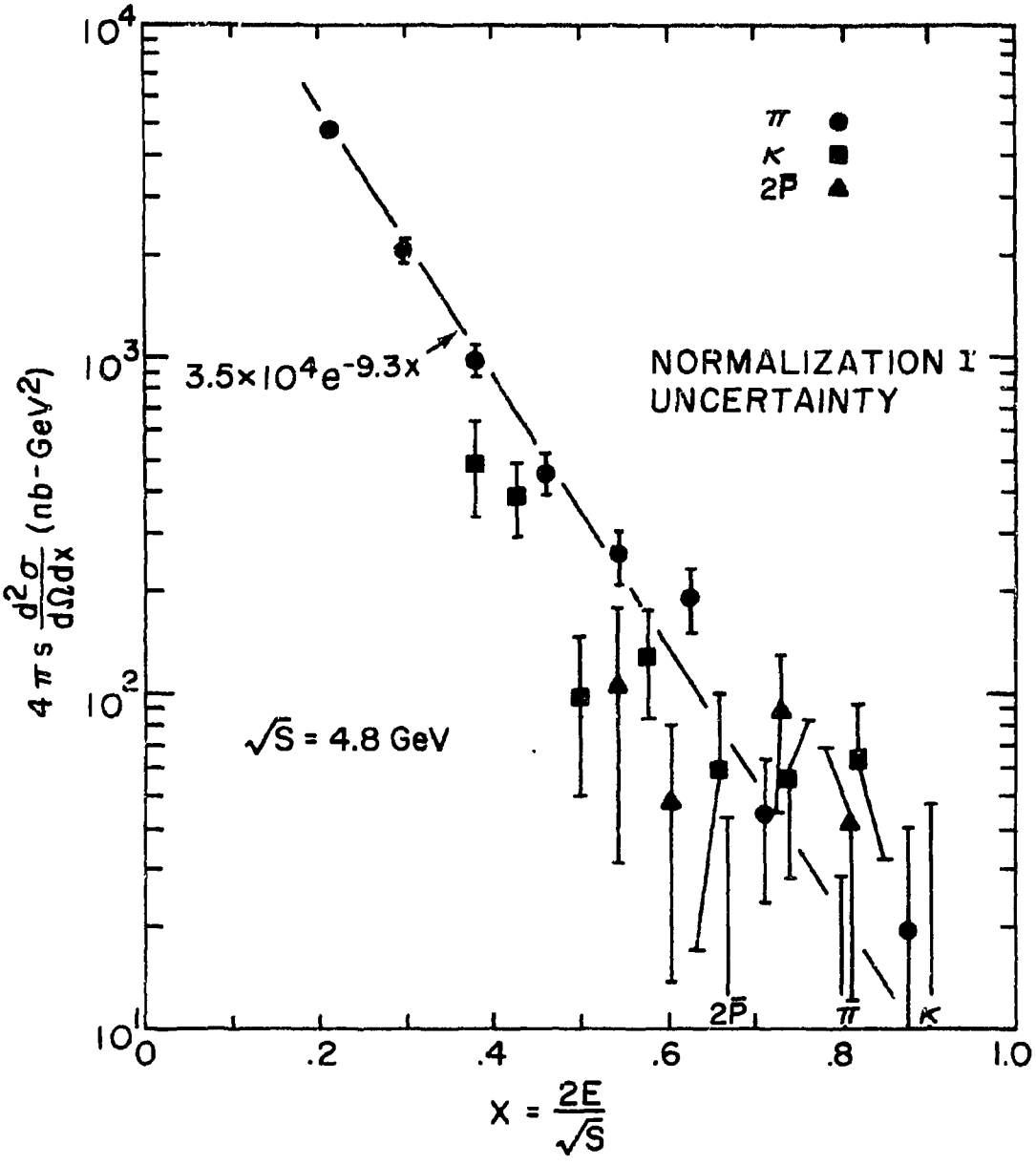

FIGURE VI-13. The scaling cross section for pions, kaons and anti-protons at a total center of mass energy of 4.8 GeV. The exponential was fit to the pion data.

$$f_\pi = \frac{N_\pi}{N_\pi + N_K + 2N_{\bar{P}}} ,$$

where the N's are the numbers of particles produced in each momentum bin. The observed results at 4.8 GeV are shown in Fig. VI-14. Also shown are the low-momentum results of the SLAC-LBL collaboration.[7] Although the data do not overlap, the rate of increase of the kaon fraction with momentum is much larger in the SLAC-LBL data and would have to suggest a large low-momentum peak if the two sets of data were to be consistent.

Some doubt is cast on this by the comparison of the SLAC-LBL data with that of the DASP double-arm spectrometer data,[15] both taken at the ψ resonance. As shown in Fig. VI-15, the SLAC-LBL kaon fractions were significantly higher than those measured by the DASP collaboration at the same energy. Although the SP8 data taken at 4.8 GeV is not directly comparable with the 3.1 and 3.7 GeV DASP data, the particle fractions at these different energies appear to be in agreement over the entire momentum range measured, within the rather large SP8 uncertainties.

The observed behavior in the SP8 data is that the kaon fraction rises gradually from about 0.1 at 0.8 GeV/c to about 0.4 at p = 1.8 GeV/c. The antiproton fraction appears to rise at about half that rate.

G. Charged Multiplicity Distributions

The charged multiplicity associated with each spectrometer trigger event was determined from the number of tracks reconstructed in the polymeter, which extrapolated near the center of the beam

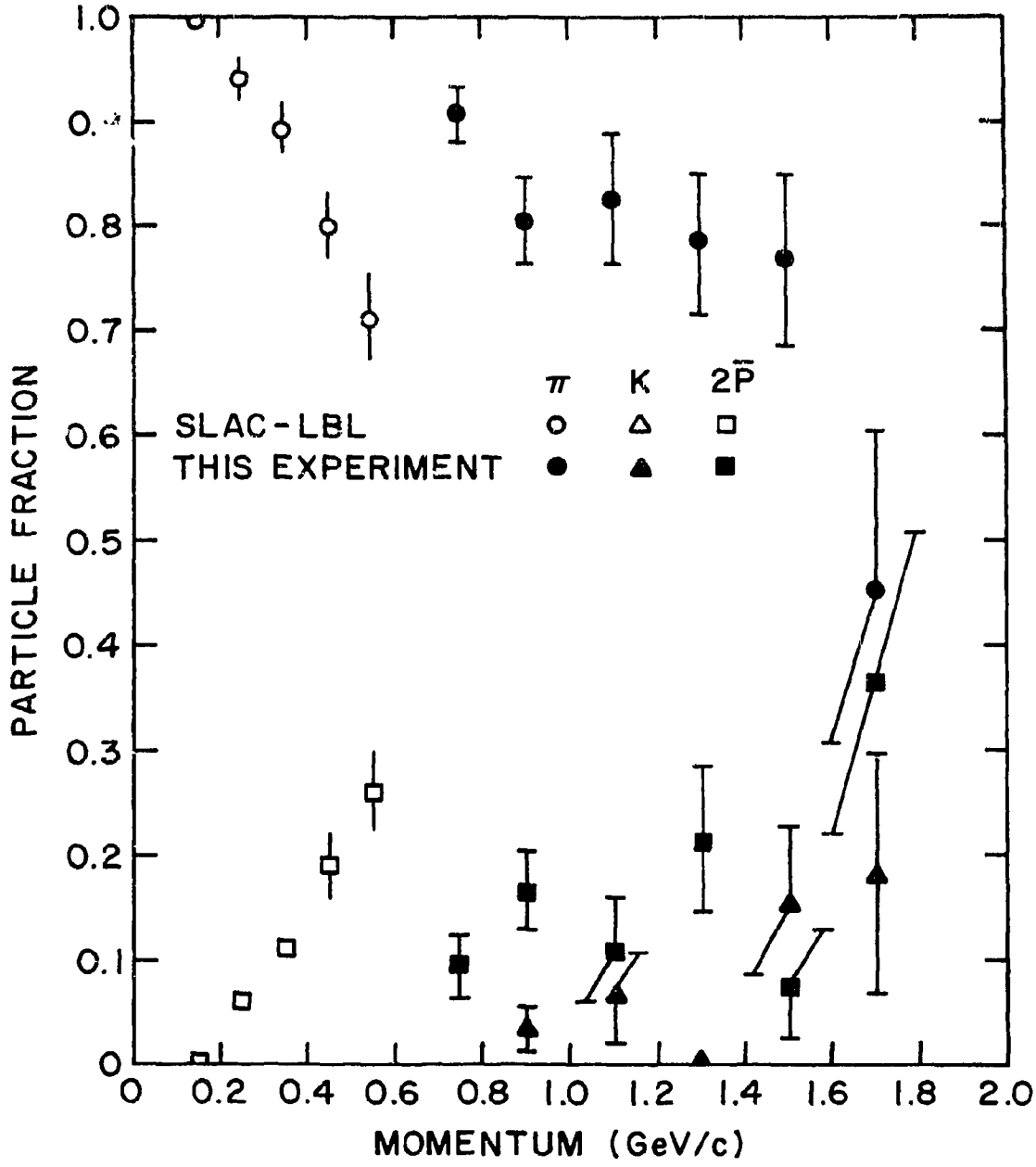

FIGURE VI-14. The particle fractions as a function of momentum at a total center of mass energy of 4.8 GeV.

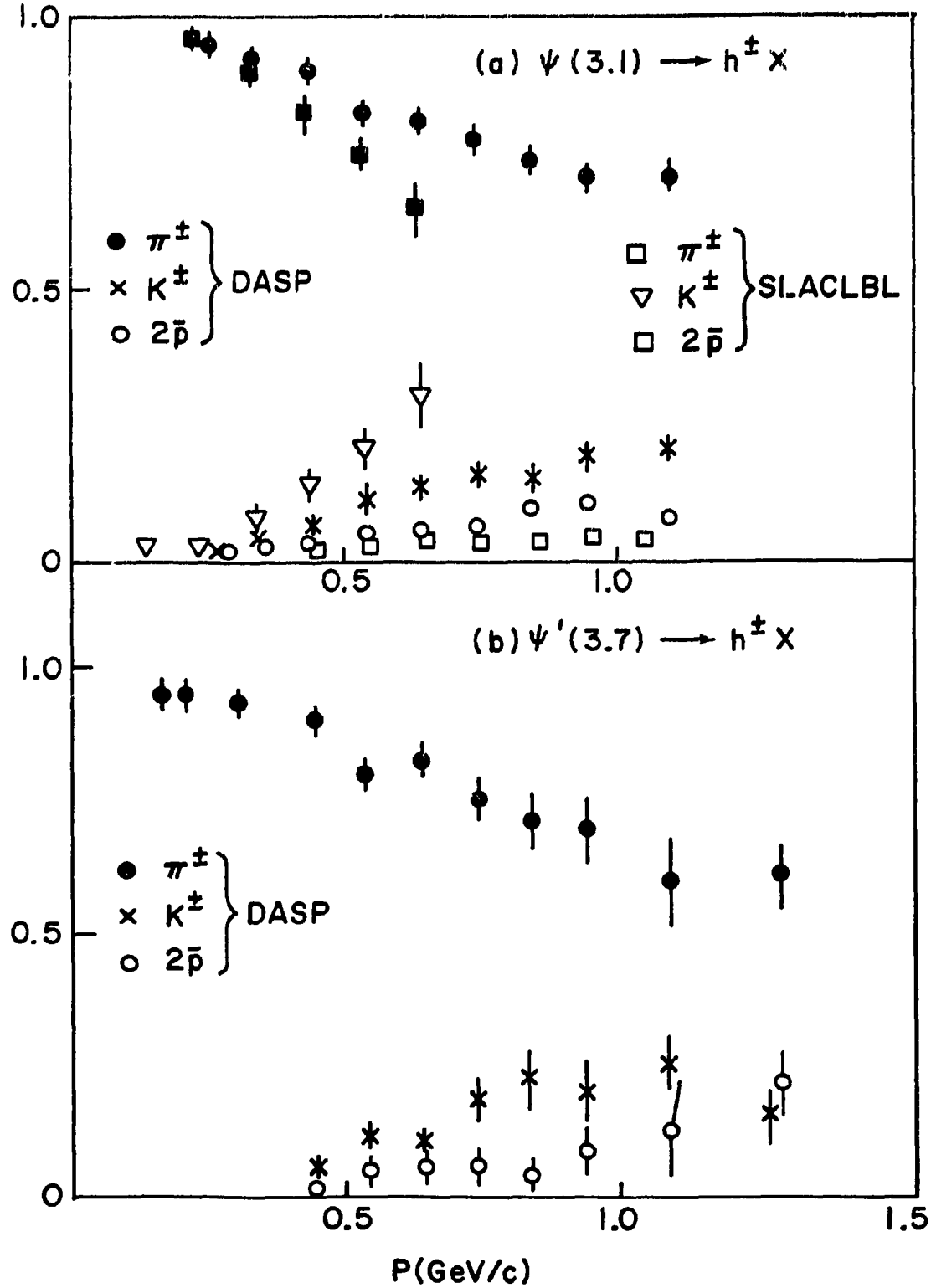

FIGURE VI-15. Hadron particle fractions observed (a) at the $\psi(3100)$ by the DASP and SLAC-LBL collaborations, and (b) at the $\psi'(3700)$ by the DASP collaboration. The DASP and SLAC-LBL measurements at the ψ are seen to be in rather strong disagreement. The data are from Ref. 15.

interaction region. The physical characteristics of the polymeter are described in Section II-D. The track reconstruction is discussed in Section III-D. The observed multiplicity for each event was determined by counting the number of 2 and 3-point tracks having their point of closest approach to the beam interaction region (also termed their "origin") within 4 standard deviations of the center of the beam interaction region. This 4 standard deviations was the calculated uncertainty in the extrapolated position resulting from the 3mm wire spacing, the number of polymeter planes having points in the track (2 or 3) and the number of wires firing in each plane (the size of the "cluster").

There were several effects which tended to introduce errors in the multiplicity count. In order to yield the physical charged multiplicity from the measured multiplicity, the analysis had to include corrections for these effects.

Perhaps the most obvious source of error was the fact that the polymeter did not cover 100% of 4π sterradians. In order to allow for the beam pipe, there were gaps in either end. In addition, there were small angular regions where overlapping support wires in different planes caused two planes at a time to be dead, thus precluding track reconstruction. Taking both of these effects into account, the effective solid angle over which tracks could be reconstructed was 97.3% of 4π.

Another obvious contributor to measurement errors in the charged multiplicity was inefficiency in the polymeter chambers. Because of its compact design it was not possible to separately regulate the high voltage across individual wire planes. Rather, the voltage was

the same for all three planes in each chamber. This occasionally resulted in relatively low efficiency for some of the individual planes. The average efficiency for detecting charged tracks was extrapolated from the single-plane efficiencies, which were determined by comparing the relative numbers of 2 and 3-point tracks. The average track-detection efficiency was found to be 98.5%. This number included a weighting over the angular region subtended by the C2AY and C2BY chambers, where the additional chambers made track detection nearly 100% efficient. Combining the detection efficiency with the solid angle coverage gave an average track-detection inefficiency of 4.46%.

Additional tracks could be added to an event if any of the photons produced by the event converted before passing through the polymeter. One might expect that most of these photons resulted from the decay of neutral pions in the vicinity of the beam interaction region. However, in order to make a correction for gamma conversion, one must first have had some knowledge of the numbers of photons present and their energy distribution. In the absence of such knowledge, a self-consistent approach was taken, using the requirement that the charged multiplicity be some multiple of 2. This constraint gave sufficient information to determine not only the physical multiplicity, but to provide a rough idea of the average number of gammas present per event.

The conversion probability was determined using the approximate cross section

$$\sigma_{pair} \approx \frac{7}{9} \cdot \frac{1}{NX_o} \quad ,$$

where N is the number of atoms per gram and X_o the radiation length. The effective thicknesses of the materials composing the beam vacuum pipe and parts of the polymeter were averaged over the solid angle using a three-dimensional integration. The average probability for a gamma to convert into an electron-positron pair such that the track could be reconstructed in the polymeter was 7.2%.

One additional correction remains to be discussed. That is the case when two or three wire planes in the polymeter experienced overflows. A maximum of 15 wires per plane were allowed to be recorded. If more than this number were excited, the result was an overflow, and hits beyond the 15th wire were not recorded.

Two types of effects were responsible for overflow. If the multiplicity were high and two or more adjacent wires fired in some of the tracks, the number 15 could have been exceeded, resulting in an overflow. Clearly this type of occurrence was much more likely for high-multiplicity events. The other principal source of overflow was the case where some stray particle, such as a delta-ray, a decay product, or a cosmic ray secondary, struck the polymeter at a highly non-perpendicular orientation, in which case many wires could fire from the same track. More often than not, such a track would not have been counted, because of its large distance of closest approach to the beam interaction region. Nevertheless, it would still result in a sudden overflow. This type of overflow could happen somewhat randomly and was not significantly dependent upon the charged multiplicity of the event.

In order to obtain a well-understood sample of events, the requirement was made that there be no more than one overflow per

event. This allowed all tracks to be reconstructed in at least 2 planes over the full 2π azimuthal angle. This procedure, having removed events with multiple overflows, then required a correction for the high-multiplicity bias of those events. The assumption was made that the events having overflows due to highly tangential tracks were distributed independently of multiplicity, and this was confirmed by an examination of the data.

The high-multiplicity bias was corrected by estimating the likelihood of overflow as a function of multiplicity and compensating the observed data for the estimated numbers of events with overflows. The first step in determining the overflow probability was to study the distribution of the number of wires firing per hit in each plane. This probability distribution is shown in Fig. VI-16a. It was determined from tracks satisfying the origin constraint and did not include hits not associated with accepted tracks.

If n_i is the number of wires firing for the ith track in a given plane, the probability of obtaining the value n_i, which is shown in Fig. VI-16a, can be represented by $P(n_i)$. The probability for obtaining a given configuration, where the first track hits n_1 wires, the second hits n_2 wires, etc., is given by

$$\prod_{i=1}^{n} P(n_i) \ ,$$

where n is the number of tracks. The probability that an overflow will occur is the sum over all these configurations such that more than 15 wires are hit. This probability that an overflow will occur for an n-prong event is therefore given by

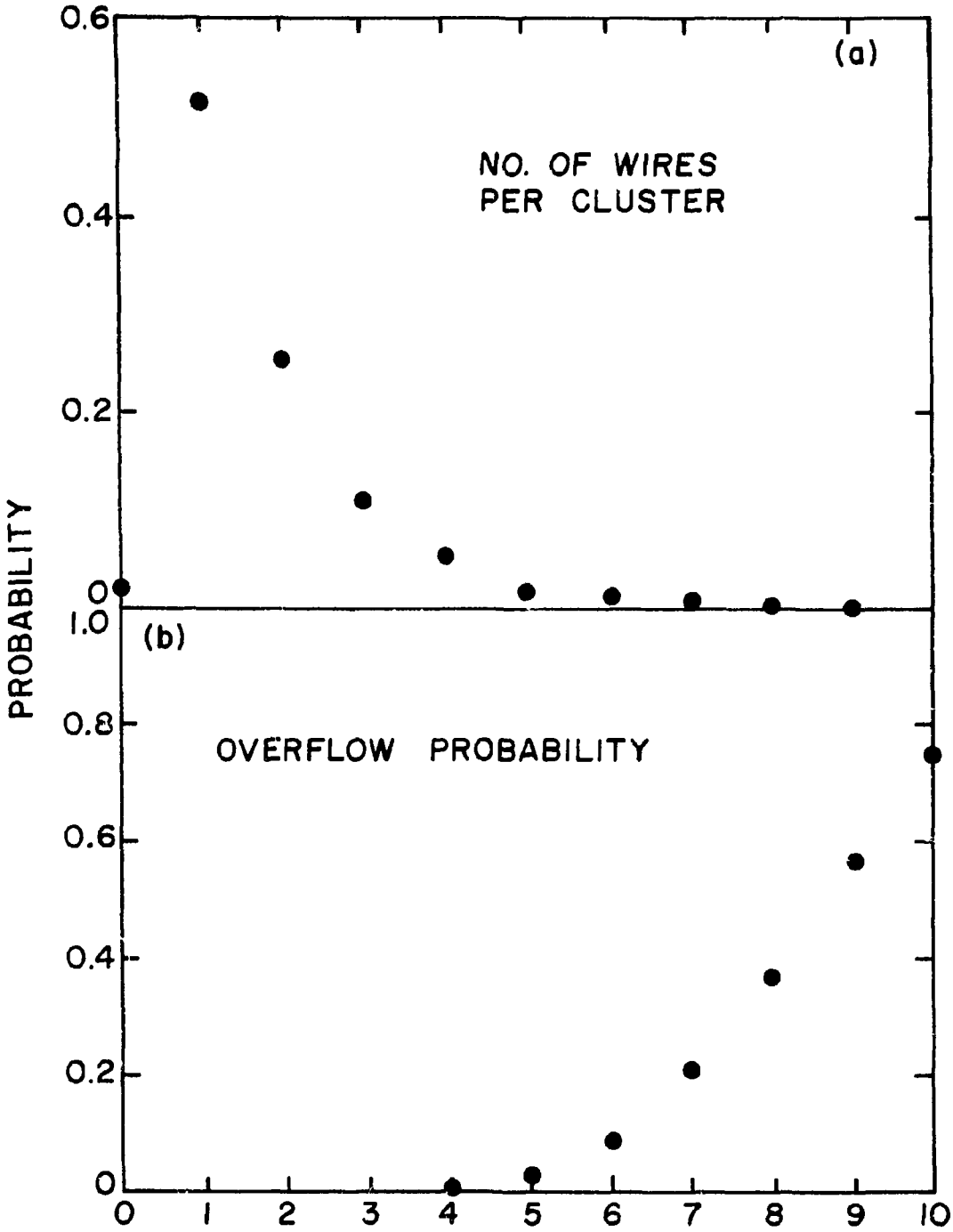

FIGURE VI-16. (a) The probability that a given hit in a polymeter plane will fire n wires, where n is the number shown on the abscissa. (b) The probability P_n that an n-prong event will contain an overflow in a given polymeter plane. The abscissa represents the charged multiplicity.

$$P_n = \sum_{k=16}^{\infty} \prod_{i=1}^{n} P(n_i), \qquad k \equiv \sum_{j=1}^{n} n_j .$$

Thus, if N_n^o is the observed number of events having charged multiplicity n, the corrected number of events is

$$N_n = N_n^o/(1 - 3P_n^2 + 2P_n^3),$$

where the polynomial in P_n accounts for the different overflow combinations among the three planes. The values of P_n were calculated by performing the products and sums indicated, over all possible combinations, using a computer. The values of the single-plane overflow probability are shown in Fig. VI-16b.

In order to effect the corrections to the observed multiplicity distributions, a computerized trial-and-error procedure was used. An assumed "physical" multiplicity was input for a given sample of events. The program then calculated the expected observed distribution based on the probability that tracks would be lost and that photons would convert. In addition to the guess for the physical multiplicity distribution, the average number of gammas for each multiplicity also had to be supplied as input. Then the physical multiplicity distribution and the numbers of gammas were changed successively until a good fit to the observed data was obtained.

The observed and corrected charged multiplicity distributions are shown in Figs. VI-17, 18 for the 4.8 and 3.8 GeV data respectively, for various values of the momentum of the particle observed in the spectrometer. The corrections to the observed distributions were applied separately to the data in each momentum bin, so that the

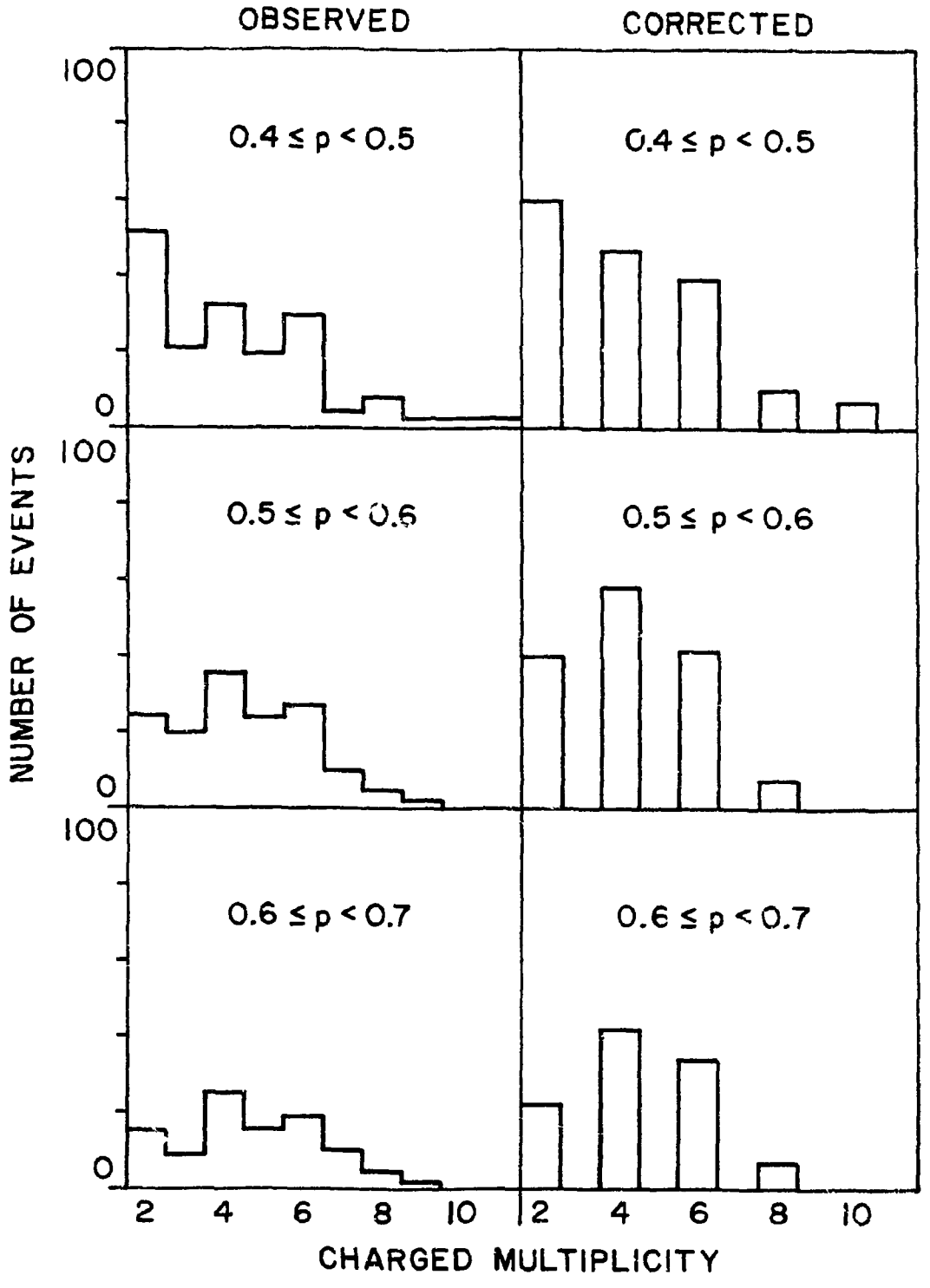

FIGURE VI-17a. The observed and corrected multiplicity distributions in various momentum intervals at a total center of mass energy of 4.8 GeV.

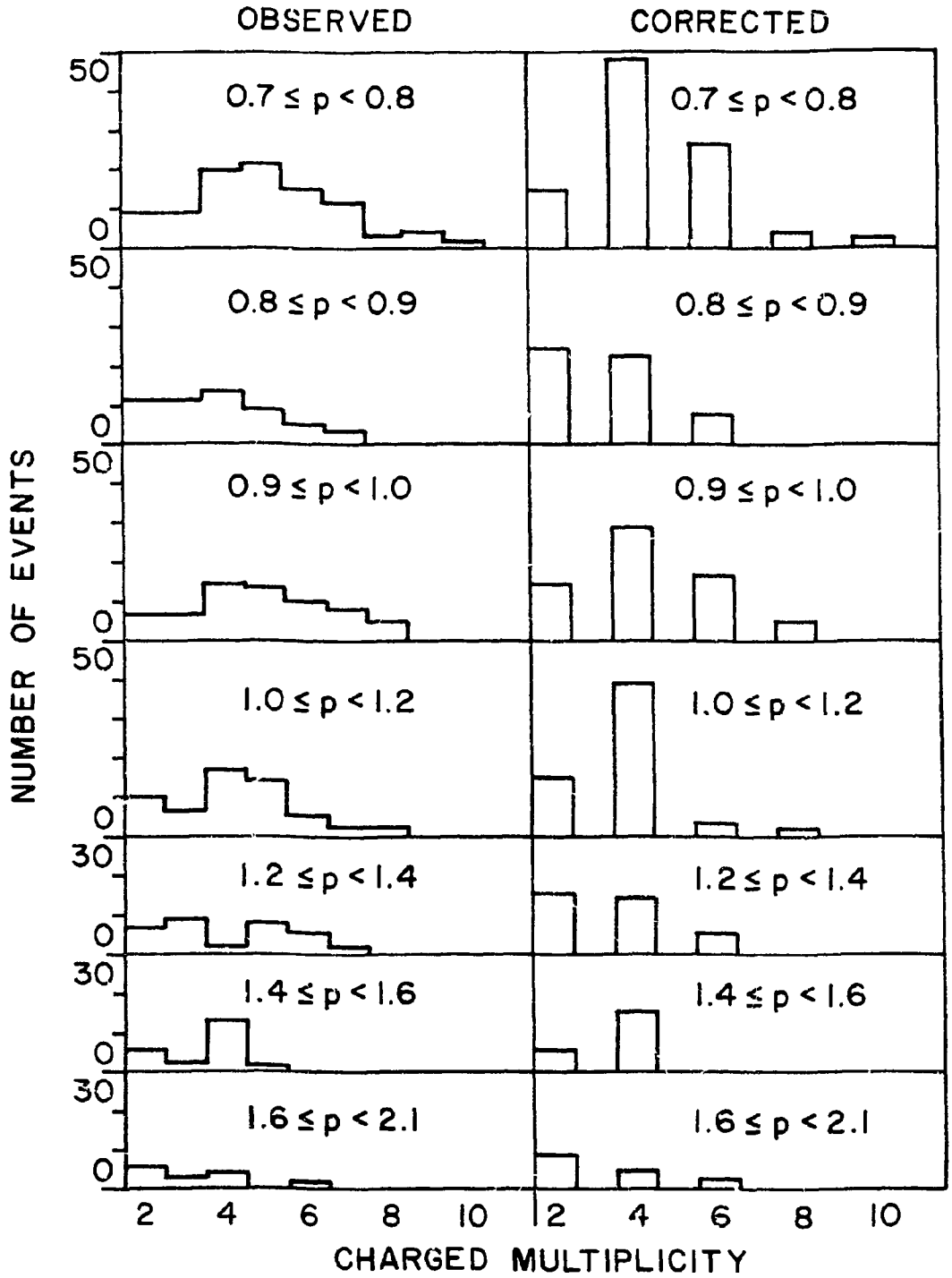

FIGURE VI-17b. The observed and corrected multiplicity distributions in various momentum intervals at a total center of mass energy of 4.8 GeV.

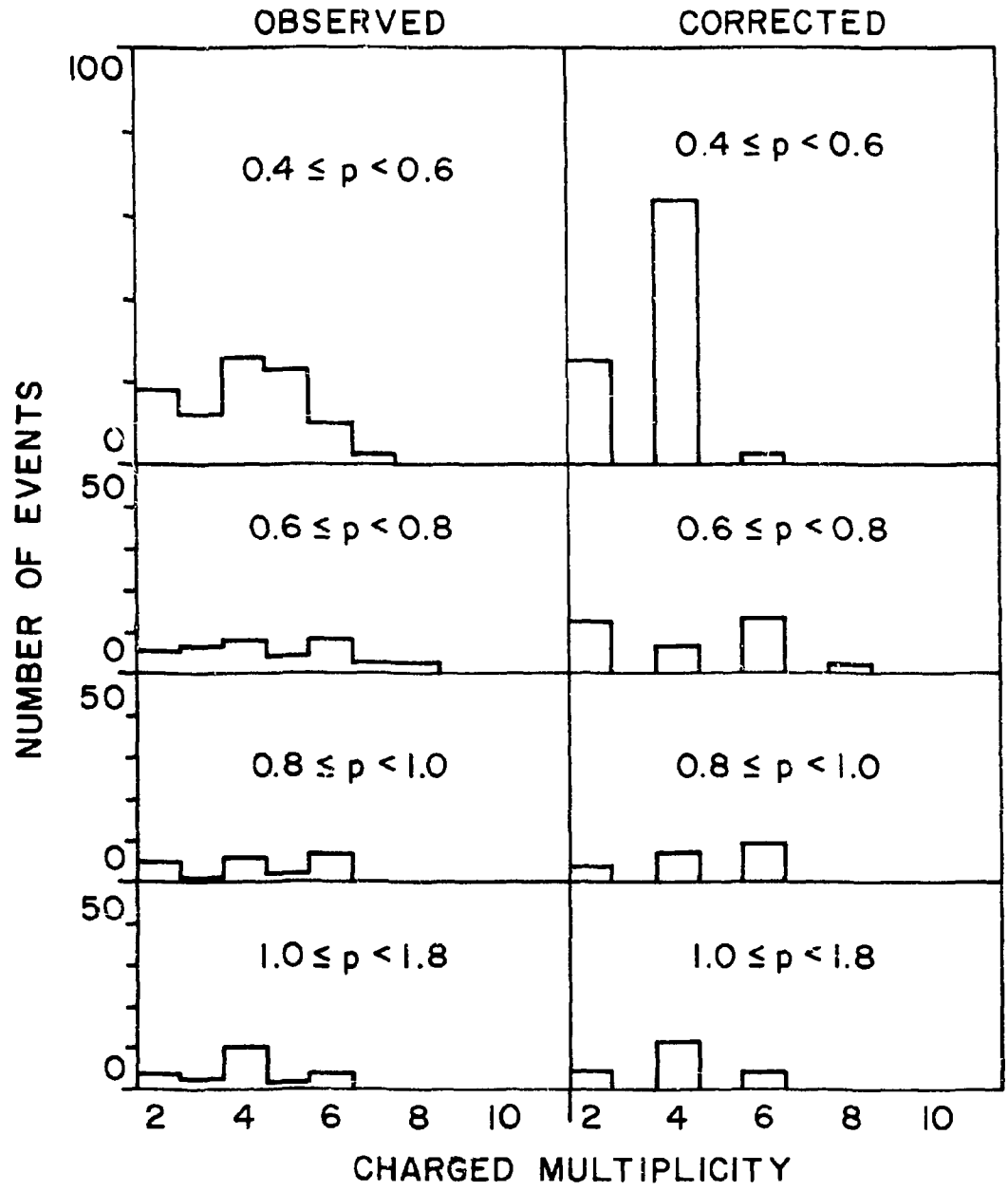

FIGURE VI-18. The observed and corrected multiplicity distributions in various momentum intervals at a total center of mass energy of 3.8 GeV.

corrections to any given bin were not influenced by the corrections to other bins.

The mean charged multiplicity is shown as a function of the spectrometer particle momentum in Figs. VI-19, 20 for the 4.8 and 3.8 GeV data. The form of the averaging procedure used to obtain the mean multiplicity was chosen with the object of eliminating the hadron multiplicity bias in the observed inclusive distributions. For example, a four-pronged event was twice as likely to trip the one-particle trigger as a two-pronged event, since the trigger could fire on any of the tracks failing within the spectrometer acceptance. The mean multiplicity was determined according to

$$\langle n_{ch} \rangle = \frac{\sum_m N_m}{\sum_m N_m/m} \quad ,$$

where m takes on the values of the even numbered multiplicities and N_m is the number of events observed having multiplicity m.

The straight line in Fig. VI-19 is represented by

$$\langle n_{ch} \rangle = 4.51 - 1.04\ p$$

and was fit to the data with $p > 0.9$ GeV/c. This same line is drawn through the 3.8 GeV data of Fig. VI-20 for comparison. The dashed line in Fig. VI-19 was determined from the charged multiplicity distributions in pp and $\pi^- p$ interactions[16] as a function of the available energy, defined by

$$E_a = \sqrt{s} - (M_a + M_b) \quad ,$$

where M_a and M_b are the masses of the particles in the initial state. A good fit to this data is given by

$$\langle n_{ch} \rangle = 2.45 + 0.32 \ln E_a + 0.53 \ln^2 E_a \qquad (pp, \pi^- p).$$

In order to compare this with the e^+e^- data, the "available energy" of the system recoilling against the spectrometer particle was approximated by

$$E_a = M_x - m_\pi \simeq \sqrt{W(W - 2p)} - m_\pi , \qquad (e^+e^-)$$

where M_x is the invariant mass of the recoilling system, $W = \sqrt{s}$ is the total CM energy, and p is the momentum of the spectrometer particle. Substituting this value of E_a, corresponding to a given value of the spectrometer particle momentum, the equivalent $\langle n_{ch} \rangle$ for $\pi^- p$ and pp interactions was calculated. Then $\langle n_{ch} \rangle + 1$ was plotted as the dashed line in Fig. VI-19. The extra unit was added to account for the charged spectrometer particle which was excluded from the calculations for the recoilling system.

It can be seen from Fig. VI-19 that the charged multiplicity for pp and $\pi^- p$ interactions exceeds that of e^+e^- interactions for all values of the inclusive particle momentum. For $p > 1.0$ GeV/c, the e^+e^- events average about 1.4 fewer charged particles per event, although the inclusive particle momentum dependences appear very similar. One might conjecture that the differences between the two multiplicity distributions is due to the presence of jet structure in the e^+e^- data. Strong evidence for jets has been found by the SLAC-LBL collaboration at higher CM energies[11]. The effect of jet structure would be that, on the average, the spectrometer particle would be associated with one or more additional particles, so that the energy available to the system recoilling against the spectrometer particle would be less than that calculated above.

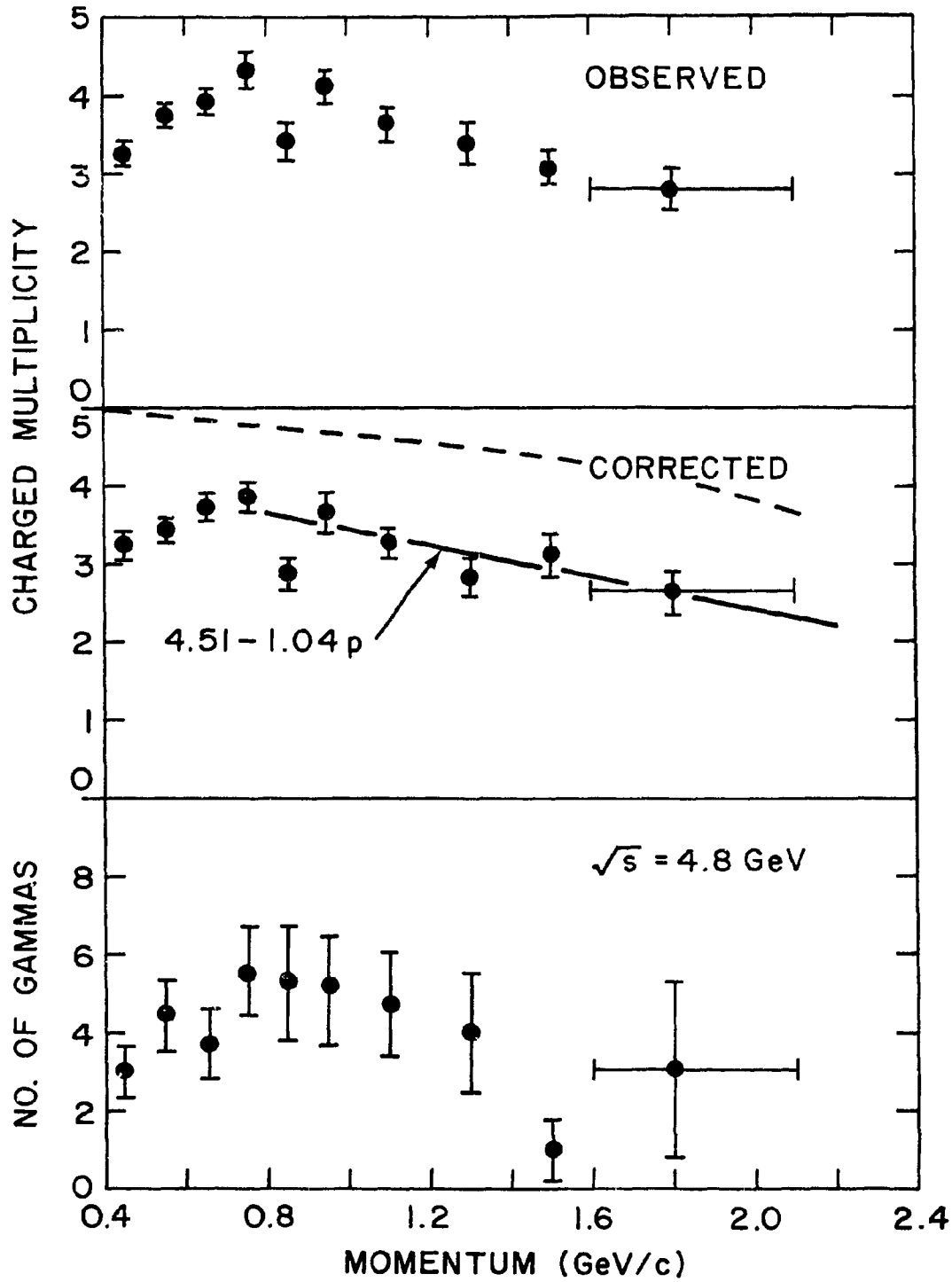

FIGURE VI-19. The mean charged multiplicity as a function of the inclusive hadron momentum at a total center of mass energy of 4.8 GeV. The lower plot shows the mean number of gammas per event needed to produce the observed distribution. The line drawn through the charged multiplicity data represents the best fit, for $p_{lab} \gtrsim 0.9$ GeV/c. The dashed curve was calculated from pp and $\pi^- p$ results.

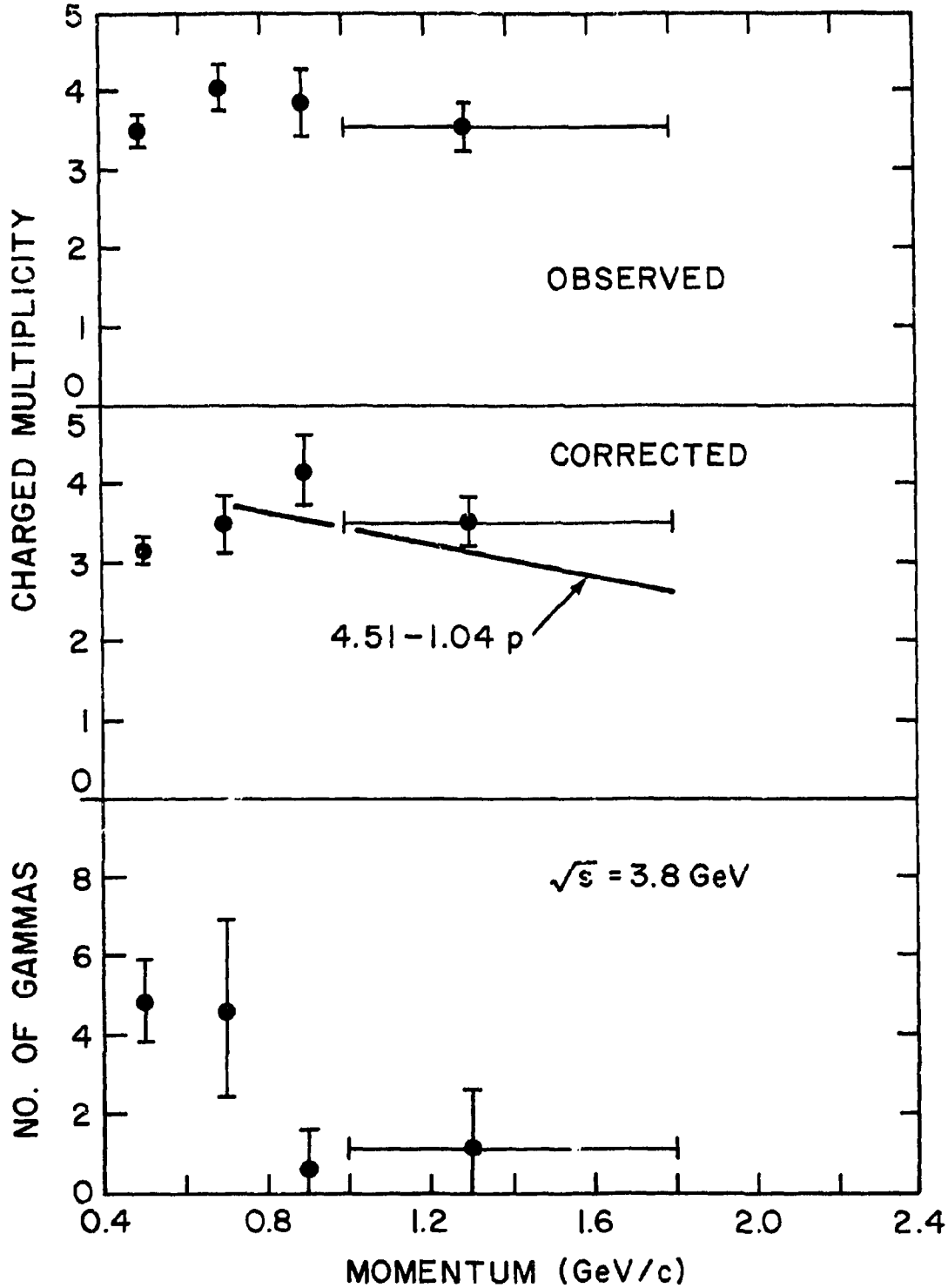

FIGURE VI-20. The mean charged multiplicity as a function of the inclusive hadron momentum at a total center of mass energy of 3.8 GeV. The lower plot shows the mean number of gammas per event needed to reproduce the observed distribution. The line drawn through the charged multiplicity data represents the best fit obtained for the 4.8 GeV data with $p > 0.9$ GeV/c.

As can be seen from Fig. VI-17b, the low point originated in the observed distribution. It is four standard deviations from the curve, making it rather unlikely to be entirely due to statistical fluctuations. Comparing the 0.85 bin of Fig. VI-17b with those adjacent to it suggests a relative enhancement for $n_{ch} = 2$.

The bottom portion of Fig. VI-19 represents the distribution of the mean number of gammas assumed to have been produced in each momentum bin in order to account for the contents of the odd-numbered multiplicity bins in the observed multiplicity data. The precision limits were determined by the statistical fluctuations in the numbers of gammas expected to convert in the polymeter.

The corrected average charged multiplicity for all the observed data was 3.29 ± 0.06 at 4.8 GeV and 3.39 ± 0.12 at 3.8 GeV. These values are not directly comparable to the SLAC-LBL total charged multiplicity values. One reason is that about 50% of the hadrons are produced with momenta below the 0.4 GeV/c SP8 cutoff. The SLAC-LBL apparatus was also insensitive to the production of coplanar hadron and muon pairs, described below, which substantially reduced the average low-momentum multiplicity. If one assumed that all the photons resulted from neutral pion decay, then a rough estimate of the average numbers of neutral pions would have been 2.2 ± 0.2 at 4.8 GeV and 2.1 ± 0.4 at 3.8 GeV.

The behavior of each charged multiplicity class as a function of the spectrometer particle momentum is shown for the 4.8 GeV data in Fig. VI-21. These cross sections were obtained by multiplying the fraction of events with a given multiplicity value by the differential inclusive cross section shown in Fig. VI-7, summed over particle types.

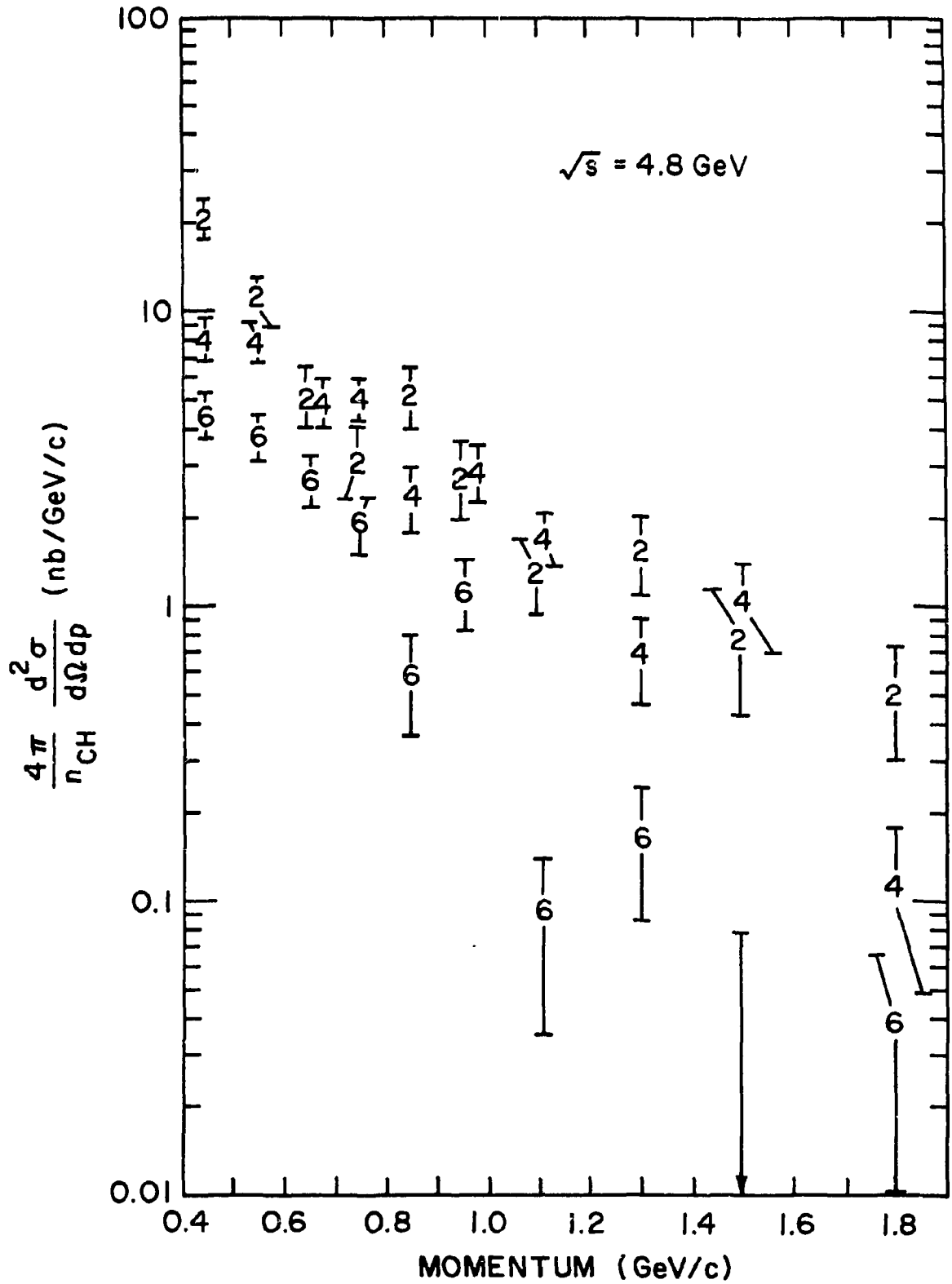

FIGURE VI-21. The hadron production cross sections broken down according to charged multiplicity. The points plotted represent the fraction of the inclusive hadron cross section having the given multiplicity, divided by the multiplicity. The errors are statistical only.

The resulting inclusive cross sections were divided by the value of the multiplicity in order to eliminate the bias in the one-particle inclusive trigger and obtain the production cross sections. The errors shown in Fig. VI-21 are statistical only.

Figure VI-21 suggests that the production rates of two- and four-prong events were of similar magnitudes over most of the momentum spectrum. The number of multiplicity two events is seen to rise rapidly at the lowest momenta measured. A possible explanation for this is that a relatively large contribution of the low-momentum two-pronged events may have resulted from the two-photon production process. Calculations[17,18] for this process indicate that when two charged pions are produced in this manner,

$$e^+e^- \rightarrow e^+e^-\gamma\gamma \rightarrow e^+e^-\pi^+\pi^-$$

$$(\text{or} \rightarrow e^+e^-\mu^+\mu^-)$$

the pions (muons) tend to come out coplanar. An examination of the two-pronged hadrons where the spectrometer particle had $0.4 < p < 0.5$ GeV/c showed that 43% ± 11% were coplanar within 10^o, and that 24% ± 8% were coplanar within 3^o. Because these events had momenta well below the muon detection threshold, they could equally well have been pions or muons.

The production rate of six-prong events appears to have been about half that of two- and four-prong events at low momentum, but dropped sharply around 1.0 GeV/c. A similar drop in four-prong events seems to have occurred before the highest momentum bin, for $p \simeq 1.6$ GeV/c. No cross sections were calculated for multiplicities higher than six, due to the small numbers of these events.

The production cross sections for n_{ch} = 2, 4, and 6 events are shown separately in Figs. VI-22, 23 and 24, along with the 3-parameter best fits for each. The goodnesses of the fits are shown in the following table:

n_{ch}:	2	4	6
χ^2 for 7 degrees of freedom:	10.3	8.6	15.6
Confidence level:	0.16	0.28	0.03

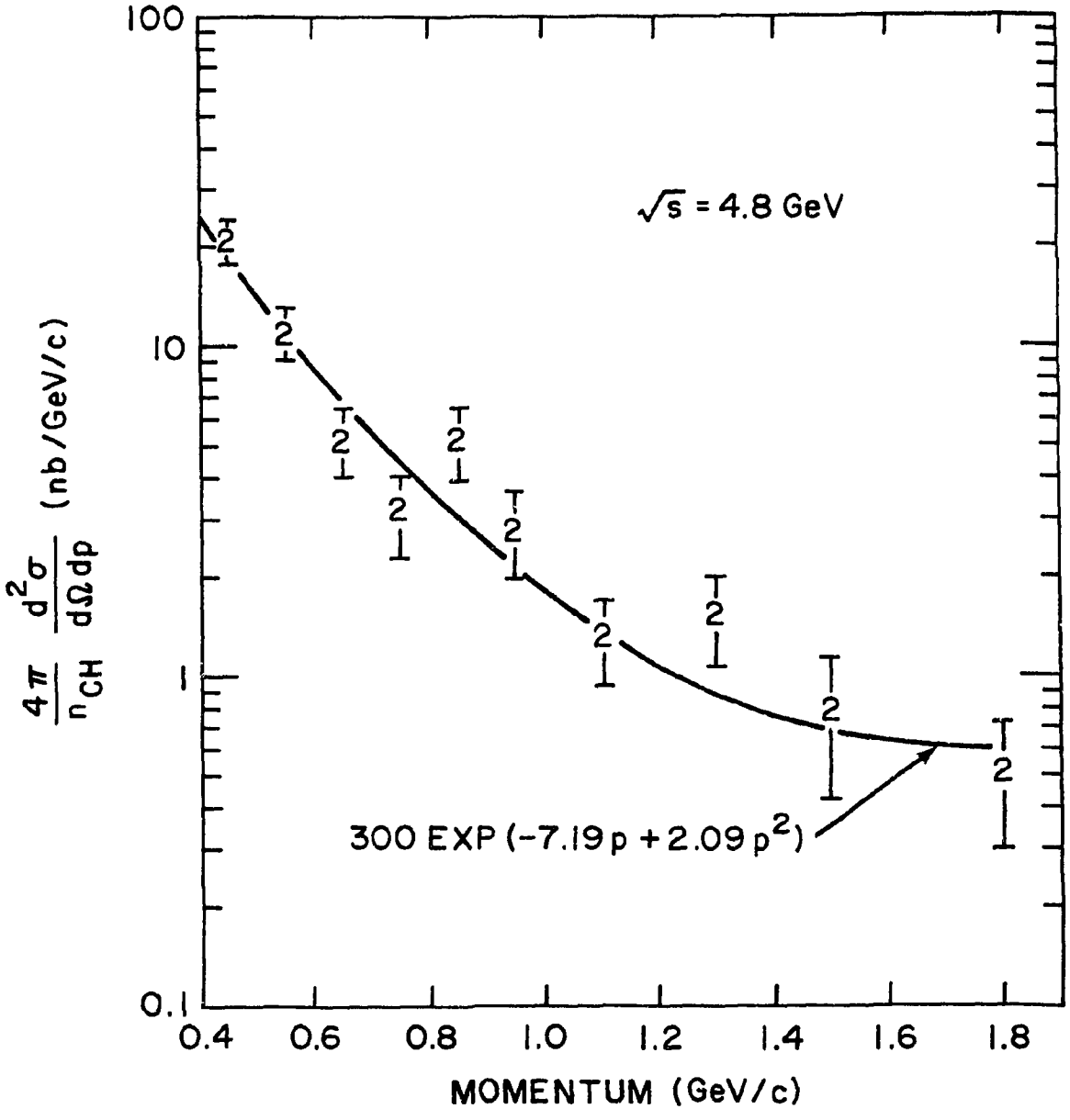

FIGURE VI-22. The production cross section for hadrons with two charged tracks. The fit to the solid curve had a chi square of 10.3 for seven degrees of freedom. The errors are statistical only.

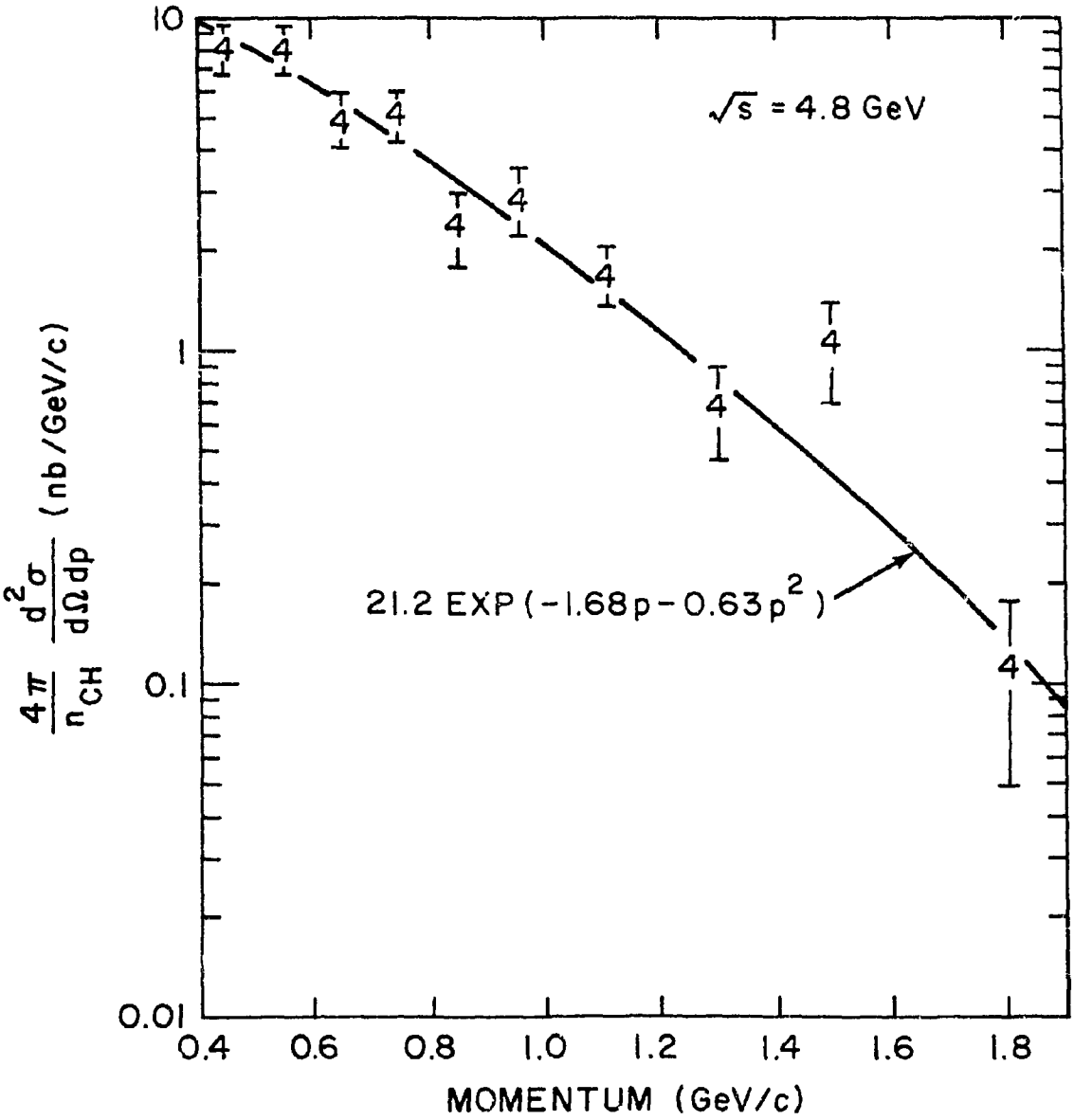

FIGURE VI-23. The production cross section for hadrons with four charged tracks. The fit to the solid curve had a chi square of 8.6 for seven degrees of freedom. The errors are statistical only.

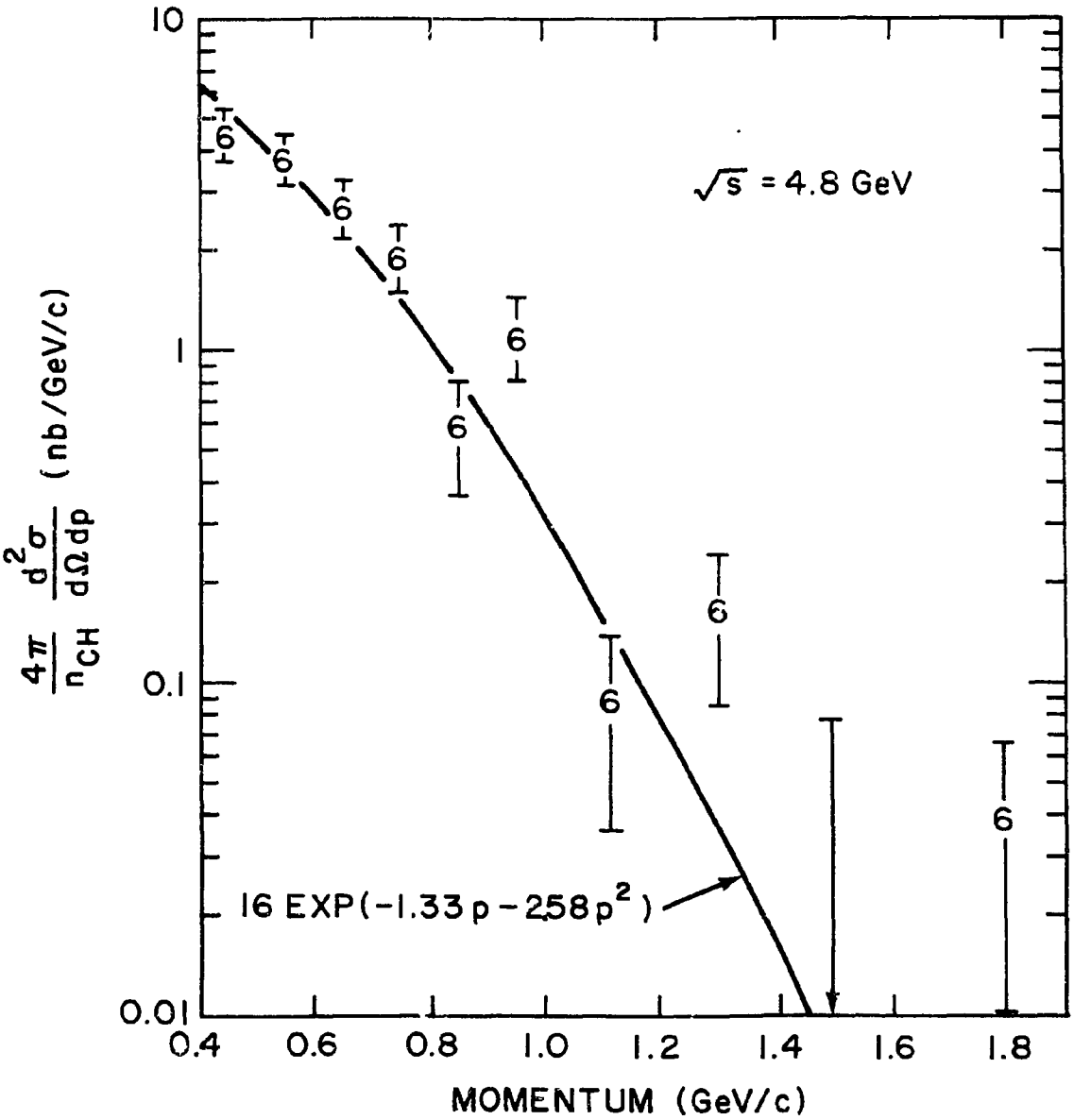

FIGURE VI-24. The production cross section for hadrons with six charged tracks. The fit to the solid curve had a chi square of 15.6 for seven degrees of freedom. The errors are statistical only.

REFERENCES

CHAPTER VI

1. T. L. Atwood, et al., Phys. Rev. Lett. 35, 704 (1975).
2. E. Bracci, J. P. Droulez, E. Flaminio, J. D. Hansen, and D. R. O. Morrison, CERN/High-Energy Reactions Analysis Group #72-1 (1972).
3. E. Bracci, J. P. Droulez, E. Flaminio, J. D. Hansen, and D. R. O. Morrison, CERN/High-Energy Reactions Analysis Group #72-2 (1972).
4. U. Casadei, G. Giacomelli, P. Lugaresi-Serra, G. Mandrioli, A. M. Rossi and F. Viaggi, CERN/High-Energy Reactions Analysis Group #75-1 (1975).
5. J. W. Cronin, R. Cool, and A. Abashian, Phys. Rev. 107, 1121 (1957).
6. H. Ogren, Laboratori Nazionali di Frascati del CNEN (Italy) report # LNF-71/89 (1971).
7. C. C. Morehouse, Proceedings of Summer Institute on Particle Physics, SLAC Report No. 191, p. 247, (1975).
8. J.-E. Augustin, et al., Phys. Rev. Lett. 34, 233 (1975) and Phys. Rev. Lett. 34, 764 (1975).
9. G. J. Feldman and M. L. Perl, Stanford Linear Accelerator Center Report No. SLAC-PUB-1615 (1975), to be published in Phys. Reports.
10. B. Richter, proceedings of XVII International Conference on High Energy Physics, London, 1974.
11. R. F. Schwitters, Proceedings of the 1975 International Symposium on Lepton and Photon Interactions at High Energies, Stanford, Calif. (1975).
12. R. P. Feynman, Phys. Rev. Lett. 23, 1415 (1969).

13. M. L. Perl, High Energy Hadron Physics (Wiley, New York, 1974), Chapter 8.

14. J. D. Bjorken, Phys. Rev. 179, 1547 (1969).

15. B. Wiik, Proceedings of the 1975 International Symposium on Lepton and Photon Interactions at High Energies, Stanford, Calif. (1975).

16. J. Whitmore, Phys. Reports 10C, 274 (1974).

17. H. Terazawa, Rev. Mod. Phys. 45, 615 (1973).

18. G. Grammer, Jr. and T. Kinoshita, Nucl. Phys. B80, 461 (1974).

CHAPTER VII

ANOMALOUS MUON PRODUCTION

A. Introduction

Up to this point, nothing has been said about inclusive muon data, except that collinear muon pairs were tabulated and the results used to normalize the inclusive hadron cross sections. This normalization procedure was discussed in Chapter V and made use of the fact that the QED production process is well understood, and that the measured production of collinear lepton pairs agrees with QED predictions.

The present chapter will be concerned with the examination of that portion of the inclusive muon data which was not classified as collinear muon pairs. These events were divided into two classes according to the value of the charged multiplicity. Separate studies were made of the muon events with a charged multiplicity of 2 ($n_{ch} = 2$) and of events with charged multiplicity greater than 2 ($n_{ch} \geq 3$). The observed characteristics of these two sets of data are summarized in Section B.

The contributions were calculated to each of these two data samples arising from all known muon production processes. Section C describes each of these processes and their contributions to the $n_{ch} = 2$ events. In Section D the predicted production rate is compared with the data, with the result that a small signal is observed in excess of the predicted effects. Section E discusses a search for μ-e events, such as those seen by the SLAC-LBL collaboration.[9] The search for an anomalous signal in the multiprong

muon events is discussed in Section F, and the physical implications of the inclusive muon data are discussed in Section G.

The results presented in this chapter represent a further analysis of previously published[1] inclusive muon data, using the more advanced momentum analysis procedures described in Chapter III. The additional solid angle coverage resulted in the addition of two events to the 4.8 GeV sample. The more reliable polymeter track reconstruction procedures developed for the charged multiplicity analysis resulted in a change in the multiplicity assignments of three of the previously published events. With the addition of the new events, there were still 13 events with $n_{ch} = 2$, and the number of $n_{ch} \geq 3$ events increased from two to four.

A much more important change in the previous results came about with the realization that the output of the QED calculation program[2] for the differential coplanarity cross section for the process $e^+e^- \rightarrow \mu^+\mu^-\gamma$ had been misinterpreted. The correct interpretation required that the previous QED background be multiplied by an additional factor of 1.85, causing a considerable reduction in the significance of the previously published results. The correct calculation procedure for this background is described in Section C.

B. The Inclusive Muon Events

The identification procedure for muon events was described in Section IV-E. The inclusive muon events examined in the present chapter were selected by requiring that the spectrometer particle must have been tagged as a muon and that its momentum must have been

greater than about 1.05 GeV/c. This momentum limit resulted from the requirement that, to be tagged as a high-momentum muon, the particle had to fully penetrate all three slabs of the iron hadron filter. Thus, the specific range requirement depended on the angle of incidence of the particle trajectory upon the hadron filter.

The presence of a second hadron filter on the side of the beam opposite the spectrometer allowed the tagging of high-momentum muons there as well, although their momenta were not measured. No trigger requirements were ever imposed on any conjugate-side particles. If for a given event a second such high-momentum muon was observed, then that event was designated a "$\mu\mu$" event. If a second prong, occurring in the conjugate side or in the polymeter apparatus, did not penetrate the hadron filter, the event was designated a "μx" event. These designations were applied only to the events with $n_{ch} = 2$, but the same information was available for the higher multiplicity events.

Of particular interest for the two-prong events were the relative angles at which the two particles were observed. The "collinearity" angle was the angle between the two final state muon trajectories as they left the interaction region. The convention used was the usual one that, if the two particles emerged exactly antiparallel, the collinearity angle was zero. The angle ranged from zero to 180°, at which angle the particles would emerge in exactly the same direction. The diagram in Fig. VII-1a shows how the collinearity angle was defined. As is clear from the figure, measuring the collinearity of two tracks required that both be reconstructed in three dimensions. While the azimuthal angle of almost every track

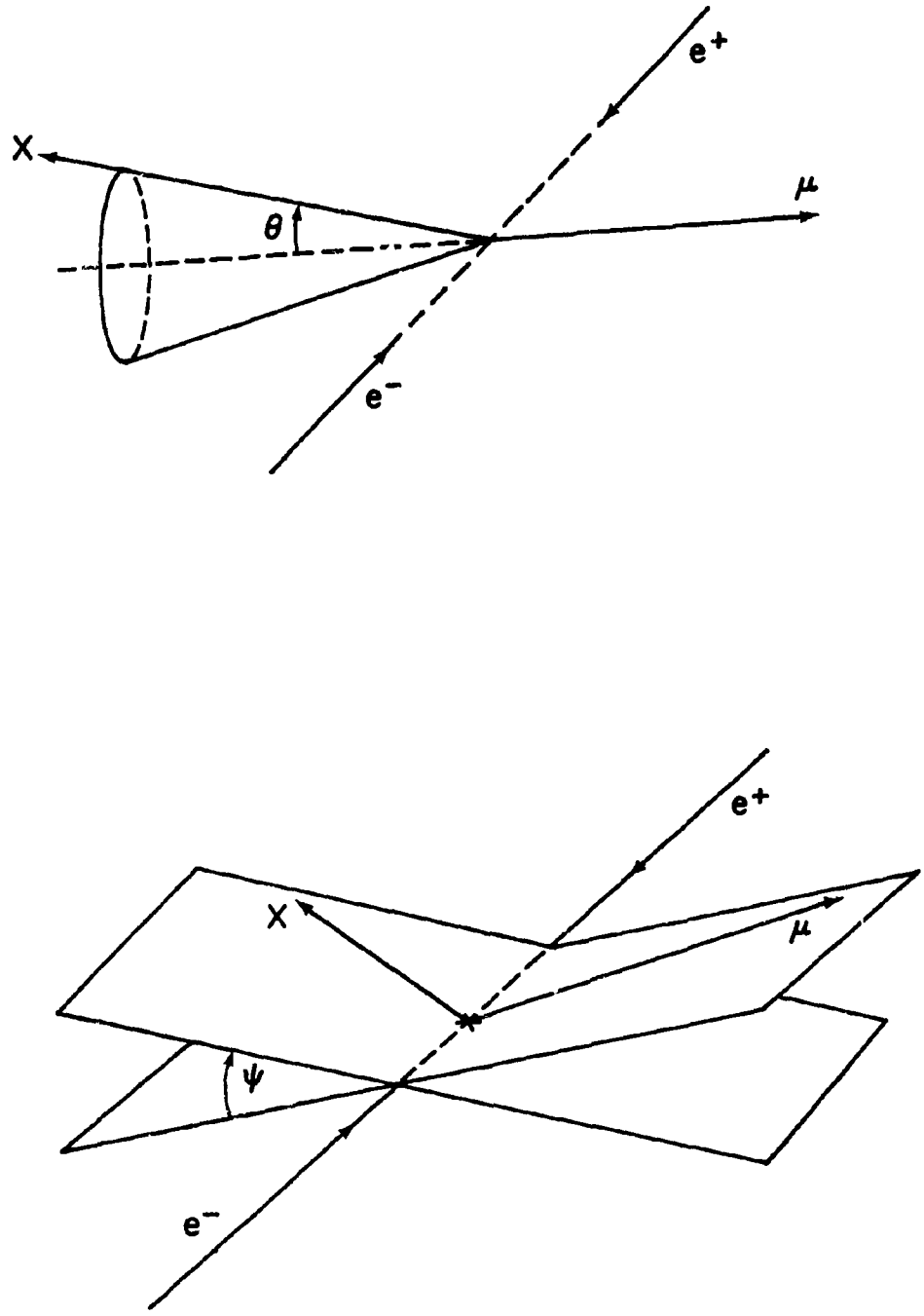

FIGURE VII-1. (a) The definition of the collinearity angle θ. (b) The definition of the coplanarity angle ψ. Each plane is defined to contain the beam and one of the outgoing tracks.

could be measured by the polymeter, the polar angle (relative to the beam) for a particle outside the spectrometer could be reconstructed only if the particle passed through one of the "X" chambers located in the spectrometer or opposite to it. The size of the collinearity which could be measured was thus limited by the spatial extent of these chambers. Every two-prong event having a collinearity less than about 30° could have it measured, and some events could have measureable collinearity angles as large as 60°, depending on the specific positions and directions of the two emerging particles.

The polymeter measured the azimuthal angle (relative to the beam) of every recognized track. Thus, for every event, one could compare the projected angular differences of various track pairs as reconstructed in the polymeter. Since the polymeter wires all ran parallel to the beams, they measured the direction of tracks projected onto a plane perpendicular to the beams. As shown in Fig. VII-1b, the spectrometer particle trajectory intersected with the beam line to form a reference plane containing both lines. A "coplanarity" angle was defined for the second final state particle as the projected angle at which it intersected this reference plane.

The QED process is known[3] to produce a very large number of muon pairs at small collinearity and coplanarity angles, as shown, for example, in Fig. V-2. Since these large numbers of events would obscure any unknown muon production process which might have been present, the study of two-prong muons was restricted to those events having coplanarity angles greater than 20°. A tabulation of all such events is presented in Table VII-1, which gives the momentum and coplanarity for each two-prong event.

TABLE VII-1. Summary of inclusive muon events with $n_{ch} = 2$, non-coplanarity > 20^{o}, and momentum greater than 1.05 GeV/c.

a) $\sqrt{s}$ = 4.8 GeV.

No.	Momentum (GeV/c)	ID	Coplanarity (Deg.)	Collinearity (Deg.)
1	1.81	μx	104.3	
2	1.79	μx	117.5	
3	1.77	μx(γ)	24.6	
4	1.41	μx	156.3	
5	1.40	μμ	27.2	37.6
6	1.27	μx	42.5	
7	1.25	μx	22.1	
8	1.23	μx	98.8	
9	1.22	μx	74.2	
10	1.17	μx	20.9	
11	1.09	μx	42.4	
12	1.07	μμ	23.1	25.4
13	1.07	μμ	32.5	

b) $\sqrt{s}$ = 3.8 GeV.

No.	Momentum (GeV/c)	ID	Coplanarity (Deg.)	Collinearity (Deg.)
1	1.78	μx	28.8	37.9
2	1.42	μx	44.1	
3	1.38	μx	102.8	

TABLE VII-2. Summary of inclusive muon events with $n_{ch} \geq 3$ and momentum greater than 1.05 GeV/c. The μμ coplanarity and collinearity are given for events where a second muon was tagged opposite the spectrometer.

a) $\sqrt{s}$ = 4.8 GeV.

No.	Momentum (GeV/c)	Multiplicity	Copl. (Deg.)	Collin. (Deg.)
1	1.92	3	4.9	40.5
2	1.45	3-4		
3	1.25	4		
4	1.24	4		

b) $\sqrt{s}$ = 3.8 GeV.

No.	Momentum (GeV/c)	Multiplicity	Copl. (Deg.)	Collin. (Deg.)
1	1.85	4	0.8	1.0
2	1.62	3	5.4	9.6
3	1.57	4	7.6	9.1
4	1.55	4	6.9	7.4
5	1.21	5		

Table VII-2 presents a tabulation of all the muon events with $n_{ch} \geq 3$. Some of these events had the property that the various reconstructed tracks included a second high-momentum muon in the conjugate-side apparatus. For these events, the coplanarity and collinearity were given for the two muon tracks.

C. Production Processes for Muon Events with $n_{ch} = 2$

1. Radiative QED Processes

The dominant process producing two-prong muon events can be described in lowest order by the usual one-photon exchange process

$$e^+e^- \rightarrow \mu^+\mu^- .$$

However, a characteristic of this process is that the muons are collinear. A 20° coplanarity cut would exclude effects from this simple process.

On the other hand, there are a number of effects of order α^3, involving real or virtual photons, which could produce noncollinear muon pairs. A computerized numerical calculation was carried out by F. A. Berends, K. J. F. Gaemers, and R. Gastman[2] to determine the cross section for muon pair production to order α^3. A version of this program was specially adapted for the SP8 collaboration by Dr. K. J. F. Gaemers. The program performed integrations over the experimental angular acceptances and produced the observed cross section as a function of the coplanarity angle. The contributing Feynman diagrams for the processes considered are given in Fig. VII-2.

The calculations were performed for a specific experimental arrangement. The muon in the spectrometer was required to have a minimum energy of 1.05 GeV and to be within a polar angle of $\pm 13.5^\circ$

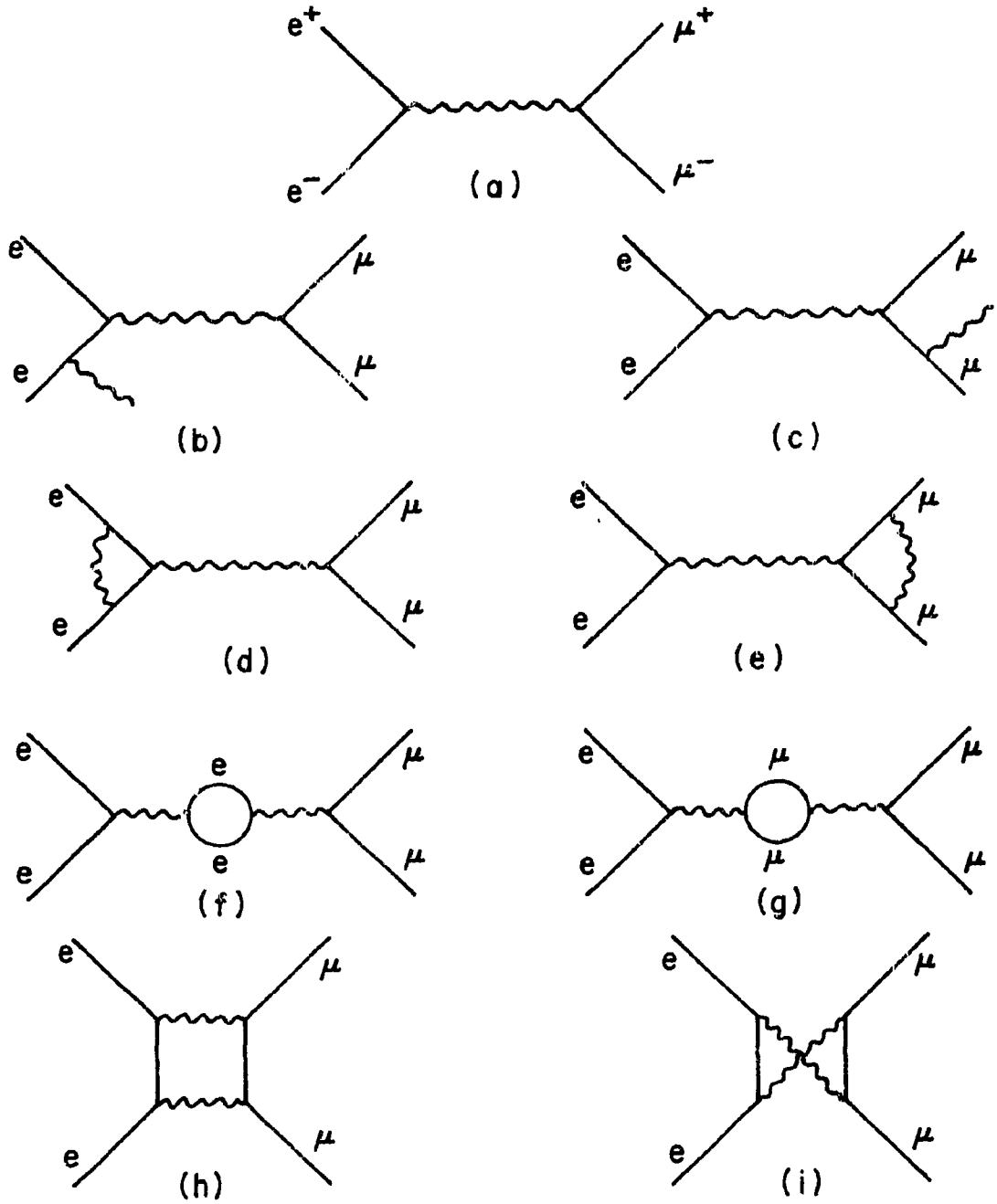

FIGURE VII-2. (a) The Feynman diagram for the lowest order QED process $e^+e^- \to \mu^+\mu^-$. (b-i) Other diagrams included in the calculation of the differential cross section to order α^3.

centered at 90^{o} from the beam. The second muon was required to have the minimum energy of 115 MeV, which was necessary for it to penetrate the polymeter. Its polar angle ranged from 11^{o} to 169^{o}, corresponding to the polar acceptance of the polymeter.

The output of the numerical integration procedure was a cross section $d\sigma/d\psi$, differential in the coplanarity angle ψ. The results were defined such that this angle ranged from 0 to π. Two adjustments were made to the resultant cross section values to make them compatible with the SP8 apparatus: (1) No azimuthal angle limits were mentioned in the previous paragraph because the program integrated over the full 2π azimuthal angle. Since the "second" muon track in the polymeter could range over the full 2π, only the azimuthal acceptance of the spectrometer needed to be corrected for. This involved a multiplicative factor of $13.4^{o}/360^{o}$. (2) The output of the integration was a production cross section. Since the SP8 apparatus used a one-particle inclusive trigger, the calculated cross section was multiplied by a factor of 2 to account for the possibility of triggering on either of the muons associated with an event. Strictly speaking, this factor should not be precisely 2, since there was no guarantee that the second muon was above the 1.05 GeV/c momentum threshold. About 15% of the calculated cross section involved events where the untagged muon was below this threshold. Thus, the correct factor was 1.85.

The total number of muon pairs expected with one muon having a momentum greater than 1.05 GeV/c and with a coplanarity angle greater than 20^{o} was found to be 5.5 events at 4.8 GeV and 2.0 events at 3.8 GeV. The QED background distribution at 4.8 GeV is shown

superimposed on the observed events in Fig. VII-3.

The amplitudes from higher-order QED processes such as

$$ee \rightarrow \mu\mu\gamma\gamma$$

have been estimated to be negative and small, such that its inclusion would reduce the $ee \rightarrow \mu\mu\gamma$ cross section by 5% - 10%[4].

2. Hadron Misidentification

Another contribution to "muon" events was the process of hadron misidentification. In order to be tagged as a high-momentum muon, a particle in the spectrometer had to penetrate the hadron filter, have a Cerenkov signal above pedestal and have a normalized shower detector amplitude less than 3.0 on the scale shown in Fig. IV-4. An occasional hadron could exhibit such a signature by (1) decaying into a high-momentum muon or by (2) punching through the hadron filter.

The probability that a hadron would penetrate the hadron filter depended on two factors. The hadron had to survive the absorption processes resulting from nuclear interactions and it had to have sufficient range. Both of these processes were calculable as described in Section IV-D. The range and, to a smaller extent, the nuclear absorption were dependent on the momentum of the hadron incident on the hadron filter. The angle of incidence of the hadron also had to be taken into account, since it determined the amount of iron that had to be penetrated for a given event.

Contributions from kaons and protons to this punchthrough process were negligible. This resulted from their much shorter range and from the absence of a signal in the Cerenkov counter. Thus, the punchthrough contributions came only from high-momentum pions.

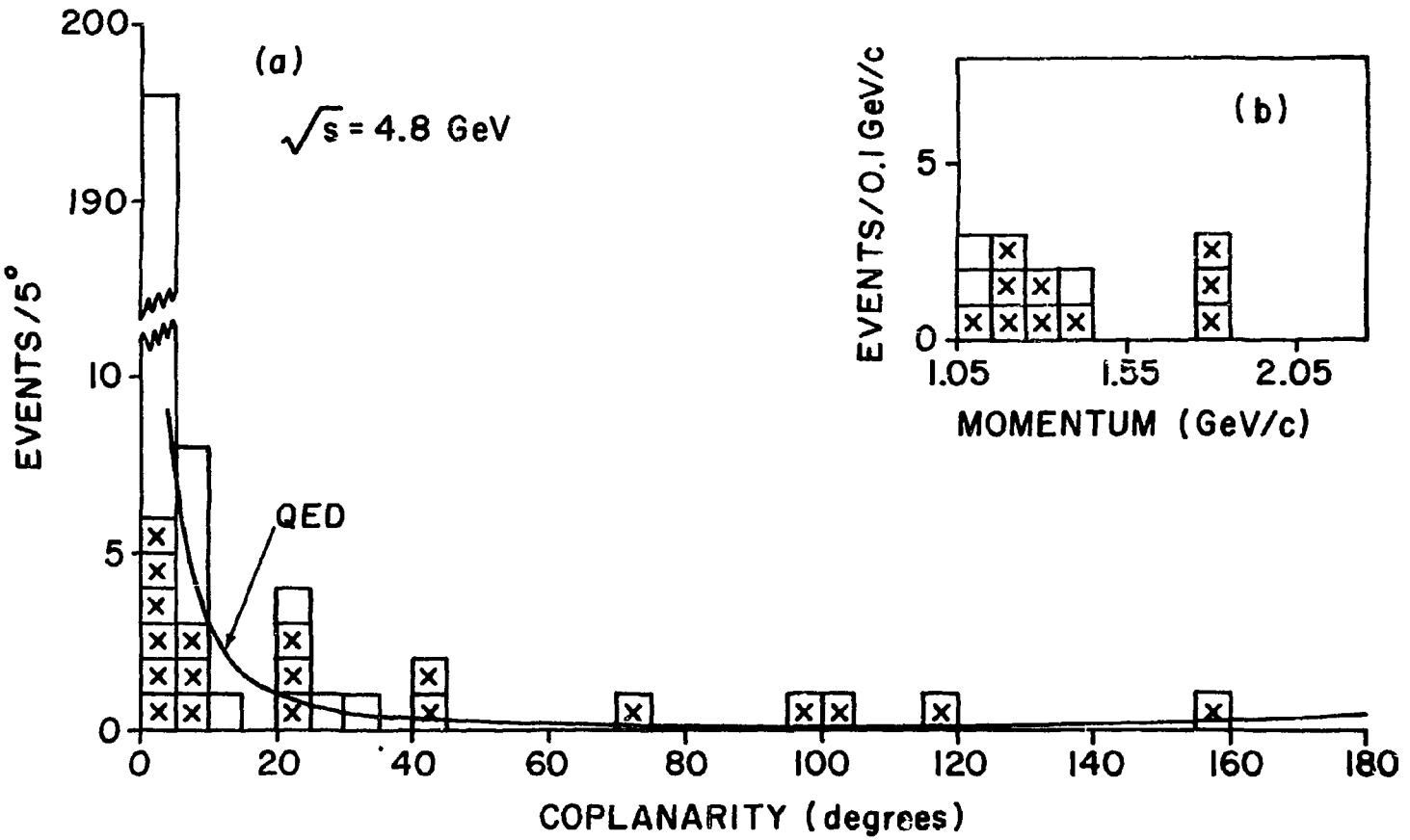

FIGURE VII-3. (a) Noncoplanarity distribution for two-prong events having at least one muon penetrating $\gtrsim$ 69 cm Fe. For events marked with an "x", the second prong was not identified as a high-momentum muon. The average angular resolution was $\pm 1^{\circ}$. The QED curve was calculated from Ref. 2. (b) Muon momentum distribution for events noncoplanar by more than 20°.

Using the equations of Section IV-D, the penetration probability was calculated for each observed pion event having a momentum greater than 1.05 GeV/c.

The probability that a pion or kaon would decay into a muon with sufficient range to penetrate the hadron filter is shown in Fig. VI-3 as a function of the momentum of the incident hadron. As described in Section VI-B-3, this probability was determined by calculating the fraction of the total solid angle in the hadron rest frame within which the secondary muon would be emitted with a lab momentum greater than 1.05 GeV/c. This decay-penetration probability was evaluated over the observed hadron events in order to obtain the estimated contribution to muons from this process.

The probability for misidentifying kaons as muons was substantially reduced by two additional characteristics of these particles. The large transverse momentum resulting from some kaon decays causes the secondary muon to miss a trigger chamber or fail the event reconstruction criteria. An even more important criterion for kaons was the requirement that the Cerenkov amplitude be above pedestal. This in effect required that the decay occur before or within the Cerenkov counter in order to be recognized as a muon. To account for these effects, a Monte Carlo program was used to estimate the probability that a kaon would decay early enough to have a Cerenkov signal and then be successfully reconstructed with the muon momentum sufficiently high to allow it to penetrate the hadron filter. These problems did not exist for the high-momentum pions, since they always had signals in the Cerenkov counter and decayed with relatively low transverse momenta.

The numerical results of the calculations of the numbers of muons resulting from hadron misidentification are given in Table VII-3. The punchthrough and decay contributions are listed separately. The errors quoted for these estimates result from the statistical uncertainties in the observed hadron events upon which the calculations were based. The total number of two-prong muon events noncoplanar by more than 20^{o} resulting from hadron misidentification was .93±.17 events at $\sqrt{s}$ = 4.8 GeV and .09±.03 events at $\sqrt{s}$ = 3.8 GeV.

3. The Two-Photon Process

Another process which can produce muons is the interaction of two virtual photons produced by the electron-positron collision[5]:

$$e^+e^- \rightarrow e^+e^-\gamma\gamma \rightarrow e^+e^-\mu^+\mu^- .$$

The relevant Feynman diagrams are given in Fig. VII-4. In this order of perturbation theory diagram (a) dominates. The other diagrams are smaller by at least a factor of $\ln(\sqrt{s}/2m_e)$. The principal characteristic of this process is that the virtual photons tend to be radiated along the beam, so that the muon secondaries are roughly coplanar. This is not always the case, however, and the contributions from diagram (a) of Fig. VII-4 to the sample of noncoplanar muon pairs was large enough to show up in the observed events.

The effective cross section for the SP8 geometry was calculated by G. Grammer and P. Lepage and was an extension of the exact calculation of Ref. 5 to include all t-channel amplitudes to fourth order. This calculation required that one muon have a momentum greater than 1.05 GeV/c and fall within the solid angle subtended by the spectrometer. The other muon was required to be within the

TABLE VII-3. Muon backgrounds with $P_\mu > 1.05$ GeV/c.

	$n_{ch} = 2$, Noncoplanarity $> 20^\circ$		$n_{ch} \geq 3$	
	3.8 GeV	4.8 GeV	3.8 GeV	4.8 GeV
Hadron Punchthrough	0.05 ± 0.02	0.39 ± 0.10	0.27 ± 0.09	1.09 ± 0.15
$\pi \to \mu\nu$	0.04 ± 0.02	0.52 ± 0.13	0.18 ± 0.06	1.77 ± 0.22
$K \to \mu\nu$	———	0.02 ± 0.02	———	0.14 ± 0.09
$e^+e^- \to \mu^+\mu^-\gamma$	2.0	5.5	———	———
$e^+e^- \to e^+e^-\mu^+\mu^-$	———	0.01	0.4	2.05
$e^+e^- \to \psi'\gamma$, $\psi' \to \psi$ + charged, $\psi \to \mu^+\mu^-$	———	———	0.80 ± 0.23	0.25 ± 0.07
Total Expected	2.1	6.4	1.7 ± 0.3	5.3 ± 0.3
Observed	3	13	5	4

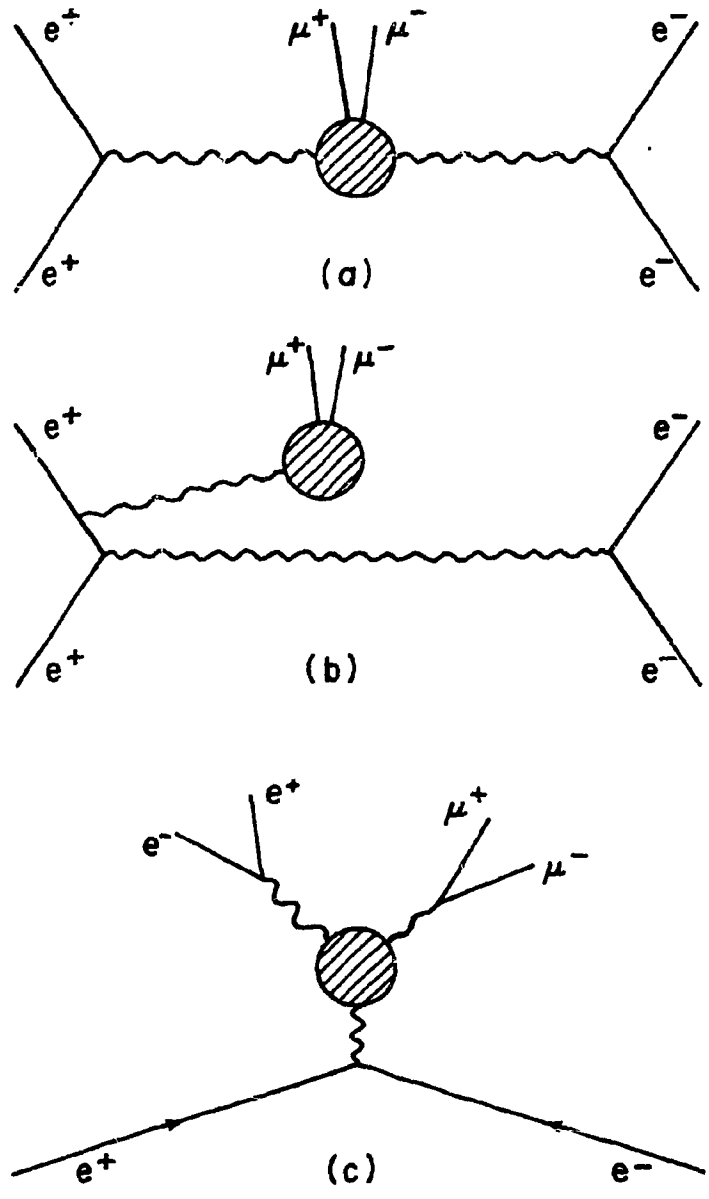

FIGURE VII-4. The Feynman diagrams describing the two-photon process $e^+e^- \to e^+e^-\mu^+\mu^-$. Diagram (a) gives the dominant contribution.

solid angle subtended by the polymeter. The restriction that the muons be noncoplanar by more than 20^{o} severely suppressed the contribution to the two-prong events from the two-photon process. The reason for this is that the net transverse momentum of the muons had to be balanced by that of the outgoing electrons. Characteristically, for muon noncoplanarities greater than 20^{o}, one of the electrons would have enough trnasverse momentum to be detected within the polymeter, which extended down to a polar angle of $\theta = 11^{o}$. Thus, instead of generating a two-prong event, the detection of the electron trajectory caused the event to be classified as three-prong.

The result was that the calculated contribution to the two-prong muon events with noncoplanarity greater than 20^{o} was only .01 events at 4.8 GeV. This compared with 2.05 events with $n_{ch} \geq 3$ (with no coplanarity restriction).

4. Muons from ψ and ψ' Decays

Another source of muon events not yet considered arises from the possibility that a $\psi(3095)$ or $\psi'(3684)$ meson could be formed at 3.8 or 4.8 total center of mass energy. This would occur if the electron-positron system radiated a photon such that the CM energy of the remaining system was precisely that of either of the resonances:

$$e^{+}e^{-} \rightarrow \gamma\psi \qquad \text{or} \qquad e^{+}e^{-} \rightarrow \gamma\psi' \ .$$

The rates of production of these resonances as a function of s are calculable from an expression deduced by J. D. Jackson.[6] The cross section is given by

$$\sigma(s) = t\cdot(\text{Area})_{0}\cdot \{ (\sqrt{s} - M)^{t-1}/E^{t} - 1/E + (\sqrt{s} - M)/2E^{2}\}$$

where

$$t = \frac{2\alpha}{\pi} \{ \ln(s/m_e^2) - 1 \} ,$$

$$E = \sqrt{s}/2 ,$$

and

$$(\text{Area})_o = \int \sigma_o(w)dw \simeq \frac{\pi}{2}\Gamma\sigma_{omax} .$$

Here σ_{omax} is the cross section of the resonance at its peak, not including radiative corrections, M is the mass of the resonance and Γ is its width. The current values[7] for the areas of the peaks are 10.4 ± 1.5 nb-GeV for the ψ and 3.7 ± 0.6 nb-GeV for the ψ'. This gives the following production cross sections at 3.8 and 4.8 GeV:

$\sqrt{s}$	$\sigma(\psi)$	$\sigma(\psi')$
3.8 GeV	719 ± 104 pb	1857 ± 301 pb
4.8 GeV	252 ± 36 pb	155 ± 25 pb

The photons created during the production of the ψ and ψ' tend to be radiated along the beam. For this reason, the direct decay of a ψ or ψ' into a muon pair,

$$\psi \rightarrow \mu^+\mu^- \qquad \text{or} \qquad \psi' \rightarrow \mu^+\mu^- ,$$

produces muons that are noncollinear, but are approximately coplanar. The branching ratios to muon pairs are 6.9 ± 0.9% for the ψ and 0.97 ± 0.16% for the ψ'. Using these branching ratios, together with the production cross sections, the number of decays to μ pairs expected in the SP8 data can be calculated according to

$$\text{No. of } \mu\text{'s} = 2L\sigma(s)\, B_{\mu\mu}\, \frac{\Delta\Omega}{4\pi} ,$$

where L is the luminosity, $B_{\mu\mu}$ the branching ratio, and $\Delta\Omega$ the spectrometer solid angle. The factor of 2 results from the fact that the single-particle trigger is sensitive to either of the two muons produced by the decay. The expected number of observed muon pair events from this direct decay is thus given by:

$\sqrt{s}$	$\psi \to \mu^+\mu^-$	$\psi' \to \mu^+\mu^-$
3.8 GeV	0.8	0.3
4.8	1.1	0.1

Because they are two-prong and coplanar, these events do not contribute to the sample of $n_{ch} = 2$ events with coplanarity greater than 20°, nor to the sample with $n_{ch} \geq 3$.

The only additional ψ or ψ' decay which would yield muon pairs as the only charged particles is the cascade decay,

$$\begin{array}{l} e^+e^- \to \gamma\psi' \\ \qquad\quad \hookrightarrow \psi + \text{neutrals} \\ \qquad\qquad\quad \hookrightarrow \mu^+\mu^- \ . \end{array}$$

The muons from this process will tend to be roughly coplanar, but if the neutrals carry away large transverse momenta, the muons could be noncoplanar by a few degrees. The total number of observed muon pairs produced by this process[8] is estimated to be 0.17 ± 0.04. The coplanarity distribution of the muons depends on the specific neutrals produced and on the dynamics, so that a precise statement cannot be made. Taking a specific example, where

$$\begin{array}{l} \psi' \to \psi\eta_o \\ \qquad\ \hookrightarrow \mu^+\mu^- \ , \end{array}$$

which has a branching ratio to all ψ' decays of 4 ± 2%, one obtains a maximum noncoplanarity of about 8° for the muon pair, assuming the ψ'

is travelling along the beam. Thus, with a 20° coplanarity cut, this type of process would not produce any contributions to the two-prong sample. To summarize, the expected number of observed muon pairs from this process was 0.17 at 4.8 GeV, none of which would be in the noncoplanar sample.

D. Observation of Anomalous μ Production in $n_{ch} = 2$ Events

In order to determine whether known processes can account for the 13 observed muon events with $p_{\mu} \geq 1.05$ GeV/c, $n_{ch} = 2$, and noncoplanarity greater than 20°, the contributions from each of the processes described in Section C must be added together. For the 4.8 GeV data, integration of the QED differential noncoplanarity cross section over coplanarity angles greater than 20° gave a total of 5.5 events. The number of events expected from misidentification of two-prong hadron events was 0.9 ± 0.2. The number of two-prong events resulting from the process $ee \rightarrow ee\mu\mu$ was found to be negligible if the coplanarity was required to be greater than 20°. And, finally, no contribution to the two-prong muon events resulted from ψ and ψ' decays, again because of the coplanarity restriction. The possibility that random tracks could have simulated noncoplanar muon events was also investigated and found to be negligible.

Adding all these contributions gives the result that 6.4 events were expected, as compared with the 13 events observed, shown in Fig. VII-3. The probability that the 13 observed events represent a statistical fluctuation in the expected number can be calculated from a Poisson distribution:

$$P(n \geq 13) = \sum_{n=13}^{\infty} e^{-6.4} 6.4^n/n! = 1 - \sum_{n=0}^{12} e^{-6.4} 6.4^n/n!$$

$$= .014 = 1.4\%.$$

The inclusive muon cross section corresponding to the excess of 6.6 events can be calculated from the integrated luminosity and solid angle:

$$\left.\frac{d\sigma}{d\Omega}\right|_{90^o} = \frac{6.6}{L\Delta\Omega} = 17.0 \text{ pb/sr} .$$

The uncertainty in this value is dominated by statistical fluctuations in the 13 observed events, with much smaller uncertainties in the estimated backgrounds and the integrated luminosity. Based on the observation of 13 events, the Poisson precision limits corresponding to one standard deviation (of a Gaussian distribution) may then be assigned to give

$$\left.\frac{d\sigma}{d\Omega}\right|_{90^o} = 17^{+12}_{-9} \text{ pb/sr}.$$

An examination of similar muon production in the 3.8 GeV data shows that the statistics were too small to justify drawing any significant conclusions. From Table VII-1b it is seen that three muon events were observed having noncoplanarity greater than 20^o. The results of Section C are that 2.0 events were expected from the QED noncoplanarity cross section integration, and 0.1 event from hadron misidentification. Thus 2.1 events were expected and 3 were observed.

E. Comparison with SLAC-LBL μe Events

The SLAC-LBL collaboration has reported[9,10] the observation of a number of μe events in their solenoid detector at SPEAR. In these events, the only charged tracks were an electron and a muon with momenta greater than 0.65 GeV/c, and there were no detected neutrals. After background subtractions, they report an "observed" μe production cross section of 20 ± 5 picobarns at 4.8 GeV. This is not a total cross section, but is simply what was observed within their detector. This detector wrapped around the beam line and subtended a solid angle of about 0.65 x 4π. At least two tracks were required for the trigger, and the momenta of both the muon and the electron were required to be above 0.65 GeV/c.

Under these circumstances, it is quite difficult to attempt a direct comparison between the SP8 result and that of SLAC-LBL, with the idea that the two signals might have a common origin. Any comparison of total cross sections would require considerable knowledge of the final states involved. This is due not only to the fact that neither experiment covered the entire solid angle, but also from the angular and momentum cuts imposed on the data. If one naively assumed an isotropic muon distribution in the final state, then the total inclusive cross section observed by SP8 would be 214^{+151}_{-113} pb.

This cross section must also be corrected for the 1.05 GeV/c momentum threshold. The momentum distribution can be estimated by assuming the anomalous muons result from the production and decay of a pair of heavy leptons. The production cross section is given by

$$\frac{d\sigma}{d\Omega} = \frac{\alpha^2}{4s}\,\beta\,\{(1-\cos^2\theta) + (1-\beta^2)\sin^2\theta\}\,.$$

Assuming V - A decay, neglecting final state masses, and assuming the S-wave dominated near threshold, one finds that the heavy lepton spins will tend to be aligned parallel to the beams. The secondary muon and electron momentum distribution is then found to be[11]

$$f(x) \sim x^2(3 - 2x) ,$$

where $x = p/p_{max}$ and p, p_{max} are the momenta in the rest frame of the heavy lepton. In the lab frame this gives

$$f(p) \sim (3 - p)p^2/4 .$$

Integrating this for $p \geq 0.65$ GeV/c gives a multiplicative correction factor of 1.20 needed to extend the SP8 inclusive muon cross section to a threshold of 0.65 GeV/c. Thus, the total SP8 muon inclusive cross section for momenta greater than 0.65 GeV/c and noncoplanar by more than 20^o would be 257^{+181}_{-136} pb.

In order to compare this with the SLAC-LBL cross section, that value needs to be corrected for the solid angle of the apparatus and the trigger configuration. If one makes the (unjustified) assumptions that the angles of emission of the electron and muon are uncorrelated, and that each particle is emitted isotropically, then the probability of the muon's being within the angular acceptance of the solenoid detector is 0.65, and likewise for the electron. Thus, the probability of triggering on an eμ event would be 0.65 x 0.65 = 0.42. With a 100% trigger efficiency for particles within the detector solid angle, this would give a total eμ production cross section of 47 ± 12 pb.

An additional factor needing consideration was the SLAC-LBL requirement that both particles have momenta above 0.65 GeV/c, while the SP8 particle outside the spectrometer had no momentum cut.

Integrating over the above momentum spectrum for $p < 0.65$ GeV/c gives a factor of 1.06 by which the SLAC-LBL cross section needs to be increased for purposes of comparison.

If one assumes that these eμ events were being produced by a decay process of the type

$$e^+e^- \rightarrow U\bar{U}, \quad U \rightarrow \begin{cases} e + \text{neutrals} \\ \mu + \text{neutrals} \end{cases},$$

and that the unknown U particle were equally likely to decay to a muon or an electron, then the total eμ cross section would account for half of the leptonic decays of the U, the other modes being ee and μμ. This model would then give a total muon inclusive cross section of 101 ± 25 pb for the SLAC-LBL data to compare with 257^{+181}_{-136} for the SP8 results. The precision limits of these two cross sections overlap slightly, suggesting that they are compatible, given the large number of assumptions which had to be made in order to make the comparison.

A second crude comparison which could be made was to estimate the likelihood of observing an eμ event with the muon tagged in the spectrometer and the electron in the conjugate side shower detector. No such events were observed. Assuming isotropy and no angular correlation between the muon and electron, the number of such events expected was found to be about 0.3 as estimated from the SLAC-LBL cross section. This is certainly consistent with having observed none. Given the 1.05 GeV/c muon momentum requirement and the noncollinearity cut at 20^o, an upper limit on the eμ cross section is found to be

$$\left.\frac{d\sigma}{d\Omega}\right|_{90^o} < 7.5 \text{ pb/sr}$$

with 95% confidence.

F. Search for Anomalous Muon Production in $n_{ch} \geq 3$ Events

In order to determine whether known processes can account for the observed muon events with more than two charged particles, a procedure was applied similar to that used for the two-prong events, where the contribution was calculated for each known process and the total compared with the observed events. As shown in Table VII-2, there were 4 events at 4.8 GeV and 5 events at 3.8 GeV having $n_{ch} \geq 3$ and $p \geq 1.05$ GeV/c. In several of these events, two back-to-back, high-momentum muons were observed. However, in this case, unlike the two-prong case, no collinearity or coplanarity cuts were made.

The nature of the hadron misidentification problem was discussed in Section VII-C-2 as applied to the $n_{ch} = 2$ events. The same procedures were applied to the calculation of the hadron misidentification of higher multiplicity events. The results are broken down in Table VII-3. The total muon contributions from hadron misidentification were 3.0 ± 0.3 events at 4.8 GeV and 0.5 ± 0.1 events at 3.8 GeV.

It was pointed out in Section VII-C-3 that the two photon process produced primarily three-prong events, since a deflected electron would usually be seen in the polymeter. The result was that 2.1 events were expected from this process at 4.8 GeV and 0.4 events at 3.8 GeV.

The remaining major contributing process to high-momentum muons with $n_{ch} \geq 3$ was the decay,

$$
\begin{array}{l}
e^+e^- \rightarrow \psi'\gamma \\
\quad\quad \hookrightarrow \psi + \text{charged particles} \\
\quad\quad\quad \hookrightarrow \mu^+\mu^- \quad .
\end{array}
$$

A calculation of the rates for this process follows the same outline as was presented in Section VII-C-4 for two-prong events. The number of muon events expected to be observed from this decay was calculated according to

$$N_\mu = 2L \frac{\Delta\Omega}{4\pi} \sigma_{\psi'}(s) \frac{\Gamma(\psi'\to\psi+\text{charged})}{\Gamma(\psi'\to\text{hadrons})} \frac{\Gamma(\psi\to\mu^+\mu^-)}{\Gamma(\psi\to\text{all})} \quad ,$$

where L is the luminosity, and the Γ's represent the various decay rates:

$$\frac{\Gamma(\psi'\to\psi+\text{charged})}{\Gamma(\psi'\to\text{hadrons})} = 0.38 \pm 0.06 \; ,$$

$$\frac{\Gamma(\psi\to\mu^+\mu^-)}{\Gamma(\psi\to\text{all})} = .069 \pm .009 \; .$$

Using the integrated luminosity values given in Chapter V, the solid angle value 0.105 sr and the ψ' production cross sections given in Section VII-C-4 gives the result that the estimated number of muon events observed from this decay process was 0.80 ± 0.23 events at 3.8 GeV and 0.25 ± 0.07 events at 4.8 GeV.

Adding together the contributions from the various background processes gives the result that the mean number of events expected was 5.3 ± 0.3 at 4.8 GeV. This compares with the 4 observed events listed in Table VII-2a. If one takes the approach that the background observed is consistent with that predicted, corresponding to having seen no anomalous process, then an upper limit, at the 95% confidence level, for any anomalous cross sections is found to be

$$\left.\frac{d\sigma}{d\Omega}\right|_{90^o} < 7.5 \text{ pb/sr} \qquad \text{(95\% confidence level)}.$$

Assuming isotropy, this would yield an upper limit on the total cross section of 96 pb.

At 3.8 GeV, the predicted background for muons with $n_{ch} \geq 3$ was 1.7 ± 0.3 events. Table VII-2b shows that five such events were observed. However, four of these events have signatures that allow them to be associated with specific background sources. Event No. 1 had a pair of collinear muons with the spectrometer particle momentum almost equal to the maximum allowable 1.9 GeV/c for a μμ event arising from QED: $e^+e^- \rightarrow \mu^+\mu^-$. The other two tracks appear consistent with a single cosmic ray secondary passing through the polymeter near the beam region. Event Nos. 2 - 4 had the multiplicity, momentum and μμ collinearity values that indicate almost certainly that they resulted from the ψ' decay described above. The three events observed are consistent with the .8 ± .2 predicted. This leaves only one remaining background event at 3.8 GeV, compared with a hadron misidentification probability of 0.5 ± 0.1 events. Thus, the results at 3.8 GeV were also consistent with having seen no evidence of anomalous muon production for $p \geq 1.05$ GeV/c and $n_{ch} \geq 3$.

G. Implications of the Inclusive Muon Results

Results from the SLAC-LBL collaboration[9] have indicated the presence of a significant number of events with the signature

$$e^+e^- \rightarrow e^{\pm}\mu^{\mp} + \geq 2 \text{ undetected particles.}$$

The "observed" cross section for this signature, with backgrounds

having been subtracted, was about 20 ± 5 pb at 4.8 GeV total energy. Analysis of the angular and momentum distributions of these events strongly support the hypothesis that they are produced by the decay of a heavy fermion according to

$$\begin{array}{l} e^+e^- \to U^{\pm}U^{\mp} \\ \qquad\quad \big|\ \ \big|\!\to \mu^{\mp} + \text{neutrals} \\ \qquad\quad \big|\!\to e^{\pm} + \text{neutrals}\ . \end{array}$$

The mass of the unknown U particle is believed to be in the range 1.6 – 2.0 GeV. There is considerable evidence to support the hypothesis that the U is a heavy lepton, but other possibilities have not yet been conclusively ruled out.

The significance of the results presented in Section D was that they confirmed the existence of a source of $n_{ch} = 2$ muon events not accounted for by previously known processes and allowed a low statistics inclusive cross section measurement without constraining the second particle polar angle or momentum. A crude comparison between the SP8 and SLAC-LBL results showed them to be approximately consistent.

The absence of a signal in the $n_{ch} \geq 3$ sample was also significant, since this puts an important constraint on the possible muon production mechanisms. The results of the $n_{ch} = 2$ and $n_{ch} \geq 3$ measurements were analyzed by Dr. G. A. Snow[12], whose findings were that these results are compatible with a heavy lepton source, but not with charmed mesons. This latter conclusion was somewhat weaker, since it was estimated that only 10 – 15% of the muons produced by charmed meson decay would have $p > 1.05$ GeV/c.

REFERENCES

CHAPTER VII

1. M. Cavalli-Sforza, et al., Phys. Rev. Lett. 36, 558 (1976).
2. F. A. Berends, K. J. F. Gaemers, and R. Gastman, Nucl. Phys. B57, 381 (1973).
3. For comparisons of the QED calculation programs with experiment, see B. L. Beron, et al., Phys. Rev. Lett. 33, 663 (1974); J. E. Augustin, et al., Phys. Rev. Lett. 34, 233 (1975); and J. E. Zipse, Ph.D. thesis, Lawrence Berkeley Laboratory Report No. LBL 4281, 1975 (unpublished).
4. Private communication from K. J. F. Gaemers.
5. G. Grammer, Jr. and T. Kinoshita, Nucl. Phys. B80, 461 (1974). For a comparison of these calculations with the experimental results from the SLAC-LBL magnetic solenoid detector, see J. E. Zipse, Ph.D. thesis, Lawrence Berkeley Laboratory Report No. LBL 4281, 1975 (unpublished).
6. J. D. Jackson, Lawrence Radiation Laboratory Memo No. JDJ/74-3 (unpublished); G. Bonneau and F. Martin, Nucl. Phys. B27, 381 (1971).
7. A. M. Boyarski, et al., Phys. Rev. Lett. 34, 1357 (1975);V. Lüth, et al., Phys. Rev. Lett. 35, 1124 (1975).
8. G. S. Abrams, Proceedings of the 1975 International Symposium on Lepton and Photon Interactions at High Energies, Stanford University, p. 25.
9. M. L. Perl, et al., Phys. Rev. Lett. 35, 1489 (1975).
10. M. L. Perl, et al., Phys. Lett. 63B, 466 (1976).

11. Y. S. Tsai, Phys. Rev. D4, 2821 (1971).

12. G. A. Snow, Phys. Rev. Lett. 36, 766 (1976).

CHAPTER VIII

CONCLUSION

This experiment was designed primarily to measure the inclusive momentum spectra for hadrons produced in electron-positron colliding beam interactions. The final sample of events was required to have spectrometer particle momentum greater than 400 MeV/c. The kaon spectrum was not quoted for momenta less than 700 MeV/c due to large uncertainties resulting from their interactions within the apparatus. Muons were tagged at momenta greater than 1.05 GeV/c. No results were quoted for inclusive electron production, since the 0.3 radiation lengths of material in front of the magnet caused severe degradation of the electron spectrum.

The results of the inclusive hadron measurements indicated that, within the SP8 statistics, Bjorken scaling of the $sd\sigma/dx$ cross section versus x ($= 2E/\sqrt{s}$) holds for $x > 0.4$. This form of scaling holds separately for the pions and for the kaons; however, the measurements give a strong indication that the pion and kaon x-distributions are different.

Other SP8 results on the Lorentz-invariant cross section, which had previously been observed by the SLAC-LBL collaboration, indicate that Feynman scaling holds over the entire measured momentum range, when the cross sections are summed over particle types. Plotting the invariant cross sections for the different particle types versus the particle energy resulted in the somewhat surprising behavior that they all seem to fall on or near the same exponential curve. SLAC-LBL has found this to be true for their low-momentum data at CM energies

ranging from 3.0 to 7.4 GeV. This dependence of the cross section only on the particle energy is what one would expect from a thermodynamic model of e^+e^- hadron production. In such models, the electron and positron interact to form a "hot hadron gas". The approximate equipartition of energy could be established as a result of the large magnitude of the strong interaction coupling, in the short time before the "gas" dissipated. The "temperature" of the hadron gas can be deduced from the exponential slope of the invariant cross section. The SP8 results at 4.8 GeV agree rather closely with the SLAC-LBL low-momentum results at CM energies from 3.0 to 7.4 GeV: the hadron temperature is

$$kT = 0.19 \text{ GeV}.$$

Another interesting result found by SLAC-LBL was that their inclusive hadron momentum spectrum was described very well by a simple phase space model.

Results were also found for the mean hadron charged multiplicity as a function of the inclusive hadron momentum. The multiplicity rises smoothly from 0.4 GeV/c and peaks at 0.8 GeV/c with a value of about 3.9. Except for the anomalous data point at 0.85 GeV/c, the multiplicity then falls gradually as the momentum is increased. There was some suggestion from the relatively large number of two-prong events at the lower momenta and the high degree of coplanarity exhibited by these events, that the fall-off in charged multiplicity at the lower momenta might be due to the effects of the two-photon process, or at least to some other possible process with similar properties.

The measurements of the inclusive muon spectrum found a small anomalous signal among the two-prong events with $p_\mu > 1.05$ GeV/c and noncoplanarity greater than 20°:

$$d\sigma/d\Omega\Big|_{90^\circ} = 17\ ^{+12}_{-9}\ \text{pb/sr} \quad .$$

A highly model-dependent comparison with the SLAC-LBL results from μe events showed approximate agreement if the muon source were postulated to be the production and decay of a heavy fermion. No anomalous muon production was seen in the higher multiplicity events, giving the upper limit on anomalous inclusive muon production of

$$d\sigma/d\Omega\Big|_{90^\circ} < 7.5\ \text{pb/sr} \qquad (95\%\ \text{confidence level}).$$

APPENDIX A

THE MAGNETIC FIELD FIT

The principal component of the magnetic field is shown as a function of position in Fig. A-1. The data used to fit the field was taken at one-inch increments along each of 25 lines running parallel to the central axis through the magnet. The spatial coordinates chosen for the fit were those used during the mapping of the magnetic field: The x axis was north along the beam, the y axis was vertical, and the z axis was out of the magnet toward the beam. The origin of coordinates was the center of the magnet, and measurements were made in inches.

The 25 lines selected for fitting formed a grid of 5 x values at 16-inch increments and 5 y values at 8-inch increments. The principal features of each of the three field components were fit. There was very little x-dependence in any of the components. The value of the field depended most strongly on the z coordinate, with large y-dependent perturbations near the magnetic poles at each end of the gap.

The average fitting error of the integrated vertical field component over the entire grid was 0.6%. The error was smaller along rays nearer the z axis, having a value of 0.09% along the z axis. Most of the errors resulted from field perturbations near the magnet surfaces.

The input to the subroutine BFIELD consists of the three-dimensional position coordinate at which the field is to be evaluated. These coordinates were the usual SP8 coordinates in centimeters with x south along the beam, y vertical, and z along the central axis of

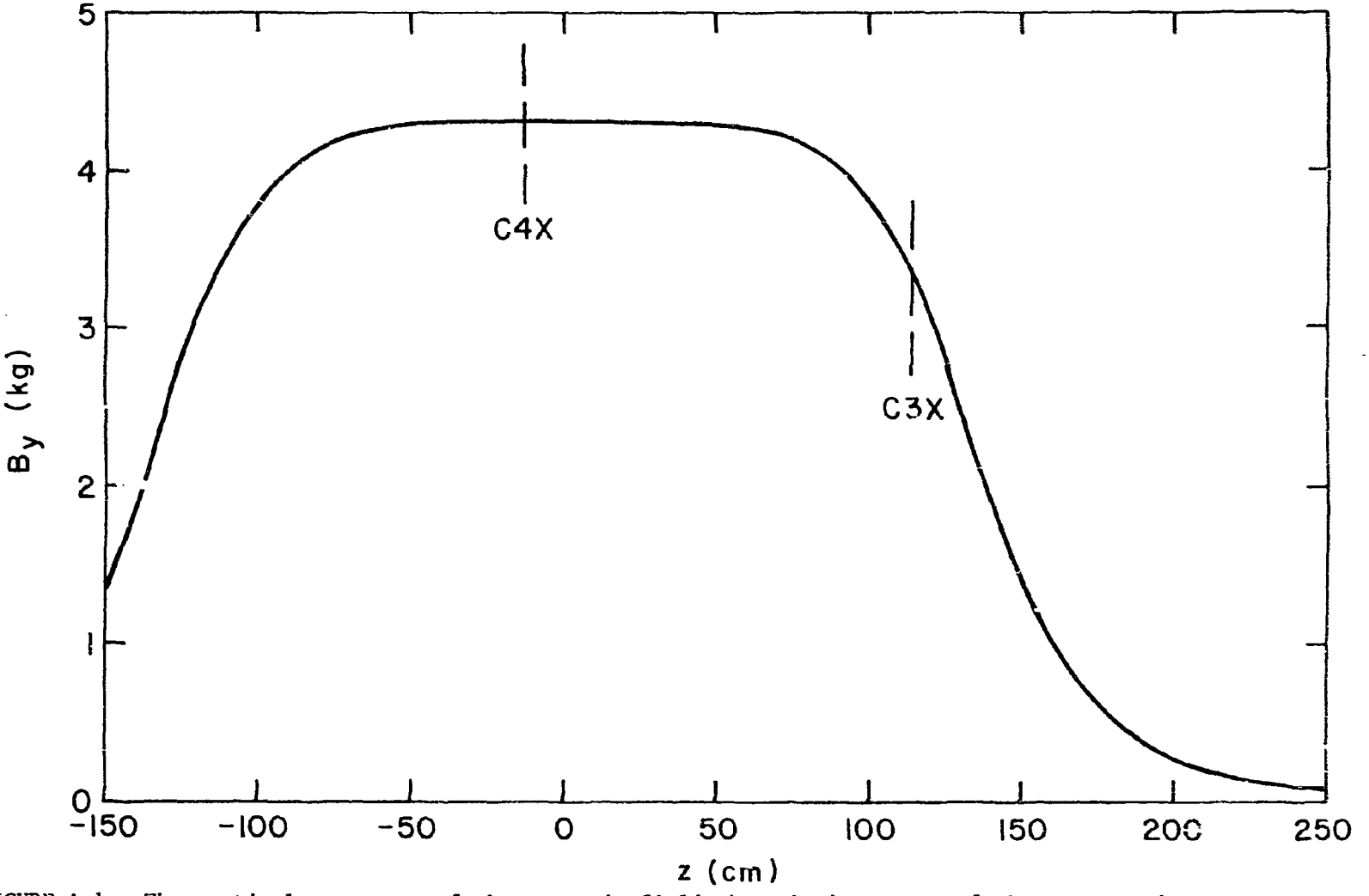

FIGURE A-1. The vertical component of the magnetic field through the center of the magnet, shown as a function of the distance from the magnet center. The beam interaction region was located at z = 311 cm to the right. The C5X chamber was located at z = -165 cm.

the magnet running away from the beam. The coordinate origin was near the center of the beam interaction region. A listing of the subroutine BFIELD follows:

```
      SUBROUTINE BFIELD(XI,B)
      DIMENSION AZ(20),CZ(20),B(3),XI(3)
      DATA AZ/101.2,82.55,64.39,56.73,46.41,28.06,23.70,-23.63,
     1 -28.06,-46.37,-56.73,-70.17,-82.55,8*-100./
      DATA CZ/101.2,87.23,61.77,54.21,49.41,43.62,0.,-43.62,
     1 -49.41,-54.21,-61.77,-87.23,8*-100./
C
C   FIRST CONVERT POSITION COORDINATES FROM CENTIMETERS TO INCHES AND
C   CONVERT FROM MAGNETIC FIELD MEASUREMENT COORDINATE SYSTEM TO SP8
C   COORDINATES WITH THE ORIGIN AT THE BEAM INTERACTION REGION.
C
      Y=XI(2)/2.54
      X=-XI(1)/2.54
      Z=-(XI(3)-311.32)/2.54
      BX=B(1)
      BY=B(2)
      BZ=B(3)
C
C   COMPARE Z VALUE WITH VARIOUS EXTREMA TO DETERMINE WHICH FUNCTION TO
C   BE USED TO CALCULATE BY.
C
      DO 100 I=1,20
      IF(Z.GT.AZ(I)) GO TO 110
100   CONTINUE
110   IA=I-1
C
C   ZERO THE FIELD IF OUTSIDE THE FIT REGION.
C
      IF(IA.NE.0.AND.IA.NE.20) GO TO 115
      B(1)=0.
      B(2)=0.
      B(3)=0.
      RETURN
115   CONTINUE
C
C   COMPARE Z VALUE WITH VARIOUS EXTREMA TO DETERMINE WHICH FUNCTION TO
C   BE USED TO CALCULATE BY.
C
      DO 120 I=1,20
      IF(Z.GT.CZ(I)) GO TO 130
120   CONTINUE
130   IB=I-1
C
C   CALCULATE MULTIPLICATIVE CORRECTIONS FOR Y-DEPENDENCE.
C
```

```
      DBY=2.61*Y**2+.00858*Y**4+.471E-4*Y**6
      DBY=DBY/3471.
      DBZ=108.5*Y+.3503*Y**3
      DBZ=DBZ/5183.
      BY=0.
C
C   CALCULATE BY(Z) FOR X=Y=0.
C
      GO TO (200,200,205,205,210,210,215,220,220,225,225,250,250,
     1 250,250,250,250,250,250,250),IA
200   BY=819.1*((101.2-Z)/36.8)**2
      IF(Z.GT.AZ(2)) BY=BY+25.-ABS(30.*Y/16.)
      IF(Z.LT.AZ(2)) BY=BY-20.-ABS(135.*Y/16.)
      GO TO 250
205   BY=819.1+2351.*(64.39-Z)/17.98
      IF(Z.GT.AZ(4)) BY=BY+100.*(Z-60.56)/(AZ(3)-AZ(4))-ABS(175.*Y/16.)
      IF(Z.LT.AZ(4)) BY=BY-100.*(Z-51.57)/(AZ(4)-AZ(5))
      GO TO 250
210   BY=4288.-1118.*((Z-23.7)/22.71)**2
      IF(Z.GT.AZ(6)) BY=BY+35.+ABS(115.*Y/16.)
      GO TO 250
215   BY=4288.
      GO TO 250
220   BY=4288.-1118.*((Z+23.63)/22.74)**2
      IF(Z.LT.AZ(9)) BY=BY+35.+ABS(115.*Y/16.)
      GO TO 250
225   BY=3170.*(70.17+Z)/23.80
250   CONTINUE
      IF(Z.LT.100..AND.Z.GT.70.) BY=BY-(((ABS(X/32.))**2.48*1118.-128.)
     1 *ABS((Y-25.)/16.)-400)/30.
C
C   CALCULATE Z-DEPENDENT CORRECTION TO BY(Z) FOR Y .NE. ZERO.
C
      CBY=46.42
      ZT=Z
      IF(Z.LT.0.) ZT=-Z
      GO TO (255,260,260,265,270,300,300,300,270,265,260,260,300,
     1 300,300,300,300,300,300,300),IA
255   CBY=-39.91
      GO TO 300
260   CBY=-2857.*((ZT-82.55)/25.82)**2
      GO TO 300
265   CBY=3471.-6328.*(ZT-46.41)/10.32
      GO TO 300
270   CBY=3471.*((ZT-28.06)/18.35)**2
300   BY=BY+CBY*DBY
C
C   CALCULATE BZ(Z) FOR X=Y=0.
C
      BZ=-68.31
      GO TO (310,315,320,325,330,350,350,330,325,320,315,350,350,
     1 350,350,350,350,350,350,350),IB
310   BZ=-87.71
```

```
      GO TO 350
315   BZ=-87.71-769.6*((ZT-87.23)/25.46)**2
      GO TO 350
320   BZ=-857.3+4326.*(ZT-61.77)/7.56
      GO TO 350
325   BZ=-5183.
      GO TO 350
330   BZ=-68.31-5115.*(ZT-43.62)/5.79
350   IF(Z.LT.0.) BZ=-BZ
C
C   CORRECT BZ(Z) FOR Y .NE. ZERO.
C
      BZ=BZ*DBZ+5.7
      IF(ABS(Z).GT.35..AND.ABS(Z).LT.70.) BZ=BZ-SIGN(595.,Y)*(ABS(Y/16.)
     1 )**.208*SIGN(1.,Z)
      IF(Z.GT.100..OR.Z.LT.70.) GO TO 380
      IF(ABS(Y).GT.8.) BZ=BZ-2417./30.
      IF(ABS(Y).LE.8.) BZ=BZ-(2670.*Y/8.)/30.
C
C   CALCULATE BX.
C
380   BX=0.
      IF(ABS(Z).LT.54.21) BX=-24.
      B(1)=BX
      B(2)=BY
      B(3)=BZ
      RETURN
      END
```

APPENDIX B

MULTIWIRE PROPORTIONAL CHAMBERS

Chamber	Planes	Wires	Spacing (mm)	Length (cm)	Distance from Beam (cm)
Polymeter (top)	3	3 x 47	3	168.6	10.4/11.8/13.2
(west)	3	3 x 140	3	168.6	10.7/12.1/13.5
(bottom)	3	3 x 47	3	168.6	10.4/11.8/13.2
(east)	3	3 x 140	3	168.6	10.7/12.1/13.5
C1AX	1	444	2	20.0	20.5
C2AX	1	448	2	48.3	32.7
C2AY	1	70*	4*	75.0	27.8
C1BX	1	444	2	20.0	21.4
C2BX	1	448	2	48.5	37.9
C2BY	1	60*	4*	78.1	32.5
C3X	1	644	2	57.1	197.2
C3Y	1	280	2	141.3	216.4
C4X	1	868	2	74.5	324.7
C4Y	1	364	2	174.9	344.4
C5X	1	1148	2	114.4	476.5
GTS	2	168/70	2	13.6/33.0	203.4/202.0
GBS	2	168/70	2	13.6/33.0	203.1/201.7
GTN	2	168/70	2	13.6/33.0	203.7/202.3
GBN	2	168/70	2	13.6/33.0	203.6/202.2

* The C2AY and C2BY had respectively 70 and 60 connected pairs of wires with 2 mm spacing.

APPENDIX C

THE CERENKOV COUNTER

A side view of the Cerenkov counter is shown in Fig. C-1. A particle entering from the right first penetrated the entrance window, a 0.2 cm thick half cylinder of aluminum. The pressure vessel was filled with 7 atm (6 atm gauge) of propane gas. The radiating path length until the particle passed through the mirror was typically 130 cm. The mirror was 1.3 cm thick plexiglass coated with a front surface aluminum finish with a $\frac{1}{4}\lambda$ MgF_2 overcoat for durability and to give constructive interference reflection for ultraviolet radiation. The ultraviolet reflectivity at 3000 Å was about 85% at normal incidence and fell off rapidly around 2000 Å. Optical absorption in propane also becomes serious around 2000 Å, resulting in a cutoff in the Cerenkov radiation at lower wavelengths.

The angle of emission of the Cerenkov radiation relative to the particle direction is given by

$$\cos \theta = 1/n\beta,$$

where n is the index of refraction and β is the particle velocity. The threshold for emission is defined by $\beta_t = 1/n$. The corresponding momentum threshold is given by

$$P_t = \frac{m_o c}{\sqrt{n^2 - 1}} .$$

The Clausius-Mossotti equation has been found to accurately describe the polarization properties of the paraffins over a very large pressure range. It relates the index of refraction to the density according to

$$(n^2 - 1)/(n^2 + 2) = K\rho,$$

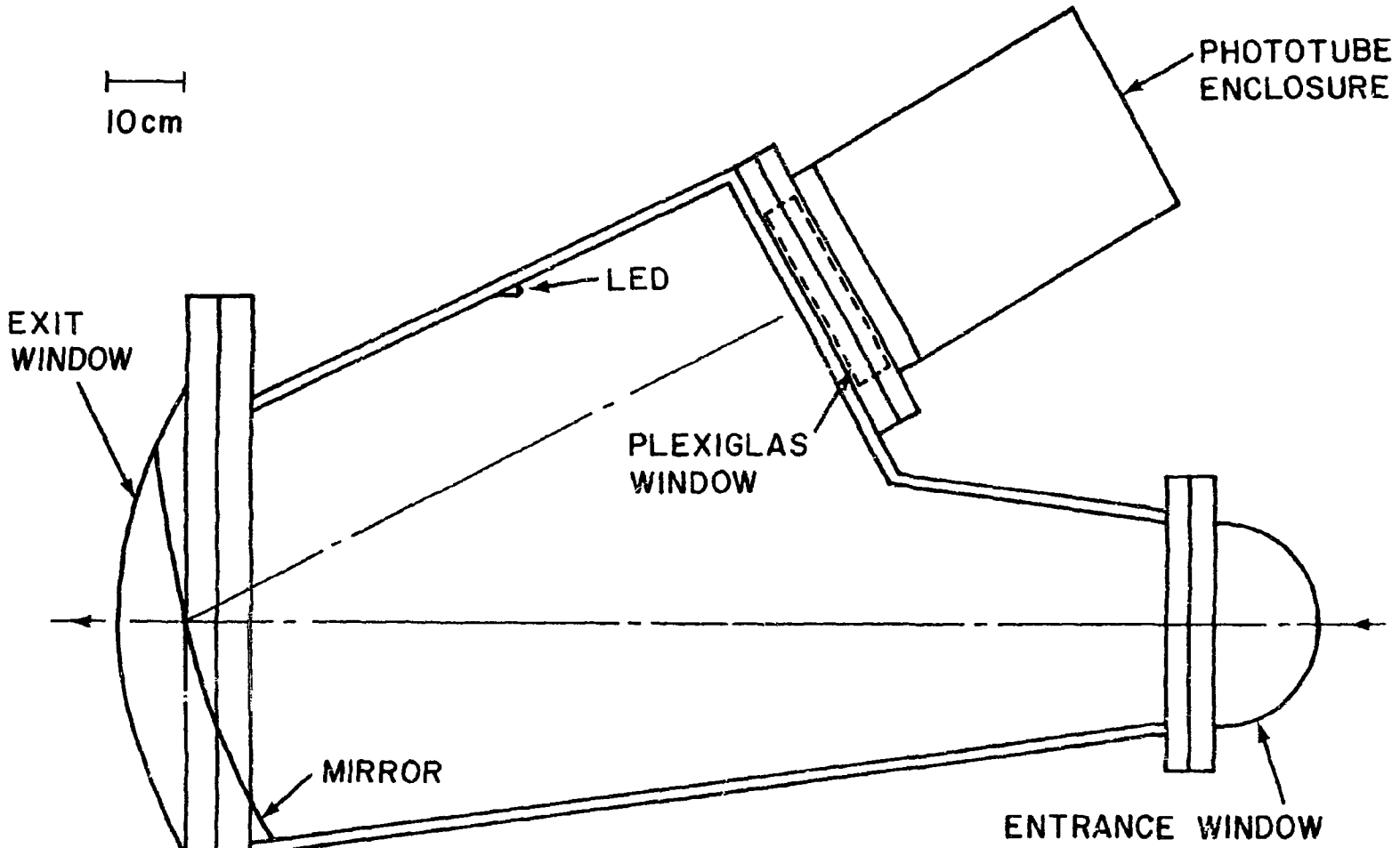

FIGURE C-1. The threshold Cerenkov counter. Particles entered from the right and radiated forward into the mirror, which reflected the Cerenkov radiation upward through the Plexiglass window to the photomultipliers. A wavelength shifter was coated on the front of the Plexiglass window.

where K is a constant equal to the molecular polarizability divided by the molecular weight. Since the refractive index has been accurately measured at atmospheric pressure, this value can be used to determine n at any density:

$$n = \left[\frac{\rho_o(n_o^2+2) + 2\rho(n_o^2-1)}{\rho_o(n_o^2+2) - \rho(n_o^2-1)} \right]^{\frac{1}{2}} .$$

Using the values $n_o = 1.00110$ and $\rho_o = 2.01$ mg/cm^3, and the density at 105 psia and 21°C of $\rho = 15.01$ mg/cm^3 extrapolated from the Matheson tables,[1]

$$n = 1.00823.$$

The differential Cerenkov photon spectrum as a function of wavelength is given by

$$\frac{dN}{d\lambda} = \frac{2\pi L}{137}\left[\frac{\sin\theta}{\lambda}\right]^2 = 5.96 \text{ cm} \cdot \left[\frac{\sin\theta}{\lambda}\right]^2 .$$

The total number of photons radiated above the 2000 Å cutoff is then

$$N_{TOT} = 5.96\text{cm} \cdot \sin^2\theta \int_{2000\text{Å}}^{\infty} \frac{d\lambda}{\lambda^2} = 2.98 \times 10^5 \sin^2\theta .$$

For $\beta = 1$, corresponding to $\theta = 7.33°$, this gives $N_{TOT} = 4845$ photons.

The radius of curvature of the spherical mirror was 118 cm. The distance from the center of the mirror to the photomultiplier plane was about 89 cm, so that a particle source about 31 cm outside the entrance window would be "in focus" on the detector plane. In fact, since the Cerenkov light was emitted at angles as much as 7° from the particle direction of travel, the resulting image was not a point but a halo. The detector array consisted of 48 56AVP 2-inch photomultipliers. The tubes were close packed in five offset rows of nine or ten tubes each. The active detector area spanned about

53 cm horizontally and 23 cm vertically. An effective angular aperture subtended from the center of the mirror can be defined by the particle source positions such that 50% of the photons in the halo fall within the active detector region. These 50% efficiency angles were $\pm 7^{o}$ vertically and $\pm 17^{o}$ horizontally. Of course particles outside this aperture hitting some parts of the mirror other than the center could still have been efficiently detected, while others within the aperture would have been lost. In this experiment the beam interaction region was well within the aperture.

The detector assembly included a 2.5 cm thick lucite window with a first surface coating of a P-terphenyl wavelength shifter.[2] Behind the lucite was an iron magnetic shield honeycombed with 5.4 cm holes for photomultiplier insertion. After tests with the magnet, it was found necessary to shield the photomultipliers by spacing them back from the lucite using plexiglass cookies with optical grease interfaces, and by wrapping them with several layers of netic.

The P-terphenyl wavelength shifter was practically transparent to visible light, but absorbed ultraviolet light and reemitted in the visible region of sensitivity of the photomultipliers with a quantum efficiency near 100%. The lucite window optical transmission[3] was about 70% at 3600 Å, rising to about 92% at longer wavelengths and dropping rapidly to zero at shorter wavelengths. The P-terphenyl radiated principally in the region 3600 Å to 4200 Å.

The photomultipliers were selected 56AVP's, optimized for uniform detection of single photoelectrons over the entire photocathode area. The maximum quantum efficiency is about 19% at 4200 Å. It falls rapidly through 10% at 3300 Å and at longer wavelengths is

10% at 5100 Å and 1% at 6100 Å. A pulse height spectrum given in ref. 2 for a P-terphenyl coating directly on the photomultiplier window indicated that about 2.5 times as much light was collected as for the uncoated tube.

Using the various depletion factors as a function of wavelength, one can estimate the number of photoelectrons which should be collected for a particle with $\beta = 1$: In the wavelength range from 3000 Å to 6200 Å there are about 1650 photons emitted; 1400 survive reflection from the mirror; 950 of these are transmitted by the lucite plate; 550 of these fall on a photocathode; and 73 of these produce photoelectrons. Multiplying this by a factor of 2.5 from the wavelength shifter gives about 180 photoelectrons maximum per event. This gives a statistical spread of $\sigma \approx 14$ photoelectrons or 7.5%.

There will also be a spread introduced into the Cerenkov amplitude from fluctuations in temperature and pressure during the course of the experiment. Density fluctuations resulted from a slow propane leak in the plumbing external to the Cerenkov counter during the course of the experiment and from possible condensation when temperatures were low, since the propane condensation temperature was only a few degrees below normal operating conditions. A 4.7% fluctuation was estimated for the number of photoelectrons collected. With this and the statistical effects superimposed, one expects about an 8.8% fluctuation in the Cerenkov amplitude. This compares with 9.7% observed from a sample of about 100 electrons, and does not take into account inefficiencies resulting from events where part of the image halo falls outside the phototube detector area. It also does not take into account possible differences in the individual

photomultiplier gains.

The counter amplitude a a function of momentum for a particle of given mass can be taken as proportional to the number of photons radiated, or

$$\text{Amplitude} \propto N_{TOT} \propto \sin^2 \theta = 1 - \frac{1}{n^2\beta^2} .$$

This can be normalized to electrons, where $\beta \simeq 1$.

APPENDIX D

THE LED CALIBRATION SYSTEM

In order to monitor the performance of all the scintillation counters and the Cerenkov counter, light-emitting diodes were installed in each counter. The "diode pulsing distribution system" shown in Fig. D-1 split the output of the Spencer-Kennedy pulser to provide a well timed pulse to each LED. In parallel with this LED pulse distribution system was a "pulser tree", not shown in the figure, which simulated one sense wire firing in each wire chamber. The "RF pulse simulation system" shown in Fig. D-1 provided a fake beam pickup signal, the only remaining ingredient necessary to satisfy the trigger coincidence. The fake RF signal was obtained by splitting off one of the LED fanout leads and returning it properly delayed to the RF discriminator. Thus the calibration events obtained by simultaneously firing the LED's and the pulser tree satisfied the trigger and were strobed into the computer and stored on magnetic tape along with the physical events resulting from electron-positron collisions.

The "TOF selective inhibit system" shown in Fig. D-1 was designed to inhibit three specified counters in each row of four. Diode events were accumulated for each inhibit configuration, allowing a clean time-of-flight reading to be simulated in the remaining counter in each row.

The TOF delay system shown at the bottom of the figure was a small box containing relays to introduce a 16 nsec delay into the S1 and S1' TOF cables. Pulsing the diodes in each relay state produced diode events with and without the 16 nsec delay. These were later

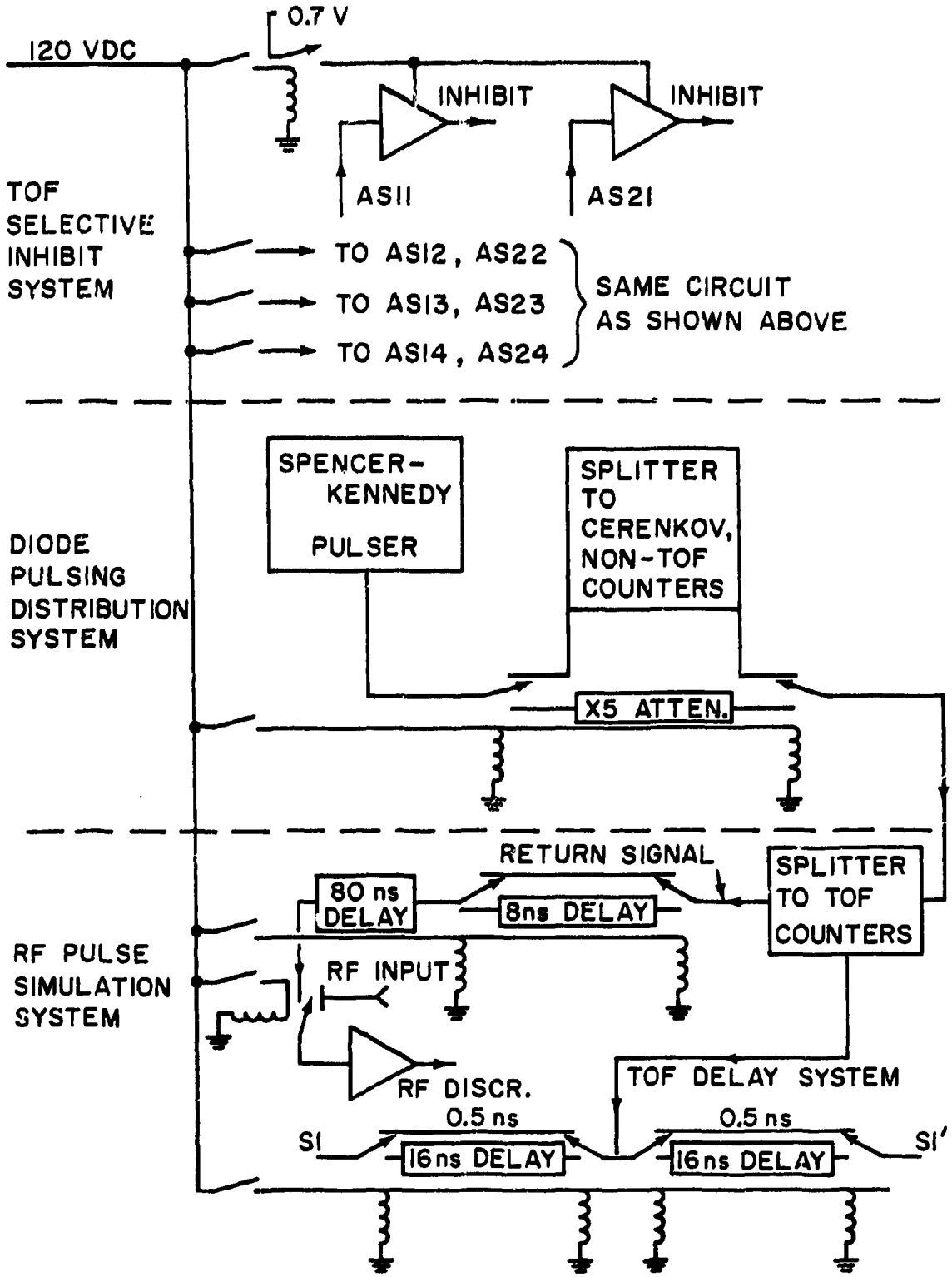

FIGURE D-1. The switching circuits used to control the pulsing of the light-emitting diodes. LED's were located in front of all the photomultipliers for calibration and monitoring purposes.

used to establish the ADC channel-number-to-nanosecond conversion factor for each TOF configuration.

APPENDIX E

EVENT WORD FORMAT ON DATA TAPES

The events were written on magnetic tape in groups of three, corresponding to the three partitions in the data buffer. The first event contained an extra eight-word heading giving such information as the data buffer sequence number (DBN), tape number, date, etc. Its contents are shown in Table E-1.

Following the heading, the rest of the first record was filled out with the first 148-word partition. The next two tape records would contain the second and third partitions, respectively, and then the three-event sequence repeated itself beginning with the next record.

The first 64 words in each partition contained the CAMAC block, the layout of which is shown in Fig. E-1. The first 40 of these were the LRS ADC's containing the scintillation counter and Cerenkov counter amplitudes. The remaining 24 CAMAC words were the outputs of the SLAC ADC's. Only nine of these were used, and they contained the values of the various time-of-flight outputs. Each 2114A word consisted of 16 bits. The eight least significant bits contained the amplitude value. The three most significant bits were CAMAC status bits and had to be stripped off before analysis began.

Words 65 through 148 contained the proportional wire chamber addresses, the hadron filter bits and other single-bit information. These storage assignments are shown in Fig. E-3. The 84 words were each divided into two eight-bit bytes. Each of these half words contained a different address. The bit format for a specific chamber

(C1AX) is shown in Fig. E-2. Words 146 through 148 contained single-bit information on which hadron filters were hit, whether the event was a diode calibration event, and whether the Cerenkov counter was above pedestal.

1	AS11	2	AS21	3	AS31	4	AS41	5	AS51
6	AS12	7	AS22	8	AS32	9	AS42	10	AS52
11	AS13	12	AS23	13	AS33	14	AS43	15	AS53
16	AS14	17	AS24	18	AS34	19	AS44	20	AS54
21	BS1T	22	BS2T	23	BS3T	24	BS4T	25	BS5T
26	BS1B	27	BS2B	28	BS3B	29	BS4B	30	BS5B
31	S1	32	S1'	33	GTS	34	GBN	35	GBS
36	GTN	37	—	38	—	39	—	40	CERENKOV
41	—	42	—	43	—	44	—	45	RF-AS1X
46	S1-AS1X	47	S1'-AS1X	48	S1-AS2X	49	S1'-AS2X	50	RF-S1
51	RF-S1'	52	RF-AS2X	53	RF-Ring	54	—	55	—
56	—	57	—	58	—	59	—	60	—
61	—	62	—	63	—	64	—		

FIGURE E-1. The Camac word block storage assignments for each event.

WORD NUMBER	CONTENTS
1	Partition length (= 148 words)
2	Write partition index
3	Read partition index
4	Number of words per event (= 148 words)
5	"COW", PWC R-card storage scheme
6	"BULL", CAMAC storage scheme
7	Data buffer number (DBN)
8	Month (02), Date (02), Tape # (02)

TABLE E-1. Contents of the data buffer heading, which is added to the beginning of every third event stored on the data tapes.

REFERENCES

APPENDIX C

1. The Matheson Company, Inc., "Matheson Gas Data Book," 430, (1966).

2. E. L. Garwin, Y. Tomkiewicz and D. Trines, Nucl. Instr. and Meth. 107, 365, (1973).

3. Rohm & Haas Company, Bulletin #PL-53f.

65	POLY I	66	POLY I	67	POLY I	68	POLY I	69	POLY I	70	POLY I
71	POLY I	72	POLY I	73	POLY I	74	POLY M	75	POLY M	76	POLY M
77	POLY M	78	POLY M	79	POLY M	80	POLY M	81	POLY M	82	POLY M
83	POLY O	84	POLY O	85	POLY O	86	POLY O	87	POLY O	88	POLY O
89	POLY O	90	POLY O	91	POLY O	92	C1AX	93	C1AX	94	C1AX
95	C1BX	96	C1BX	97	C1BX	98	C2ABY	99	C2ABY	100	C2ABY
101	C2AX	102	C2AX	103	C2AX	104	C2BX	105	C2BX	106	C2BX
107	C3XL	108	C3XL	109	C3XL	110	C3XH	111	C3XH	112	C3XH
113	C3Y	114	C3Y	115	C3Y	116	C4XL	117	C4XL	118	C4XL
119	C4XH	120	C4XH	121	C4XH	122	C4Y	123	C4Y	124	C4Y
125	C5XL	126	C5XL	127	C5XL	128	C5XM	129	C5XM	130	C5XM
131	C5XH	132	C5XH	133	C5XH	134	CGTS	135	CGTS	136	CGTS
137	CGBS	138	CGBS	139	CGBS	140	CGTN	141	CGTN	142	CGTN
143	CGBN	144	CGBN	145	CGBN	146	HF Bits	147	HF Bits	148	HF Bits

146	-	-	-	AH25	AH24	AH23	AH22	AH21	-	-	-	AH15	AH14	AH13	AH12	AH11
147	-	-	-	-	-	BH13	BH12	BH11	-	-	-	AH35	AH34	AH33	AH32	AH31
148	Cer.	-	-	Diod	-	BH33	BH32	BH31	-	-	-	-	BH23	BH22	BH21	

FIGURE E-3. The proportional wire chamber word storage assignment for each event.

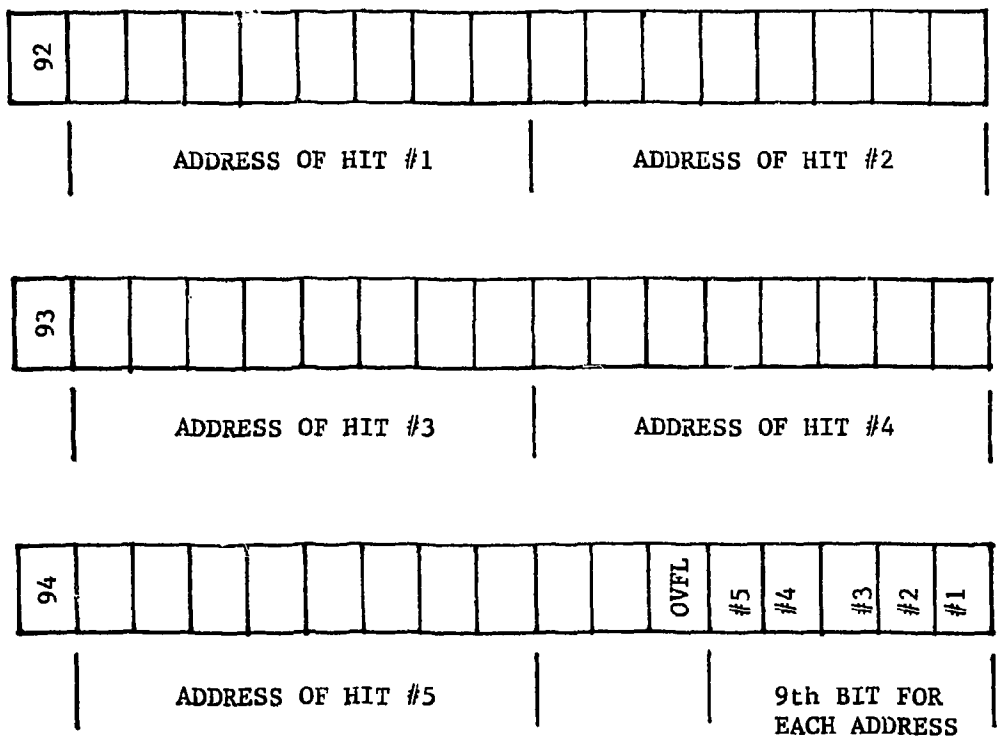

FIGURE E-2. The three-word storage assignment for hits in C1AX.

APPENDIX F

COMPUTER ANALYSIS PROCEDURES

The data tapes written by the HP2114A computer at SLAC were brought to Maryland and unpacked into SUMX[1] format using a program called TRANS. All further data processing was performed on the Univac 1108 computer at Maryland. The unpacking included the stripping off of the diode calibration events. Once this was accomplished for each data tape, the resulting SUMX tape, known as MODØ was processed to a MOD2 stage by adding in the averaged values of the diode calibration amplitudes. The MOD2 level SUMX tapes then formed the input to the one-pass analysis program, which recorded its calculations on another SUMX tape. The names and descriptions of the subroutines used by the analysis program are given in Table F-1 in the order in which they were called. Table F-2 itemizes the event rejection criteria and indicates the subroutines in which they were applied.

TABLE F-1. A list of the subroutines called during the computer analysis.

TAPESR[1]	Called by SUMX; inserted equipment location data and controlled the analysis procedures.
SUB1	Stripped CAMAC status bits from ADC words and summarized AX PWC overflows.
SUB2	Reorganized data for event pictures.
POLARR	Associated polymeter wire addresses with the 12 individual wire planes.
SUB3	Further reorganized data for trajectory analysis and wire mapping.
SUB4	Summed shower counter and hadron filter amplitudes by columns.
SUB5	Performed trajectory analysis, printed out "hot" wire addresses
CLUSTR	Grouped adjacent wires into clusters to be considered as single hits.
COORDI	Converted wire numbers into XYZ coordinates, and searched for hot wires.
LINFIT	Found all 2, 3-point AX lines in C1AX, C2AX, C3X.
LFIT[2]	Fit 3-point lines.
FCHISQ[2]	Calculated chi-square for fits.
LINEAY	Found all 2, 3, 4, 5, 6-point lines in the AY chambers.
LFIT, FCHISQ	
MOMTM	Calculated momentum values for each AX line and each hit in C4X, C5X. Scanned all possible line-point combinations for most consistent matchups, and integrated particle through magnetic field to determine accurate momentum value.
LFIT, FCHISQ	
P4, P5	Calculated momentum for each hit in C4X, C5X respectively.

TABLE F-1 (continued).

XTRAP	Extrapolated a particle of specified momentum, position and direction a short distance through a specified magnetic field.
BFIELD	Specified the magnetic field at a given point in 3-dimensional space.
LINEBX	Reconstructed all 2-point lines in C1BX, C2BX.
LINEBY	Reconstructed BY lines in C2BY and the polymeter.
LFIT, FCHISQ	
POLY	Reconstructed lines in the polymeter and determined multiplicity.
LFIT, FCHISQ	
SUB6	Selected counter columns associated with specific particle trajectories.
SUB7	Checked for wire miscodings.
SUB8	Performed wire maps on PWC's.
SUB9	Calculated dE/dx in spectrometer shower counters.
SUB10	Calculated time of flight for spectrometer particle.
DELTIM	Corrected TOF value for dependence on the position where the particle hit the counter.
SUB11	Performed a coarse identification of events.
SUB12	Printed out a picture of the X and Y views of the events.
PRIN1	Organized and printed out the X view.
PRIN2	Organized and printed out the Y view.
SUB13	Printed out a picture of the polymeter.

TABLE F-2. Events rejected by the analysis program.

#	Calling Subroutine	Description of Reject
1	SUB2	At least 19 AS counters did not digitize.
2	COORDI	The number of AX chambers without hits together with the total number of AX overflows was greater than 3.
3	COORDI	Sum over C1AX, C2AX, C3X: The number of chambers without hits, together with the total number of overflows, was greater than 2.
4	COORDI	At least two of the chambers C1AX, C2AX, C3X had no hits.
5	COORDI	There were no hits in C4X and C5X.
6	LINFIT	There was no AX line projecting into the magnet.
7	LINEAY	The best AY line had phi outside $\pm 10^{\circ}$.
8	LINEAY	The best AY line had KIND less than 40.
9	MOMTM	The best momentum value was less than 350 MeV/c.
10	MOMTM	The best momentum value was greater than 100 GeV/c.
12	MOMTM	The momentum values from C4X, C5X were inconsistent: a) $\lvert\Delta p/p\rvert > .25$ ($\Delta p = \lvert p5x - p4x\rvert$) b) There were no overflows in C4X or C5X. c) This was the best trajectory, not the second best. d) None of C1AX, C2AX, C3X used in the fit had overflows. e) The C4X momentum value was less than 700 MeV/c and the C5X momentum value was less than 550 MeV/c. All of these requirements must have been satisfied in order for the event to have been rejected for inconsistent momenta.
13	MOMTM	The best fit trajectory hit the magnet walls at any point.
17	MOMTM	Same as #9 except that this check followed the calculation of the final momentum value.
14	SUB9	The average dE/dx for the 3 minimum-valued AS planes was less than 0.1.
15	SUB9	S1 was not hit: dE/dx for S1 was less than 0.2.

REFERENCES

APPENDIX F

1. D. E. Trevvett, "SUMX Version M-5", University of Maryland Technical Report 75-038 (1974).

2. P. R. Bevington, "Data Reduction and Error Analysis for the Physical Sciences", McGraw-Hill Book Co. (1969), pp. 104-5, 194.

APPENDIX G

ERROR PROPAGATION FOR HADRON IDENTIFICATION

The probability that a given event is a particle of type a was given in Section IV-G as

$$P(a) = \frac{f_a(t)}{f_a(t) + f_b(t) + f_c(t)} \quad ,$$

where

$$f_a(t) = \frac{N_a}{\sqrt{2\pi}\cdot\sigma} \exp\ \{-\tfrac{1}{2}(\Delta t_a/\sigma)^2\} \quad .$$

The indices (a,b,c) represent some permutation of (π,K,P), and $\Delta t_a = t - t_a$, where t_a is the expected TOF value of the spectrometer particle assuming its identity to be type a.

The variance describing the uncertainty in P(a) is obtained by straightforward differentiation:

$$\begin{aligned}\sigma^2(P(a)) = {} & (\partial P/\partial N_a)^2\sigma^2(N_a) + (\partial P/\partial N_b)^2\sigma^2(N_b) + (\partial P/\partial N_c)^2\sigma^2(N_c) \\ & + (\partial P/\partial t_a)^2\sigma^2(t_a) + (\partial P/\partial t_b)^2\sigma^2(t_b) + (\partial P/\partial t_c)^2\sigma^2(t_c) \\ & + (\partial P/\partial t)^2\sigma^2(t) + (\partial P/\partial \sigma)^2\sigma^2(\sigma) \quad ,\end{aligned}$$

where, for example, $\sigma^2(N_a)$ represents the uncertainty in the N_a value. Taking these terms in reverse order, $\sigma(\sigma)$ is the uncertainty in the width of the TOF distribution and was set equal to 0.1σ. The quantity $\sigma^2(t)$ is simply σ^2. The variances associated with the three calculated TOF values are dependent on the momentum uncertainty. The calculated TOF has the form

$$t_a = \frac{s}{\beta_a c} = \frac{s \cdot (p^2 + m_a^2 c^2)^{\frac{1}{2}}}{pc}$$

where s is the total distance travelled along the trajectory arc. The total momentum uncertainty was taken to be $\sigma(p)/p = .02$.

There are two contributions to the uncertainty $\sigma^2(N_a)$: the statistical counting error and the possibility of particle misidentification. Let the number of events of type a actually present in a sample be designated by M_a:

$$M_a = N_a - dN_a \quad .$$

This number will contain the same statistical error as the observed number N_a. The best estimate of the misidentification error dN_a is zero, but it remains to calculate the uncertainty in this quantity. If a probability $P_i(a)$ is assigned for the identification of the ith event as a particle of type a, based on the parent TOF distributions evaluated for that event, then the actual misidentification error is

$$(dN_a)_i = P_i(a) - \delta_i(a) \quad .$$

The function $\delta_i(a)$ is one if the ith event is actually type a and zero otherwise. That this makes sense is further shown by

$$M_a = N_a - \sum_{i=1}^{N} \{P_i(a) - \delta_i(a)\} = N_a - N_a + \sum_{i=1}^{N} \delta_i(a) = \sum_{i=1}^{N} \delta_i(a) \quad ,$$

which is true by definition. The misidentification error is given by

$$\sigma^2(N_a) = \sigma^2(dN_a) = \sigma^2(P(a)) + \sigma^2(\delta(a)) \quad .$$

P(a) gives the <u>a priori</u> TOF probability distribution according to the laws of physics and is therefore completely determined, if one ignores for the moment the finite statistics upon which the actual calculation

of P(a) is based.

The quantity $\delta_i(a)$ can take on the values 0 and 1. The average probability that it is 1 can be designated by q_i. The uncertainty in the value of $\delta_i(a)$ for a given event is thus

$$\sigma^2(\delta_i(a)) = q_i(1 - q_i)$$

in accordance with the binomial distribution law. Observing that by definition $q_i = P_i(a)$ gives the final result, where the observed value of P(a) is used to approximate the parent TOF distribution. Adding this misidentification error in quadrature to the statistical error gives

$$\sigma^2(N_a) = N_a + \sum_{i=1}^{N} P_i(a)\{1 - P_i(a)\} .$$

A feeling for the second term can be gotten by observing that it is a measure of the degree of overlap of the TOF distributions for the different particle identity classes. Similar expressions apply to the errors in N_b and N_c.

APPENDIX H

CALCULATION PROCEDURE FOR INCLUSIVE HADRON PRODUCTION CROSS SECTIONS

Two different procedures were used for calculating the hadron cross sections. depending on the spectrometer particle momentum. For $0.4 < p < 1.1$ GeV/c, the time-of-flight system was used exclusively for particle identification. Above 1.1 GeV/c the Cerenkov counter was used to flag the pions, resulting in a different calculation procedure.

For the TOF pion identification below 1.1 GeV/c, the corrected number of observed pions was calculated according to

$$N = \frac{(N_o - B)CU/.955}{(S + D)(1 - P)A} \qquad \text{(Pions)}$$

The variables are defined as follows:

N_o = number of observed pions inside origin and TOF cuts.

C = correction for hadrons misidentified as electrons due to the presence of accidental Cerenkov signals.

.955 = correction for fraction of good events outside 2-standard deviation TOF cuts.

B = estimated pion background inside origin cuts.

U = correction for events having unanalyzable TOF.

S = survival probability; the probability a particle traverses the spectrometer without decaying.

D = probability that a pion will decay to a muon, fall within the TOF cuts, and not penetrate the hadron filter.

P = probability that a pion will punch through the hadron filter.

A = probability that the pion will traverse the material composing the spectrometer without being removed through nuclear interactions.

For TOF kaon identification below 1.1 GeV/c, the corrected number of observed kaons was calculated according to

$$N = \frac{N_o CU/.955}{(S + D)(1 - P)A - Q} \qquad \text{(Kaons)}$$

Here the meaning of each symbol is the same as for the pion calculation, but the values used were calculated for kaons. The symbol Q represents the fraction of kaons which decay to two pions and subsequently contaminate the TOF system.

The low momentum protons were corrected according to

$$N = \frac{N_o CU}{.955A} \qquad \text{(Protons)}$$

where the symbols have the same meaning as for pions.

The Cerenkov counter was used to tag pions at momenta greater than 1.1 GeV/c. The corrected number of pions was obtained from the expression

$$N = \frac{N_o C - R}{\{S + (1 - S)(1 - d)\}(1 - P)A} \qquad \text{(Pions)}$$

The previously defined symbols have the same meaning as before. The quantity R represents the number of kaons and protons having an accidental signal in the Cerenkov counter. The quantity d is the probability that a secondary muon produced by decay could penetrate the hadron filter.

The corrected number of high momentum kaons was calculated according to

$$N = \frac{N_o}{S(1 - C)(1 - P)A} \qquad \text{(Kaons)}$$

where C is the probability that the Cerenkov counter fired accidentally. Similarly for the protons,

$$N = \frac{N_o}{(1 - C)A} \qquad \text{(Protons)}$$